„RIBOFLAVIN-TARGETED NANOMEDICINES FOR CANCER IMAGING AND DRUG DELIVERY"

Von der Fakultät für Mathematik, Informatik und Naturwissenschaften der RWTH Aachen
University zur Erlangung des akademischen Grades einer
Doktorin der Naturwissenschaften genehmigte Dissertation

vorgelegt von

Diplom-Chemikerin Yoanna Tsvetkova

aus Plovdiv, Bulgarien

Berichter: Professor Dr. Fabian Kiessling

Professor Dr. Wolfgang Stahl

Tag der mündlichen Prüfung: 20.02.2018

Acknowledgements

I would like to sincerely thank Professor Fabian Kiessling and Professor Wolfgang Stahl for their supervision of my doctoral thesis.

I especially thank Professor Kiessling for giving me the opportunity to work on extremely interesting projects in preclinical cancer research. I am deeply grateful for his great ideas, teaching, motivation, and guidance of my work.

I would like to thank my colleagues at the Institute for Experimental Molecular Imaging for their work, help, and friendship. I was truly lucky for being part of such a young, dynamic and bright team.

I thank my best friends Layla Tulimat, Hari Puspitosari and Gergana Ivanova who became my family in Aachen for the incredible time and their constant support.

I thank my parents Diana and Nikolay Tzvetkovi for their endless love, care, and support. Mostly, I would like to thank my brother Boris Tzvetkov for his great mind, advice and encouragement.

TABLE OF CONTENTS

Chapters:

Chapter 1

1. Introduction

1.1 Molecular Imaging

Molecular imaging is a medical field which deals with the visualization of biological conditions and processes in a living organism. Such conditions and processes include biological events at a cellular or even at a molecular level, such as the location of a specific population of cells, levels of expression of proteins, or cellular interactions. In order to characterize a biological process in a living organism, it is essential to follow the biological events without removing the tissue and the cells of interest, i.e., to monitor the process in its natural environment without disturbing the system under investigation.[1] Therefore, the imaging techniques used in this field are noninvasive and exploit different tissue properties, sometimes combined with imaging agents, as the source of contrast. The imaging techniques can provide spatial resolution sufficient to observe the biological processes in tissue over time without disrupting them. Such longitudinal imaging helps to understand the pathology, progress and underlying mechanisms of numerous diseases and thus offers the potential for early detection and monitoring a treatment.[1]

Molecular imaging has a main application in translational research. By imaging biological processes in diseased tissue, researchers can establish and develop specific markers that can be used in diagnostics, drug development, and therapy. Figure 1.1 shows a schematic overview of a common molecular imaging study. It begins with exploring the pathology of the biological event, for instance the development of cancer. The next step is to identify a target specific to this biological process, such as overexpression of cellular receptors or intracellular proteins. Further, a molecular probe, specific to the target, is identified or synthesized. The molecular probe can be labeled with a contrast agent so that it can be used as a tracer in order to visualize it in in vitro and in vivo studies. The probe has to be tested in vitro in order to assess its cellular interactions, specificity, and toxicity. If the in vitro studies are successful, the probe is further tested in vivo (in small animals, such as rodents) in order to analyze its biological activity. If the molecular probe is efficient in terms of pharmacokinetics and pharmacodynamics, it can be then translated from preclinical studies into clinical trials.

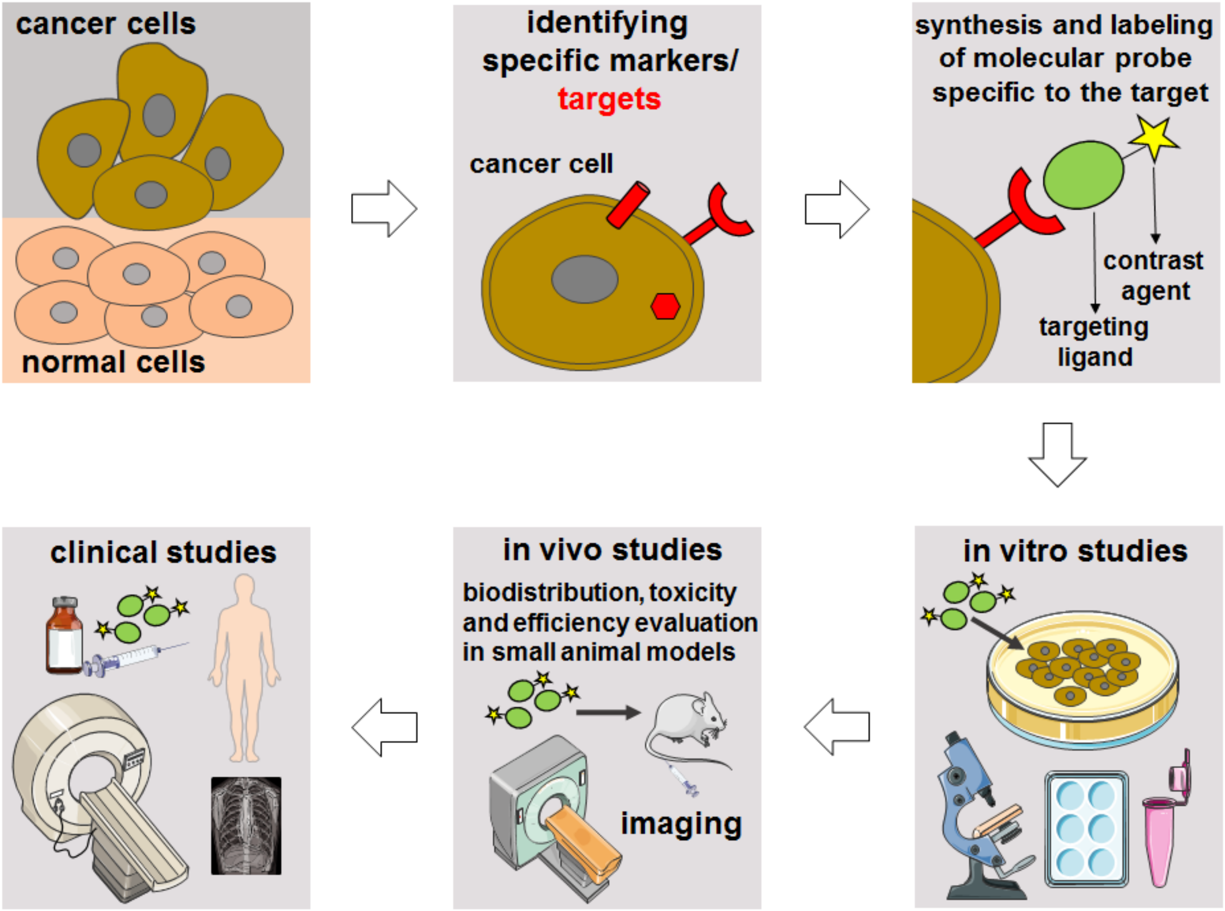

Figure 1.1 Schematic representation of a molecular imaging study in translational research.

The use of small animal models in preclinical research enables the assessment of the biodistribution, pharmacokinetics, and biological response (potential toxicity, side effects, ect.) of potential contrast agents and drugs. The in vivo evaluation of molecular probes in small animals can be performed by different noninvasive imaging modalities, such as optical imaging (OI), computed tomography (CT), magnetic resonance imaging (MRI), positron emission tomography (PET), single photon emission (SPECT), computed tomography (CT), ultrasound (US) or photoacoustic imaging (PAI). Most of these imaging modalities are also used in clinics, as represented in Figure 1.2, which makes the preclinical evaluation to some extent a reliable prediction for the outcome in humans.

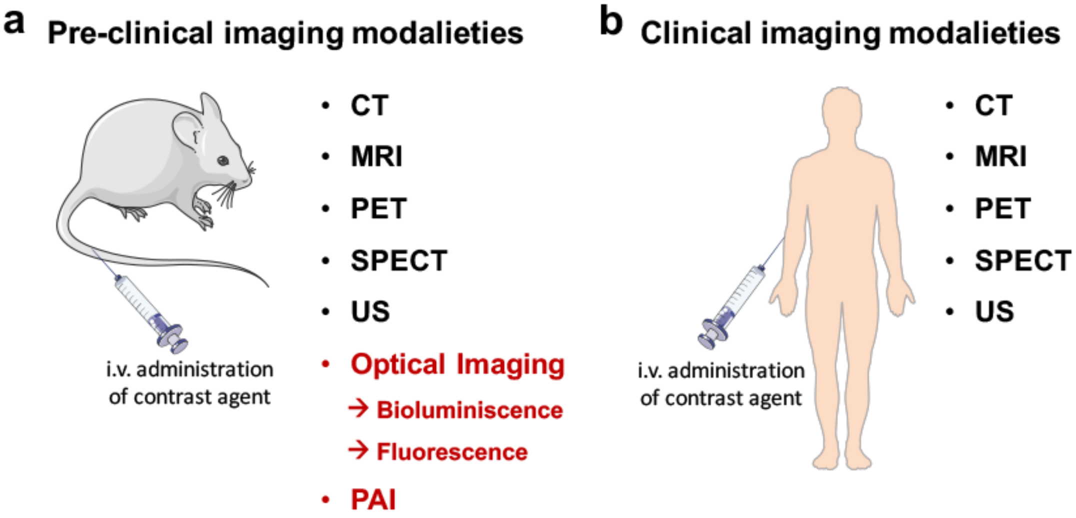

Figure 1.2 Imaging modalities used in a: preclinical settings, b: clinics.[1]

Optical and photoacoustic imaging are more often used in preclinical settings, mainly due to limitations in penetration depth. These modalities are applicable in humans only for superficial tissue examinations. There are, however, limitations for each imaging modality in terms of sensitivity or special resolution. For this reason, different modalities can be combined (PET/CT, PET/MRI, CT/FMT) and thus give more detailed information for the region of interest.

1.2 Imaging modalities and contrast agents

Imaging modalities can be classified into two groups: those that provide anatomical and morphological information and those that provide molecular and functional information.[1,2] Computed tomography, magnetic resonance imaging and ultrasound are imaging technologies with high spatial resolution and provide anatomical and morphological information.

Optical and photoacoustic imaging, positron emission tomography and single photon emission computed tomography are used only with probes, such as radiotracers or fluorophores, and have high sensitivity (referring to the amount of contrast agent that can be detected) to provide molecular and functional information.

The choice of the imaging modality depends mainly on the biological process that needs to be visualized and evaluated. There are different factors, for example: spatial resolution, sensitivity, region of interest, penetration depth, quantitative data, number of scans, etc., that need to be considered in order to select the most appropriate imaging method.

A description of the imaging modalities is summarized in Table1, the data is obtained from James and Gambhir (*Phisiol. Rev.* 2012) [1] and Kunjachan et al. (*Chem. Rev.* 2015) [2].

Table 1.1 Imaging modalieties and their properties.[1,2]

Imaging Modality	*Radiation*	*Resolution*	*Main Advantages*	*Main Disadvantages*	*Contrast agents*
PET	high energy gamma rays	1 – 2 mm	high sensitivity (pM range), limitless penetration depth, quantitative imaging data	low spatial resolution, ionizing radiation, no anatomical information, high cost	modified with radioisotopes: ^{11}C, ^{13}N, ^{15}O, ^{18}F, ^{44}Sc, ^{62}Cu, ^{64}Cu, ^{68}Ga, ^{82}Rb, ^{86}Y, ^{89}Zr, ^{124}I
SPECT	lower energy gamma rays	1 – 2 mm	high sensitivity (pM range), limitless penetration depth, quantitative imaging data	low spatial resolution, ionizing radiation, no anatomical information, high cost	modified with radioisotopes: ^{99m}Tc, ^{111}In, ^{123}I, ^{201}Tl
CT	X-rays	50-200 µm	high spatial resolution, anatomical information, very good hard tissue contrast, limitless penetration depth, low cost	limited soft-tissue contrast, low sensitivity (mM range), ionizing radiation	iodine- or barium-based
Optical Bioluminescence Imaging	VIS light	3 – 5 mm	highest sensitivity (fM range), no ionizing radiation, low cost	low spatial resolution, only 2D imaging, low penetration depth (~2cm), no anatomical information	substrates for enzymatic reaction
Optical Fluorescence Imaging	VIS or NIR light	<10 mm	high sensitivity (nM), no ionizing radiation, low cost	low spatial resolution, low penetration depth (~10 cm), autofluorescence, no anatomical information	fluorophores
MRI	radio waves	25 – 100 µm	high spatial resolution, very good soft tissue contrast, functional and anatomical information, no ionizing radiation, limitless penetration depth	low sensitivity (mM range), long acquisition time, high cost	Gd-based; iron oxide nanoparticle
US	high-frequency sound	0.05 – 2 mm	real-time imaging, high spatial resolution, high sensitivity, portable, no ionizing radiation, low cost	no whole-body imaging, user-dependent	microbubbles
PAI	NIR light, acoustic waves	0.01 – 1 mm	real-time imaging high sensitivity (nM range), no ionizing radiation	low penetration depth (~5cm)	fluorescent dyes, gold nanoparticles

Computed tomography, magnetic resonance imaging and fluorescence molecular imaging are further explained in more detail since these modalities were extensively used in the course of the thesis.

Computed tomography

CT is an imaging modality employed in preclinical and clinical settings. It exploits the different attenuation of X-rays in tissue to produce series of 2D acquisitions, which are combined to deliver a 3D anatomical image. A schematic representation of X-rays generation and image acquisition is shown in Figure 1.3.

X-rays are electromagnetic radiation in the wavelength-range between 0.01 nm and 10 nm. The radiation is generated in a vacuum tube by the interaction of free accelerated electrons, emitted from a cathode upon high voltage, with the electrons of the element used as anode (most commonly tungsten). When the free high-speed electrons hit the anode, energy, produced by two different processes, is released in the form of X-rays. In the first process, the accelerated electrons are deflected and slowed down by the tungsten nuclei (Coulomb interactions) which results in energy release called Bremsstrahlung (braking radiation). In the second process, some of the free high-speed electrons collide with the orbital electrons of tungsten and dislodge them from the atoms. When an electron is removed from the orbital, the vacancy it leaves is filled by another electron dropping from a higher energy state. This results in the emission of radiation characteristic to the element used for anode. The X-rays produced by Bremsstrahlung have higher energy than the characteristic radiation emitted in the second process. Due to their high energy, they have limitless penetration through tissue and are used for medical imaging.[3]

A CT scan is performed by rotating an X-ray source at 360 degrees around a subject. The X-rays passing through the subject are acquired at different angles by detectors placed opposite the X-ray source. The X-rays are attenuated to a different extent in the body, depending on the tissue density, which provides the contrast of the image. Therefore, series of attenuation profiles are obtained and are mathematically reconstructed to obtain a 3D image of the scanned object. Highly dense tissues, such as bones, strongly absorb X-rays and appear white on the CT image, while media that absorbs poorly, such as air in the lungs, appear black. Soft-tissues appear in grey and have moderate contrast. For this reason, iodine-based contrast agents are commonly used to provide a better special resolution for soft tissue imaging.[3]

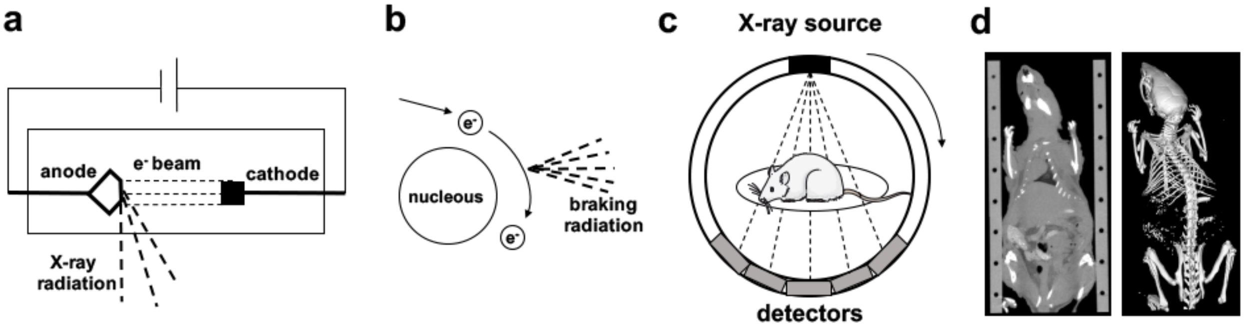

Figure 1.3 Schematic representation of CT imaging. a: X-rays generation, b: Generation of braking radiation, c: CT scanner, d: Example of a mouse CT image.

Magnetic resonance imaging

MRI is an imaging modality employed in preclinical and clinical settings. By using this technique, objects containing NMR-active nuclei, such as ^{1}H, ^{13}C, ^{31}P, can be visualized with the application of magnetic field and radio frequency waves. Since hydrogen is the most abundant element in tissues, its nuclear spin properties are exploited to obtain high-resolution three-dimensional whole-body image. When a subject is placed in a strong magnetic field B_0 (up to 3 T in clinical MRI scanner), the nuclei spins of the hydrogen atoms align either with the direction of the magnetic field (lower energy state) or opposite to B_0

(higher energy state). Small excess of the spins is in the low-energy state, and this population difference results in a net magnetization vector (sum of the magnetization vectors of the spins) aligned with B_0, as illustrated in Figure 1.4a. In addition, all protons experience a torque by the strong magnetic field, which causes spin precession at a specific angular frequency (Larmour frequency) proportional to the strength of B_0. By applying a radio-frequency pulse with the Larmour frequency, perpendicular to B_0, the magnetization vector can be tilted away from the direction of B_0. When the the radio frequency source is switched off, the spins return back in orientation with B_0, resulting in two relaxation processes called longitudinal relaxation (spin-lattice relaxation, with time constant T1) and transverse relaxation (spin-spin relaxation, with time constant T2), shown in Figure 1.4b. During T2-relaxation, the protons emit the absorbed energy, which can be measured by a receiver coil and the signal is referred as free-induction decay (FID), depicted in Figure 1.4c. Since the protons have different chemical environment, they also display different T1 and T2 relaxation times, which can be used to obtain contrast between tissues.[4]

During the acquisition of MR images, the RF pulse is repeatedly applied at a determined rate and the time between two excitation pulses is referred as time of repetition, (TR). The time at which the FID signal is measured is called time of echo (TE). Thus, by adjusting TR and TE, one can change the contrast of different tissues in the MR image. By applying slice selection gradient (SSG), phase encoding gradient (PEG), and frequency encoding gradient (FEG) the obtained signals can be reconstructed in 3D grey-scale images.[4]

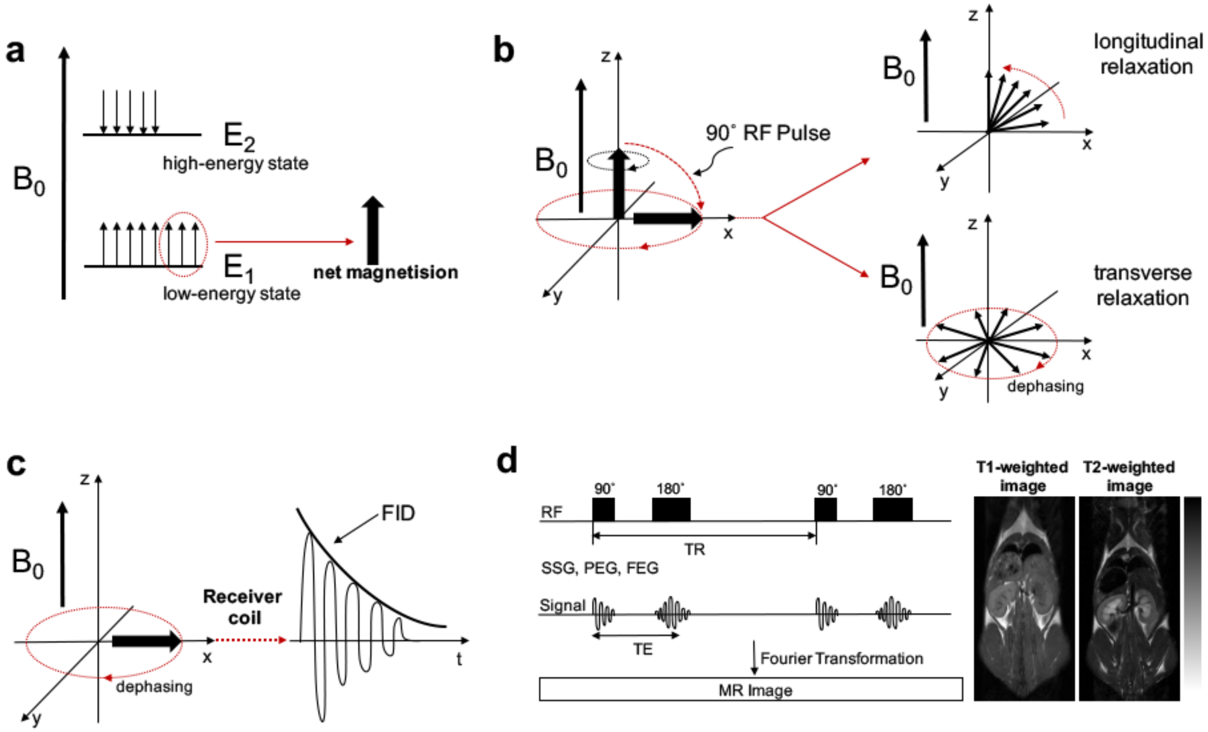

Figure 1.4 Schematic overview of MR imaging process. a: Spins' alignment in the presence of strong magnetic field B_0, and net magnetization vector resulting from the different spin population of the energy-levels, b: Tilting the net magnetization 90º from B_0 (depicted on the z-axis) by applying RF-pulse with the Larmour frequency and illustration of T1-longitudinal relaxation (spins rotating back to equilibrium) and T2-transverse relaxation (spin precession out of phase), c: FID signal from decreasing magnetization on the xy-plane resulting from spin precession out of phase, d: Schematic representation of signal acquisition (left) and example of T1-weighted and T2-weighted coronal MR images of a mouse.

Fluorescence molecular tomography

FMT is a preclinical three-dimensional fluorescence imaging modality which allows localization and quantification of fluorophores in tissue. The fluorophores, used for in vivo experiments, usually have an excitation wavelength in the visible or near infra-red range (650-800 nm), since the absorption of tissue, especially of hemoglobin, below 650 nm is high (Figure 1.5a). Furthermore, the penetration depth of the light in the tissue is low (<10 cm), which makes a whole body scan possible only for small laboratory animals, such as mice. Since melanin also absorbs light in the VIS and NIR range, nude mice, that have no dark skin pigments, are preferably used for FMT. This imaging method can provide not only a superficial two-dimensional (2D) fluorescence reflectance image but also an in-depth three-dimensional fluorescence assessment (Figure 1.5c). For three-dimensional (3D) fluorescence analysis the animal is illuminated with a laser (at up to 120 different points) in order to excite the fluorophore within the tissue, and the emitted light is collected by a detector (CCD camera). The data is then reconstructed by a software [5] to provide a 3D image of the fluorescence intensity and distribution within the mouse. Fluorescence tomography, however, does not provide an anatomical image of the animal and the signal cannot be properly assigned to different tissues. For this reason, FMT is combined with CT, that can generate a 3D anatomical image. For this reason, the mouse is immobilized in a cassette and scanned with both imaging modalities after which an overlay 3D CT-FMT image can be generated (Figure 1.5d) and the fluorescence signal can be assigned to the different organs. Furthermore, the signal intensity is normalized to the absorption properties of different tissues so the amount of fluorophore in them can be quantified. Due to its high sensitivity FMT is a very useful preclinical method for evaluating the pharmacokinetics and biodistribution of fluorescently labeled probes in small animals.

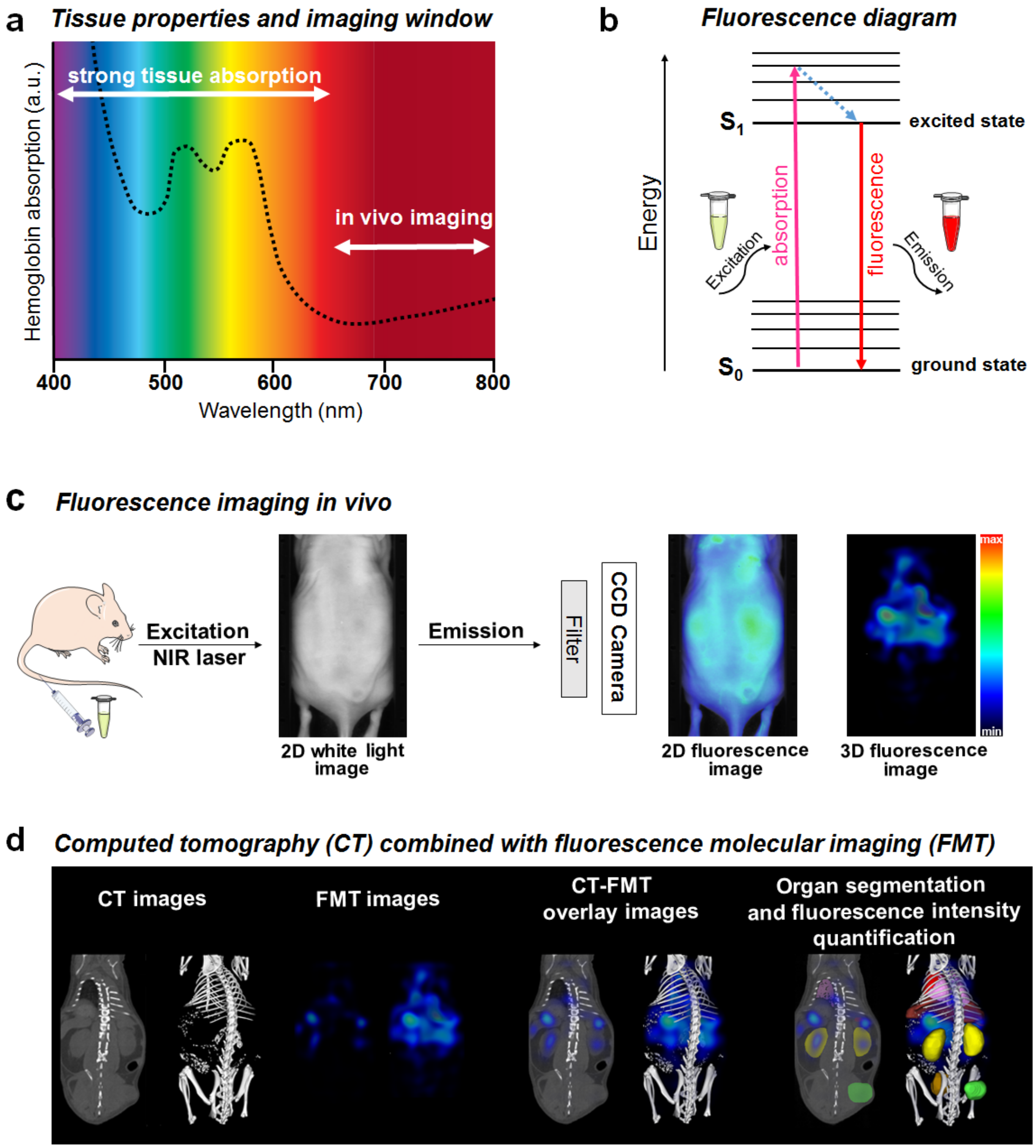

Figure 1.5 Overview of fluorescence molecular imaging. a: Absorption spectrum of hemoglobin in VIS and near infrared spectrum, b: Diagram of excitation and emission of fluorophores, c: Representation of fluorescence imaging in vivo, example of 2D and 3D fluorescent images of a nude mouse injected with a fluorophore (excitation λ=680 nm and emission λ=707 nm), d: Representation of combined CT-FMT images of a mouse.

1.3 Cancer imaging and drug development

Various imaging techniques are used for cancer diagnosis, monitoring and treatment. The development and combination of different imaging modalities can provide quantitative spatial and temporal information about tumor growth, morphology, structure and metabolism. Tumor size and structure are usually assessed by CT and MRI. Contrast-enhanced ultrasound, CT or dynamic MR imaging can be used to evaluate the blood flow and volume, or vascularity in the tumor.[6] PET is commonly applied to assess tumor metabolism.[7] Monitoring different tumor properties is particularly helpful in cancer treatment and in the development of new chemotherapeutic drugs.

The treatment of solid tumors usually involves surgical removal (if possible) combined with chemotherapy and often with radiation therapy. Chemotherapeutics are substances toxic for cells, with various mechanisms to inhibit the cellular function, growth and division. The different types of drugs, based on their mechanism of action, are schematically represented in Figure 1.6. Chemotherapeutic agents are generally classified into antimetabolites, antimitotics and drugs affecting nucleic acid function and tyrosine kinase function. Antimetabolites are molecules with chemical structures similar to the nucleobases and thus can inhibit the activity of enzymes involved in the DNA and RNA synthesis, or can even be incorporated in the DNA or RNA, which result in termination of the nucleic acids synthesis and cell death.[8] Antimitotics interfere with microtubules and block cell mitosis, which interrupts the cell division and has cytotoxic effects.[9] Drugs which directly affect nucleic acid function can act in various ways: intercalate in the DNA, cross-link with the DNA strands, alkylate DNA or cause DNA fragmentation, and thus have toxic effects on the cells. Drugs, which inhibit tyrosine kinase function, hinder the proliferation and invasion of malignant cells. Other types of anticancer drugs inhibit the function of essential cellular enzymes (such as topoisomerase and proteasome) and prevent DNA replication.

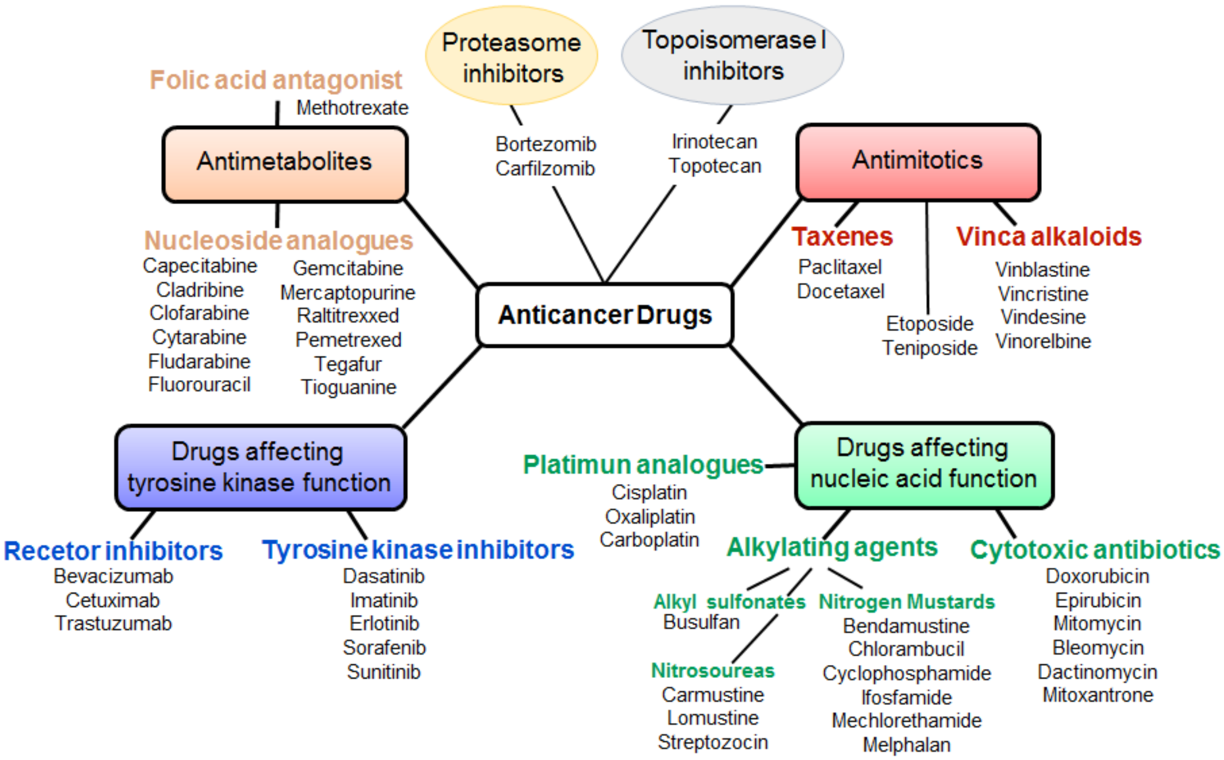

Figure 1.6 Scheme presenting different types of anticancer drugs.

Chemotherapeutics are small molecules (low molecular weight) with short circulation time and large volume of distribution. These properties often lead to: I) low accumulation in the tumor (only ca. 0.2 % of the administered chemotherapeutics reaches the tumor) and II) non-specific tissue accumulation causing massive side effects such as hair loss, stomach irritation, healthy organ damage and low counts of blood cells. Toxic side effects to healthy tissue are one of the main limiting factors for a continuous and high dose administration of anticancer drugs. In addition, many of the chemotherapeutics are poorly or not at all water-soluble which hinders the efficiency of the drug delivery. Furthermore, repeated administration of chemotherapeutics often causes cancer cells to develop multidrug resistance (MDR), which makes the treatment less efficient.

Despite severe side effects and low tumor accumulation, these drugs are still the routine for cancer treatment in clinics. There are, however, strategies for their administration which aim to improve cancer treatment by reducing drug accumulation in healthy tissue and increasing the drug amount in the cancer lesion. These approaches are based on the incorporation of the drugs in nanomaterials, which serve as drug delivery systems, called nanomedicines.[10,11,12]

Nanomaterials, which are used as drug vehicles, most commonly polymers, micelles, liposomes, nanoparticles and antibodies, are within the size range of approximately 5-200 nm, schematically presented in Figure 1.7.[13] The chemotherapeutic drugs can be bound either physically (adsorption, encapsulation) or chemically to the nanomaterials.

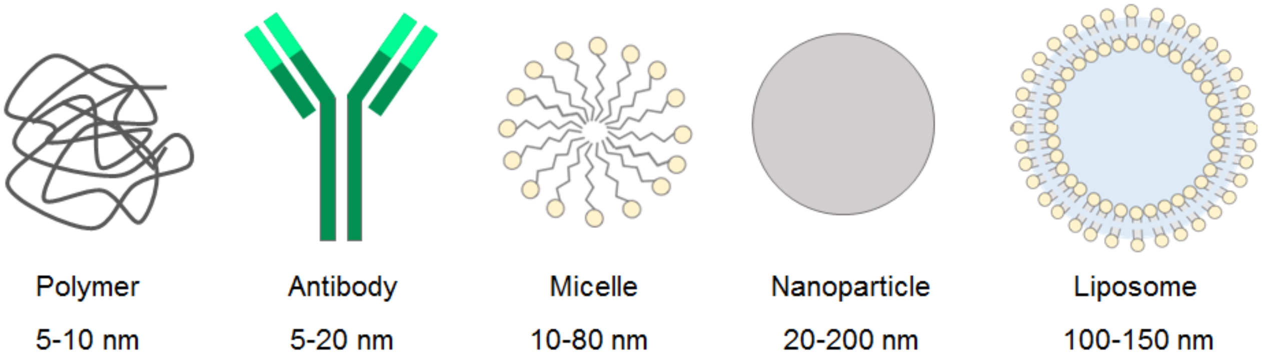

Figure 1.7 Schematic representation of nano drug delivery systems.[13]

The application of nanomedicines has numerous advantages compared with the administration of free drugs: nanomedicines have high drug loading capacity, enhance the drugs water solubility and increase the blood half-life of the drugs. Furthermore, due to their large size, nano drug delivery systems also have low penetration and extravasation in normal tissue, which prevents their accumulation in most of the healthy organs. The mechanism through which the nanomedicines accumulate and extravasate at the tumor site, generally referred as passive targeting, is based on the enhanced permeability and retention (EPR) effect. EPR results from the tumor’s abnormal, leaky vessels and impaired lymphatic drainage.[14] Gaps in the vessel endothelium allow the penetration of the drug carriers in the cancer interstitium, while the low lymphatic drainage in the tumor tissue contributes to their retention and accumulation.[15–19] As the nanomedicines get entrapped in the tumor, they may enter the cells (in very low amounts) through unspecific endocytosis, or release the chemotherapeutic payload in the interstitial space where the drugs can diffuse and reach the tumor cells. A comparison between the properties, pharmacokinetics, and biodistribution of free chemotherapeutic drugs and nanomedicines is represented in Figure 1.8.

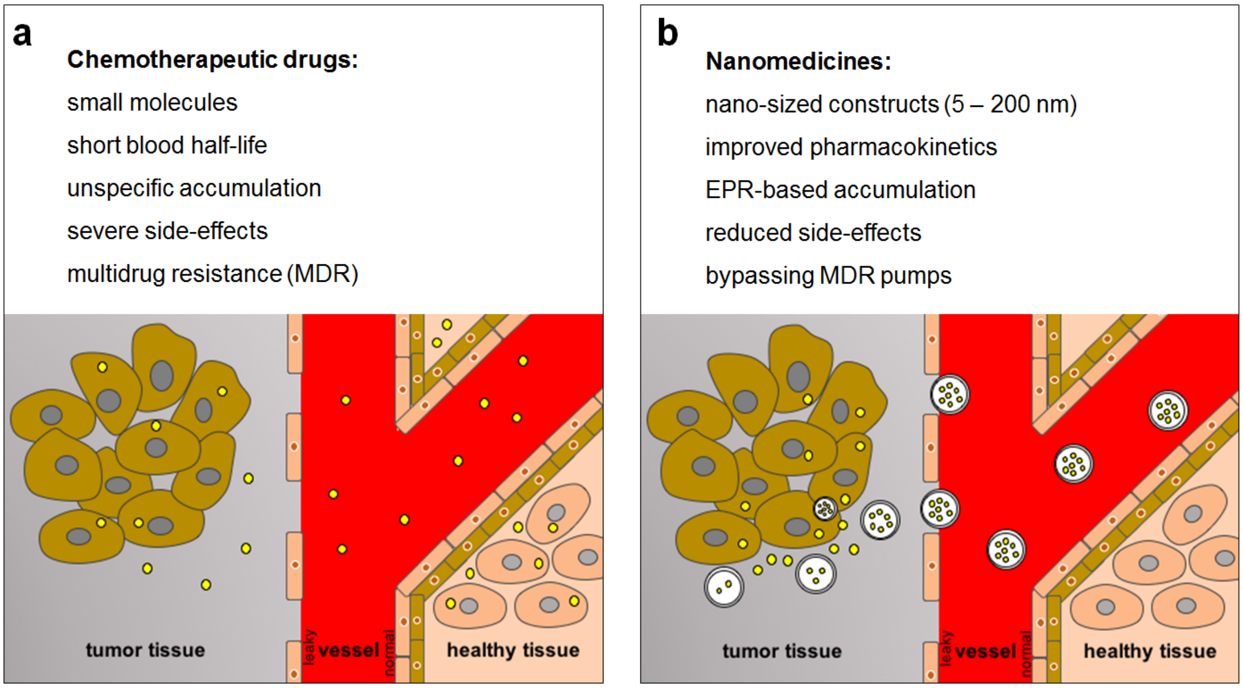

Figure 1.8 Comparison between the properties of chemotherapeutic drugs and nanomedicines and schematic presentation of their biodistribution in cancer and healthy tissue. a: chemotherapeutic drugs, b: nanomedicines.[13]

In order to enhance the nanomedicine accumulation at the tumor site, the drug carriers can be conjugated to targeting ligands, which specifically bind to certain proteins (receptors) overexpressed on the membrane of malignant cells or angiogenic vessels, schematically represented in Figure 1.9. This approach is usually referred as targeted drug delivery or active targeting, and is suggested to increase the retention and cellular uptake of the nanomedicines.[12] The internalization of the nanomedicines is useful for drugs which need to be delivered intracellularly or for drugs which are otherwise poorly taken up by cells. In addition, active drug delivery to angiogenic endothelial cells would lead to disruption of the vessels and in this way to tumor growth inhibitoin.[13]

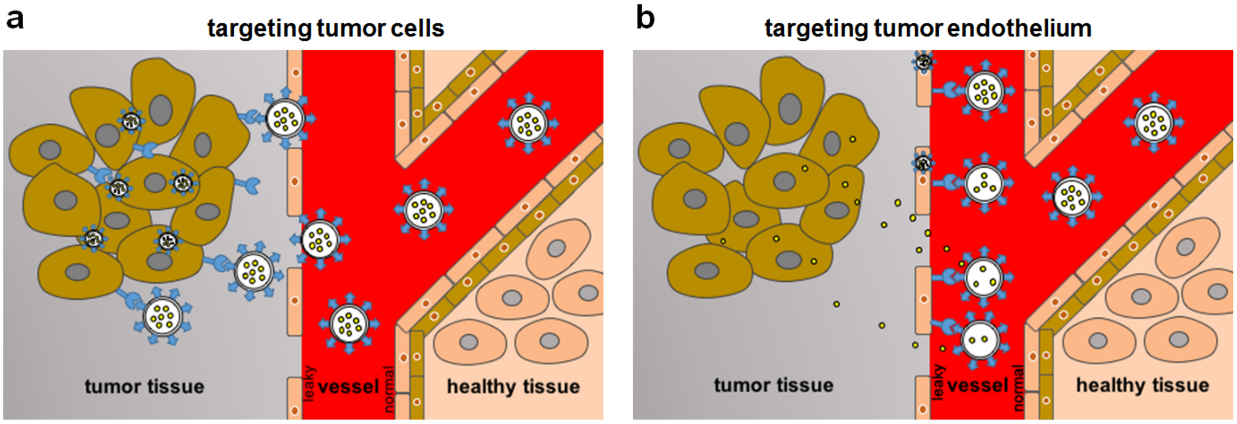

Figure 1.9 Schematic presentation of biodistribution of tumor-targeted nanomedicines for a: tumor cells, b: tumor vessel endothelial cells.[13]

On the other hand, targeted nanomaterials may not only serve as drug delivery systems but also as contrast agents for cancer diagnostics.

Nevertheless, the efficiency of passive and active cancer targeting with nanomedicines highly depends on the degree of EPR effect that may vary not only among different tumor types but also in different regions within a single tumor. Fast-growing and well vascularized tumors usually tend to display higher vessel leakiness than slow-growing poorly vascularized tumors and thus may respond better to nanomedicine treatment.[6,9] An example for this was reported for doxorubicin loaded liposomes (Doxyl) that showed higher efficiency than free chemotherapeutic drugs only in highly leaky tumors, such as Kaposi sarcoma and head and neck cancer.[20–22] In less leaky tumors, however, Doxyl did not perform better than the free drugs, as reported for breast cancer.[23] Furthermore, the pathophysiological tumor characteristics are not the only factor which determines the efficiency of nanomedicines. The design of the nanoconstruct also plays an important role for its performance. Properties like size, structure, and charge of the vehicle influence its blood half-life, recognition by the immune system, and extravasation in the tissue.[24,25] In case of active targeting, the properties and the expression of the receptor have a great impact on the nanomedicine internalization and its homogeneous distribution in the tumor tissue. There are numerous targets overexpressed in cancer lesions or angiogenic endothelial cells, such as folate receptor [26–30], transferrin receptors [28,31–36], integrins [37–41], vascular endothelial growth factor (VEGF) receptor [42,43] and glucose transporters [44–51]. These proteins are markers for the cancer up-regulated metabolism and promote its cell growth, proliferation and invasion. Riboflavin (vitamin B2), similarly to folic acid (vitamin B9), plays an important role in cellular metabolism and has recently drawn attention as a potential targeting ligand for cancer diagnosis and drug delivery.

1.4 Riboflavin-based targeting

1.4.1 Riboflavin cellular uptake and metabolism

Riboflavin (RF) is a water soluble vitamin (B2), which is obtained from the diet. RF is a small biomolecule that is essential to cellular metabolism, proliferation, and development. Within the cell, riboflavin is modified by enzymes to its biologically active forms: flavin mononucleotide (FMN) and flavin adenine dinucleotide (FAD), shown in Figure 1.10. Riboflavin is first modified to FMN by riboflavin kinase, a cytosolic enzyme that phosphorylates the terminal alcohol group of the RF ribityl chain. FMN can be further converted to FAD by the enzyme FAD Synthase, which attaches an adenosine monophosphate to the FMN phosphate group. FMN and FAD are important cofactors for numerous enzymes (oxidases and reductases) that play an important role in the metabolism of carbohydrates, proteins, and lipids.[52]

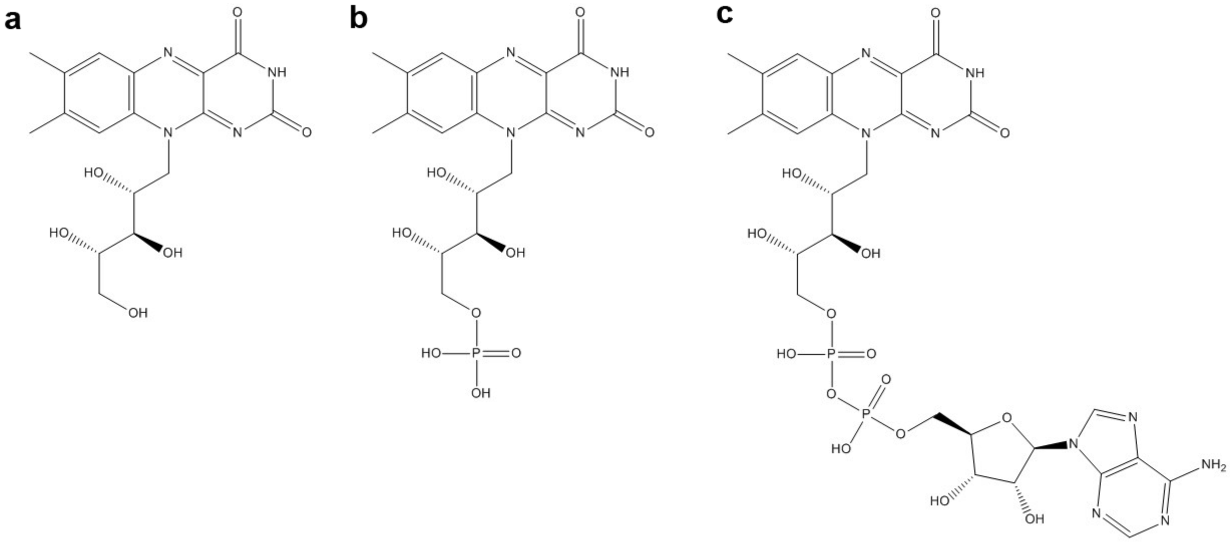

Figure 1.10 Chemical structure of a: riboflavin, b: FMN and c: FAD.

The riboflavin metabolism in the cell has been thoroughly investigated, but its transport within the cell still remains partially elusive. At first, it was considered that riboflavin enters the cells only through passive diffusion, since RF is lipophilic enough to pass through the cellular membrane. However, this takes place only for a small amount of RF. Recently, it has been shown that the riboflavin cellular uptake is carrier-mediated and strictly regulated by three transmembrane transporters [53–55]:

- Riboflavin transporter 1 (RFT1, encoded by the gene SLC52A1), mainly expressed in the small intestine and placenta.[53]
- Riboflavin transporter 2 (RFT2, encoded by the gene SLC52A2), mainly expressed in the small intestine, colon, kidneys, prostate and testis.[54]
- Riboflavin transporter 3 (RFT3, encoded by the gene SLC52A3), mainly expressed in the brain, spinal cord, salivary gland, and testis.[55]

The exact mechanism of RF internalization through the riboflavin transporters is still not fully characterized. Since RF is obtained from the diet and thus enters the blood circulation via intestinal absorption, initial studies on RF transport focused on the RFT expression and functionality in the intestinal epithelial cells. Subramanian et al.[56] performed confocal live imaging of Caco-2 cells (polarized intestinal cells) transfected with GFP-RFT1, GFP-RFT2 and GFP-RFT3, showing that the three transporters are expressed on the cell surface as well as intracellularly. GFP-RFT2 was found to be predominantly expressed at the apical domain, while GFP-RFT1 and GFP-RFT3 at the basolateral domain as well as in intracellular vesicle. Furthermore, it was shown that there is a difference in expression and functionality among the transporters in the intestinal cells: RFT2 was found to be more abundantly expressed and displayed a higher rate of RF uptake than RFT1 and RFT3. These data indicate that the RF transport through the lumen is vectorial: RFT2 most probably facilitates the RF entry into the absorptive epithelia while the other two transporters may regulate its exit from the lumen into blood circulation (schematically represented in Figure 1.11).[56]

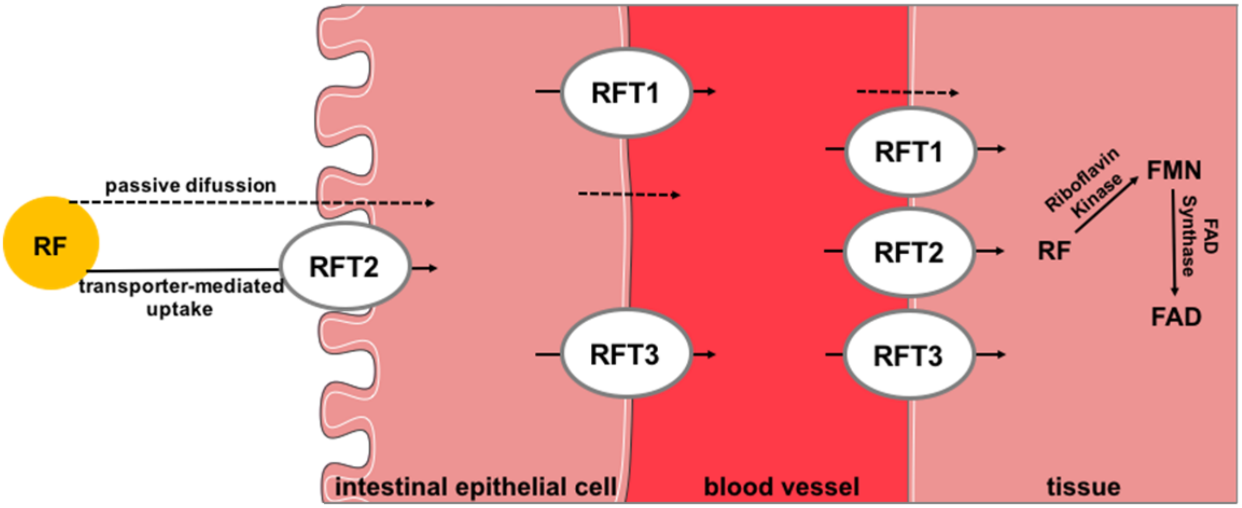

Figure 1.11 Schematic presentation of RF transport from the intestinal epithelium to the tissue.

Once RF reaches the blood circulation, it gets non-specifically adsorbed on different plasma proteins such as albumin and immunoglobulins, which may play a potential role in RF conservation, transport, and delivery to various organs.[57] There is, however, a plasma protein, Riboflavin Carrier Protein (RCP), which selectively binds to riboflavin. RCP is an estrogen-regulated protein released by the liver and oviduct into the bloodstream. RCP has a pregnancy-specific role, as its main function is to deliver RF to the embryo. This riboflavin-binding protein has been identified in human umbilical cord serum, as well as in the plasma of laying hens, cows, mice, rats, spadefoot toads, turtles, and bonnet monkeys.[58–60] The first well characterized RCP has been isolated from chicken (cRCP). Its crystal structure and RF-binding site have been thoroughly investigated, showing that that RF binds within a folded pocket of the protein in 1:1 stoichiometric ratio, with strong hydrophobic interactions of the RF isoalloxazine ring with RCP- tyrosine and tryptophan (Tyr75 and Trp 156) amino-acids, as shown in Figure 1.12.[58]

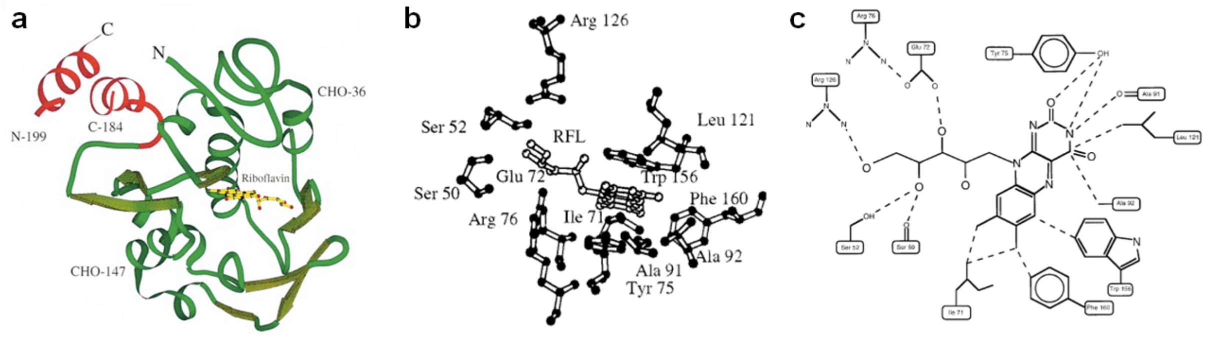

Figure 1.12 Structure of cRCP. a: RCP ribbon diagram of cRCP in which the Rf-binding domain is represented in green, the protein's phosphorylated part in red, and RF in yellow, b: Steric representation of the RCP amino-acids at the RF-binding site, c: Schematic representation of the amino acids which interact with RF.[58] The image is adapted from Ref. 58.

Chicken-RCP is shown to have a close homology with the riboflavin carrier proteins from other species. Monoclonal antibodies against cRCP were shown to cross-react with simian, rodent, and human RCP.[61] This cross-reactivity has been used to analyze the function of RCP in human cells. Mason et al.[61] performed immunofluorescence studies with cRCP and anti-cRCP, and Liquid Scintillation Counting experiments with [^{3}H]RF and ^{125}I-cRCP on human placental trophoblasts (BeWo) and suggested that RCP may be secreted by the cells into the extracellular environment to facilitate RF cellular uptake. The RCP-RF complex is shown to interact with a specific membrane receptor and is internalized by the cells via clathrin-mediated endocytosis.[61] However, it is not yet known which receptor is involved in RCP uptake.

In conclusion, RF cellular uptake is shown to be complex and to involve different pathways: passive diffusion through the cellular membrane and interaction with transmembrane transporters (RFT1, 2 and 3) and a plasma protein (RCP). Although none of the transporter-mediated pathways is fully characterized, they are shown to play an important role in RF cellular uptake. Since riboflavin is essential to the cellular survival and proliferation, upregulation in its transport has been associated with metabolically active cells, such as cancerous cells.

1.4.2 Clinical significance of riboflavin in cancer

The first clinical studies which related riboflavin metabolism to cancer disease reported significantly elevated RCP plasma levels for patients with breast adenocarcinoma compared with healthy women. Karande et al.[62] showed that the concentration of the riboflavin binding protein in the serum of cycling breast cancer patients was four times higher than in their healthy counterparts (14.7 ± 5.3 ng/ml, n = 41 vs 3.8 ± 0.7 ng/ml, n= 14). The difference in RCP concentrations were even more pronounced for post-menopausal patients, for which RCP was found to be ten times higher compared with healthy age-matched women (17.0 ± 4.6 ng/ml n = 49 vs 1.7 ± 0.7 ng/ml, n = 9). Furthermore, increase in RCP levels could be clearly associated with the disease progression, rising from 8.4 ng/ml for early stage to 20.0 ng/ml for advanced disease stage with metastasis. Immunohistochemical analysis of the excised cancer lesions revealed that RCP is localized in the cytoplasm of the tumor cells, leading to the hypothesis that the protein production is upregulated in neoplastic cells and subsequently released from them in the bloodstream.[62] Rao et al. demonstrated similar results in a separate clinical study on breast cancer and showed that the levels of RCP in plasma may serve as an indicator for malignancy, with positive predictive values of 88% for breast tumors in stage I and II, and 100% for tumors in stage III-IV.[63]

In addition to cases of breast cancer, RCP was associated with hepatocellular carcinoma and prostate adenoacarcinoma as well. Elevated RCP plasma levels were also measured for patients with hepatocellular carcinoma (21.75 ± 14.66 ng/ml) compared to healthy controls (0.73 ± 0.25 ng/ml).[64] In addition, RCP was also shown to be overexpressed in prostate adenocarcinomas.[65]

Aili et al.[66] performed another clinical study and presented analysis of biopsy tissue of cervical squamous cell carcinoma, that showed higher RFT-2 levels in the cancer lesions (mRNA level: 0.21 ± 0.14 and protein level: 0.93 ± 0.41, n = 22) compared with normal cervical epithelium, 5 cm distant from tumors, (mRNA level: 0.16 ± 0.12 and protein level: 0.80 ± 0.36, n = 22). Moreover, the expression of RFT-2 in the tumor cells was correlated to the progress of the disease, with further increase in the RFT-2 levels in advanced tumor stages.[66]

These clinical data clearly indicate that the RF uptake and transport may be up-regulated in malignant tissues due to overexpression of RCP and the RF-membrane transporters. Consequently, these proteins could be used as efficient targets for cancer diagnostics and drug delivery systems.

1.4.3 Riboflavin-targeted nano drug delivery systems

The role of riboflavin was investigated in numerous preclinical studies on cancer, which showed that RF serves as an efficient targeting ligand of various nano drug delivery systems (polymers, dendrimers, liposomes, nanoparticles). Here are some important literature-reported studies which demonstrated that RF facilitates an enhanced and receptor-mediated uptake of nanoconstructs in different cancer cell lines in vitro and has a great potential as a targeting agent for malignant lesions in vivo.

N-(2-hydroxypropyl)methacrylamide (HPMA) polymers

Bareford et al.[67] evaluated riboflavin-functionalized HPMA polymers as a drug delivery system for the breast cancer cell line MCF-7. The presented in vitro studies showed that RF-targeted polymers were internalized by cancer cells to a higher extent than non-targeted polymers. Moreover, RF showed higher efficiency in cellular uptake as a targeting ligand than folic acid (FA), which is a well-characterized targeting ligand for breast cancer (RF-HPMA vs. FA-HPMA: 50.86 ± 2.69 vs 27.62 ± 3.42 ng/mg protein/ 60 min). Furthermore, RF-HPMA was conjugated to the chemotherapeutic agent Mitomycin C and showed 7-fold higher drug accumulation in cells in comparison to the free drug.[67] These data indicate that RF could be used as a ligand for targeted drug delivery systems.

Liposomes

In another study focused on targeted drug delivery systems, Beztsinna et al.[68] studied the efficiency of riboflavin-modified liposomes in vivo, in CD1 nude mice bearing squamous cell carcinoma (A431) and prostate cancer (PC3) xenografts.

The targeting specificity of the liposomes in vivo was first evaluated in CD1 nude mice bearing PC3 tumors (Figure 1.13). A hydrophobic near-infrared lipophilic dye DiR (1,1′-dioctadecyl-3,3,3′,3′-tetramethylindotricarbo-cyanine iodide) was inserted in the phospholipid bilayer in pegylated RF-targeted and control liposomes in order to assess their biodistribution and tumor accumulation means combined CT-FMT. Histological analysis of excised tumor cryosections displayed significantly higher fluorescence signal (corresponding to the amount of liposomes accumulated in the tissue) in the mice which received targeted nanocarriers (78.2 ± 29.4 au/area) compared to the nontargeted (40.8 ± 7.6 au/area). The fluorescent signal of the RF-liposomes was colocalized with the endothelial cells of angiogenic vessels which indicated specific tumor vascular targeting.[68]

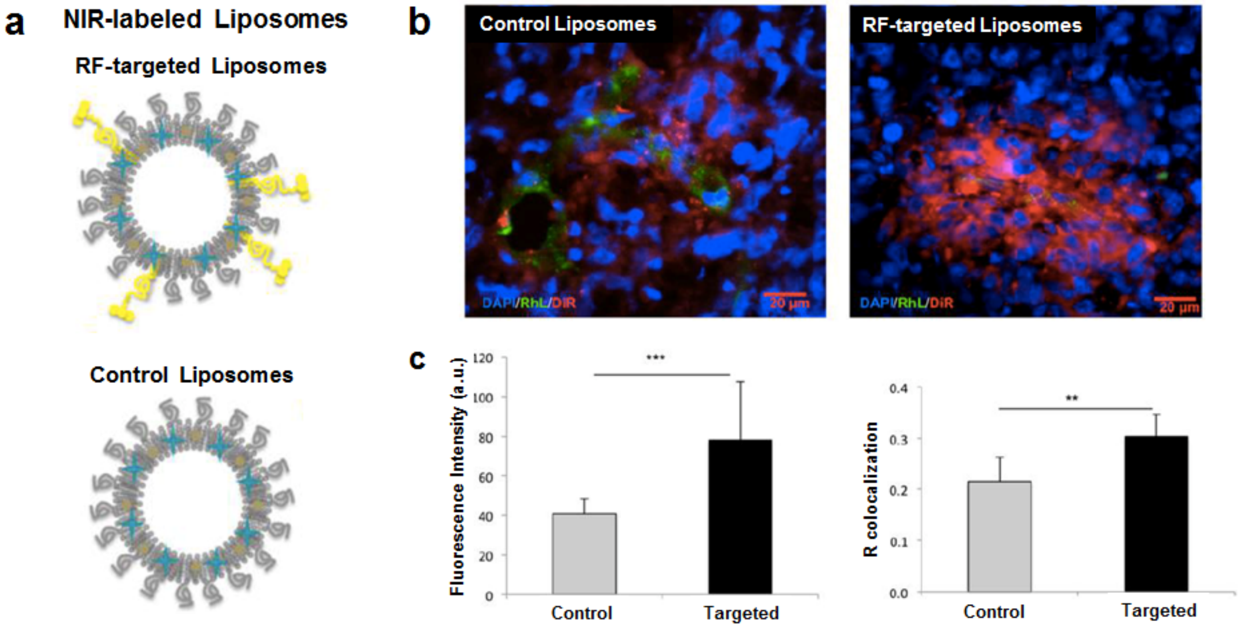

Figure 1.13 Evaluation of RF-targeted liposomes in CD1 nude mice bearing PC3 tumors (n=6). a: Schematic illustration of RF-targeted and control liposomes, b: Examples of fluorescence images of liposomes cellular uptake in the cancer lesion: liposomes (red), vessels (RhL, green), and cell nuclei (DAPI, blue), c: Quantification of the fluorescence signal in the tumor tissue, corresponding to the amount of internalized liposomes (right), and liposomes' colocalization with angiogenic vessels (left).[68] The image is adapted from Ref. 68.

In a follow-up study, the NIR dye was replaced with indocyanine green (ICG), which enabled the evaluation of the liposomes' tumor accumulation with photoacoustic imaging (PAI).[69] The accumulation in the cancer lesion of RF-targeted liposomes was measured to be 3.4 times higher than the control ones after 15 min, and 2.6 times higher after 4h after i.v. injection in CD1 nude mice bearing A431 tumor model (Figure 1.14). This data is in line with the previous study showing that RF-liposomes may be used as an efficient targeting agent for angiogenic vasculature.[69]

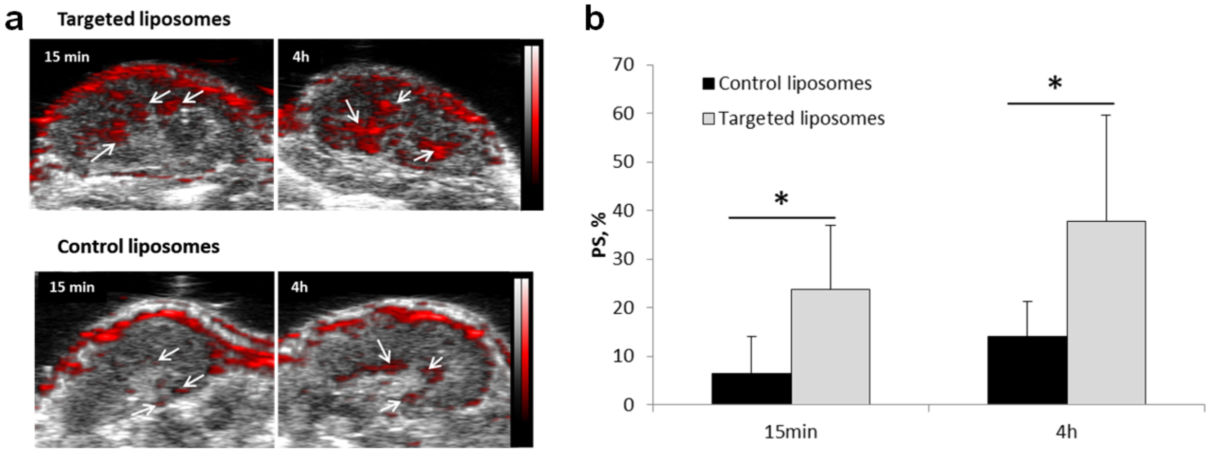

Figure 1.14 In vivo evaluation of RF-targeted and control liposomes in CD1 nude mice bearing A431 tumor model (n=5). a: Examples of 2D ultrasound (black and white) combined with photoacoustic (red) images of A431 tumors at different time points after i.v. administration of RF-targeted or control liposomes. Arrows show the liposomes' photoacoustic signal in the tumor. b: Quantification of the photoacoustic signal intensity in the tumors at different time 15 min and 4 h after liposome injection.[69] The image is adapted from Ref. 69.

Iron oxide Nanoparticles

Jayapaul et al. reported studies in which FMN and FAD were grafted on the surface of ultrasmall superparamagnetic iron oxide nanoparticles (USPIO) and were used as riboflavin-targeted MR contrast agents (Figure 1.15a and c).[70–72] These coatings not only increased the hydrophilicity of USPIO and prevented their aggregation, but also led to a RFT-specific uptake. FMN-coated and FAD-coated USPIO were shown to be intensely internalized by human umbilical vein endothelial cells (HUVEC) and the prostate cancer cells LnCaP in comparison with non-targeted magenetic nanoparticles.[70–72]

The targeted USPIOs (i.v. injection of 900 µmol Fe/kg) were also evaluated in vivo in CD1 male nude mice bearing LnCap prostate cancer xenografts. Animals treated with Resovist® (SPION coated with carboxydextran) served as a control group. A significantly stronger increase in R2* relaxation rates in tumors was reported for 1 h and 3 h after intravenous injection of FAD-USPIO, compared to Resovist® (FAD-USPIO vs. Resovist® at 1 h:

18.75 ± 6.96 s^{-1} vs. 5.92 ± 2.48 s^{-1}; 13.66 ± 4.05 s^{-1} vs. 4.56 ± 4.91 s^{-1} at 3 h), shown in Figure 1.15b. Competitive binding study with an excess of free FMN indicated that the in vivo cellular uptake of FMN-USPIO in LnCap xenographs is receptor-mediated. Significant decrease in R2* relaxation rates in the cancer lesion was measured for the competitive-binding group in comparison with the mice which received FMN-USPIO (free FMN and FMN-USPIO vs. FMN-USPIO at 1 h: 6.18 ± 3.84 s^{-1} vs. 22.28 ± 7.22 s^{-1}; 7.72 ± 3.57 s^{-1} vs. 18.78 ± 5.80 s^{-1} at 3 h), shown in Figure 1.15d. Histological analysis showed that both FAD-USPIO and FMN-UPSIO specifically and strongly accumulated in the endothelial cells of angiogenic blood vessel.[70–72]

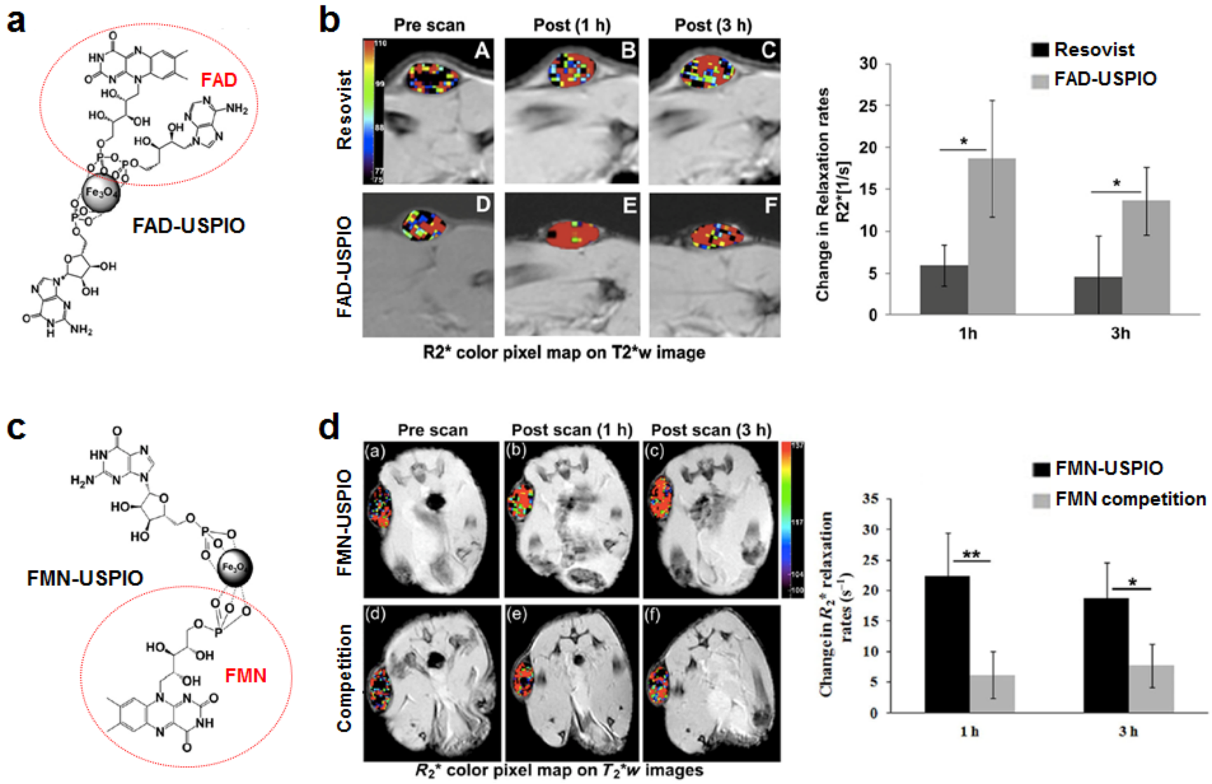

Figure 1.15 RF-targeted magnetic nanoparticles and their in vivo evaluation in prostate tumor models. a: Schematic illustration of FAD-coated USPIO., b: T2*w images at different time points of LnCap tumor lesion of CD1 nude mice after i.v. administration of FAD-USPIO and Resovist, c: Schematic illustration of FMN-coated USPIO, d: T2*w images at different time points of LnCap tumor lesion of CD1 nude mice after i.v. administration of FMN-USPIO alone and in a competitive binding study with FMN.[70–72] The image is adapted from Ref. 70-72.

Furthermore, Mertens et al.[73] showed that FMN-USPIOs were also highly efficient for cell labeling (fibroblasts, smooth muscle cells and endothelial cells) and subsequent cell imaging in tissue-engineered implants.

In conclusion, although RF uptake mechanisms remain to be explored, the summarized preclinical data presented in this chapter show that targeting RFT/RCP is simple, highly efficient and holds a great potential in imaging, drug delivery and cell labeling. Stimulated by these encouraging preclinical results, the following thesis work focuses on the further development, improvement and evaluation of RF-targeted nanosystems for cell labeling and drug delivery.

Chapter 2

2. Objectives

The scope of this thesis is the synthesis, characterization, and evaluation of riboflavin-targeted diagnostic and theranostic nanocarriers with different imaging modalities. The thesis comprises two projects which focused on:

1. cell labeling with riboflavin-modified iron oxide nanoparticles and their evaluation with magnetic resonance imaging;
2. passive and active tumor targeting with riboflavin-functionalized polymers and their evaluation with fluorescence molecular tomography.

The objectives of the first study was to stabilize riboflavin-targeted ultrasmall paramagnetic iron oxide nanoparticles (USPIO) by grafting different biomolecules on their surface and to analyze how the USPIO coating influences the physicochemical properties of the nanoparticles and their cellular uptake.

The goals of the second study were to design fluorescent riboflavin-targeted polymers and to evaluate how their size and functionalization influence the biodistribution, targeting efficiency, and tumor accumulation in mouse models by using computed tomography combined with fluorescence molecular tomography.

Chapter 3

3. Riboflavin-targeted iron oxide nanoparticles

The content of this chapter and major text passages have been published in the journal of *Contrast Media Mol. Imaging* 2016, 11, 47-54 [74] with the following title:

"Refinement of adsorptive coatings for fluorescent riboflavin receptor targeted iron oxide nanoparticles"

Flavin-targeted ultrasmall superparamagnetic iron oxide particles (USPIO) were stabilized with the adenosine phosphates – AMP, ADP and ATP. It is shown that these stabilizing molecules significantly influence the contrast agent's properties and its cellular uptake, e.g. by changing the flavin amount on the UPSIO surface which regulates the receptor-mediated internalization.[74]

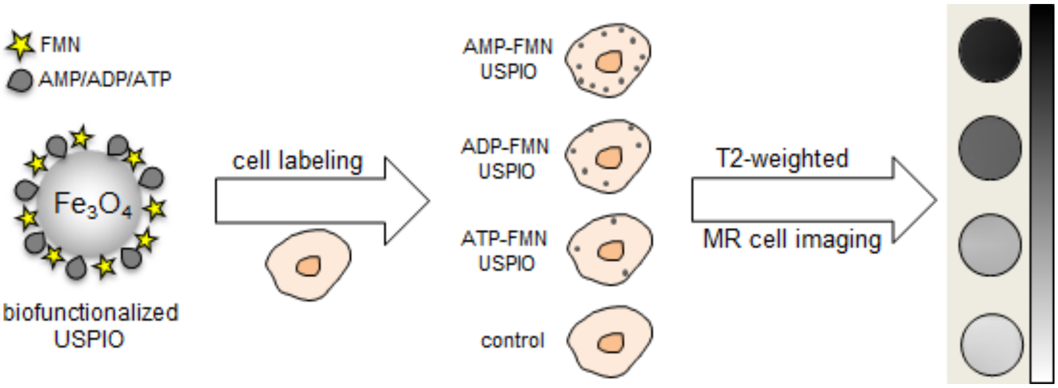

Contrast Media Mol. Imaging 2016, 11, 47-54

Abstract

Flavin mononucleotide (FMN) is a riboflavin derivative that can be exploited to target the riboflavin transporters (RFTs) and the riboflavin carrier protein (RCP) in cells with high metabolic activity. This study presents the synthesis of different FMN-coated ultrasmall superparamagnetic iron oxide nanoparticles (USPIO) and their efficiency as targeting contrast agents. Since FMN alone cannot stabilize the nanoparticles, different adenosine phosphates – adenosine monophosphate (AMP), adenosine diphosphate (ADP) and adenosine triphosphate (ATP) were used as spacers to obtain colloidally stable nanoparticles. Nucleotides with di- and triphosphate groups were intended to increase the USPIOs charge and thus improve their stability. However, all nanoparticles formed negatively charged clusters with similar properties in terms of zeta potential (-28 ± 2 mV), relaxivity (228 - 259 $mM^{-1}s^{-1}$ at 3T) and hydrodynamic radius (R_h 53 - 85 nm). Molecules with a higher number of phosphate groups, such as ADP and ATP, have a higher adsorption affinity towards iron oxide which instead of providing more charge on the particles' surface, led to partial desorption and replacement of FMN. Hence, the obtained USPIOs carried different amount of targeting agent (FMN) which significantly influenced the cellular uptake of the nanoparticles. The nanoparticles' uptake by different cancer cells and Human umbilical vein endothelial cells (HUVEC) was evaluated photometrically and with MR relaxometry showing that the cellular uptake of the USPIOs increases with the FMN amount on their surface. Thus, for USPIO targeted with riboflavin derivatives the use of spacers with increasing numbers of phosphate groups does not either increase zeta potential, or improve particles' stability, but rather detaches the targeting moieties from their surface leading to lower cellular uptake. [74]

3.1 Introduction

Iron oxide nanoparticles are clinically approved MR contrast agents and have a broad application in the biomedical field, for example in diagnostics, drug delivery and cell tracking. Magnetic nanoparticles without surface coating, however, are not stable under physiological conditions and tend to aggregate and precipitate due to hydrophobic interactions between the particles, van der Waals forces, and high energy surface.[75] Therefore, the stabilization of the iron oxide particles is a crucial step in the synthesis and is necessary to obtain a stable magnetic colloidal suspension in biological medium and magnetic field.[76] In order to stabilize the iron oxide nanoparticles, their surface is often modified with polymers or small molecules, which provide an electrostatic or steric repulsion among the particles and thus prevent their agglomeration.[76] The stabilizing agents can be either adsorbed on the particles' surface through phosphate, sulfate and carboxy groups or covalently bound to the iron oxides, such as organosilanes. In addition, the surface may be functionalized with targeting ligands like antibodies, proteins or peptides so that the iron oxide nanoparticles can be applied as targeted contrast agents for diagnostics and therapy.

Jayapaul et al.[70–72] presented the synthesis and surface modification of ultrasmall superparamagnetic iron oxide nanoparticles (USPIO) for targeting riboflavin transporters (RFTs) and riboflavin carrier protein (RCP). The USPIOs were coated with different small biomolecules carrying phosphate groups, which were adsorbed on particles' surface - flavin mononucleotide (FMN) and guanosine monophosphate (GMP). FMN was used as targeting ligand and GMP was applied to provide sufficient surface coverage to prevent particles precipitation. GMP-FMN coated USPIOs were efficiently used for RFT/RCP targeting of prostate cancer and activated endothelial cells in vitro and in vivo.[70,72] Furthermore, it was shown that these nanoparticles are highly efficient for cell labeling and cell imaging in tissue-engineered implants.[73]

The objective of this study is to improve the stability of FMN-targeted USPIOs by applying new stabilizing agents. GMP, used by Jayapaul et al., was replaced with the nucleotides adenosine monophosphate (AMP), adenosine diphosphate (ADP) and adenosine triphosphate (ATP). Small molecules carrying higher number of phosphate groups are suggested to provide more charge to the particles and thus increase their stability. Furthermore, it was aimed to evaluate how the different stabilizing agents change the physicochemical properties of the nanoparticles and how these influence the cellular uptake.[74]

3.2 Results and Discussion

Synthesis and surface modification of USPIO

USPIOs were prepared with a coprecipitation technique by adding ferric and ferrous salts in alkaline solution.[76] The obtained particles were then washed and preserved in 0.1 M HCl solution. In aqueous solution, the iron atoms on the particles' surface function as Lewis acid and accept lone-pair of electrons donated from the surrounding water molecules. When coordinated to the iron atoms, water dissociates, and the iron oxide particles become functionalized with hydroxy groups on their surface.[76] Since these hydroxy groups are amphoteric, they react with acids and bases.[77] Therefore, bare ironoxide nanoparticles are positively charged in acidic and negatively charged in basic solution. This surface charge provides electrostatic repulsion and the particles are colloidaly stable at low and high pH values. The isoelectric point is determined at pH 6.8 [78], meaning that the bare particles are no longer charged at physioplogical pH, become less stable due to the lack of electrostatic repulsion and begin to sediment. Therefore, to stabilize the bare nanoparticles at physioplogical pH, they were first coated with FMN.

FMN adsorbs on the iron oxide nanoparticle's surface and makes it specific towards the RFTs and RCP. However, coating USPIO only with FMN resulted in less stable particles which gradually agglomerated. Figure 3.1a shows freshly prepared FMN-USPIO, which had a mean core radius of 5.5 ± 1.7 nm. After short time the particles began to form agglomerates with a size in micrometer range, as shown in Figure 3.1b. The agglomerates could be temporarily dispersed by sonication, but after short period of time sedimentation was observed. Flavin mononucleotide probably cannot cover the complete USPIO surface, most likely due to steric effects of the bulky isoalloxazine rings, which could prevent a dense FMN population on the iron oxide surface.[74]

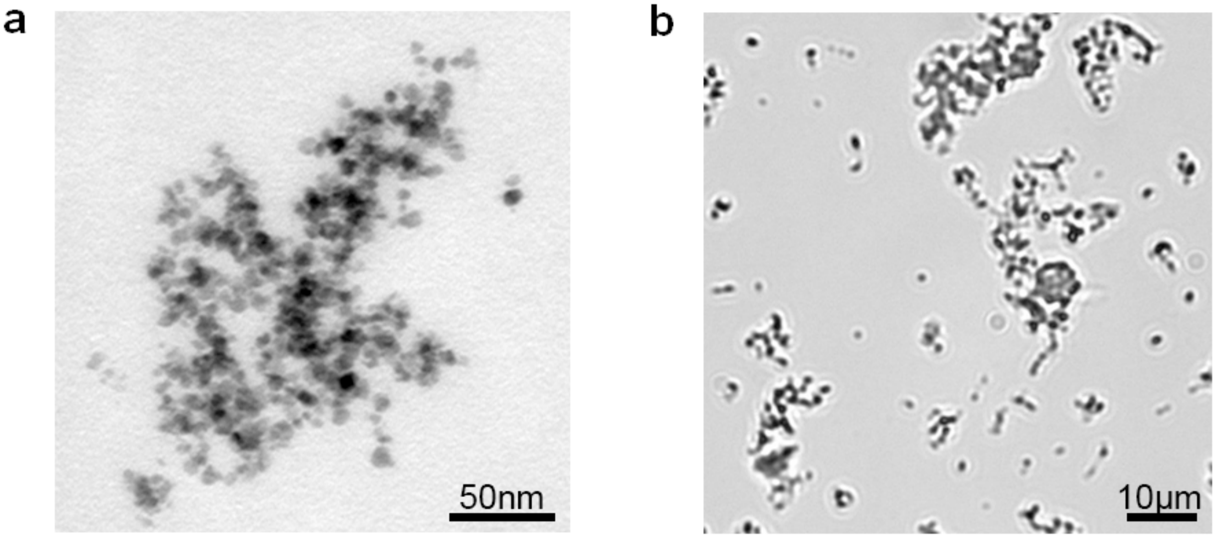

Figure 3.1 Microscopy images of USPIO grafted with FMN. a: TEM image of freshly prepared FMN-coated USPIO, b: Optical microscopy image of aggregated FMN-coated USPIO.[74] The image is adapted from Ref. 74.

In order to achieve long-term stability, less bulky molecules which can fill the gaps between the flavin mononucleotides needed to be used as spacers. Nucleotides such as GMP, AMP, UMP and TMP are suitable for this purpose since they are small and biocompatible, and contain a phosphate group by which they can get attached to the iron oxide surface. Furthermore, their purine or pyrimidine moieties may also form hydrogen bonds with the FMN isoalloxazine imide, which would result in a denser coating around the USPIO core and prevent sedimentation.[74]

Stable FMN-USPIOs could be obtained by adding adenosine mono-, di- or triphosphate to the nanoparticles suspension, which got adsorbed on the iron oxide surface, as depicted schematically in Figure 3.2. Higher number of phosphate groups per molecule were expected to provide more charge to the nanoparticles and thus increase zeta potential and stability. The three nucleotides - AMP, ADP and ATP provided sufficient electrosteric stabilization to prevent agglomeration of the FMN-USPIO and delivered colloidally stable nanoparticles.[74]

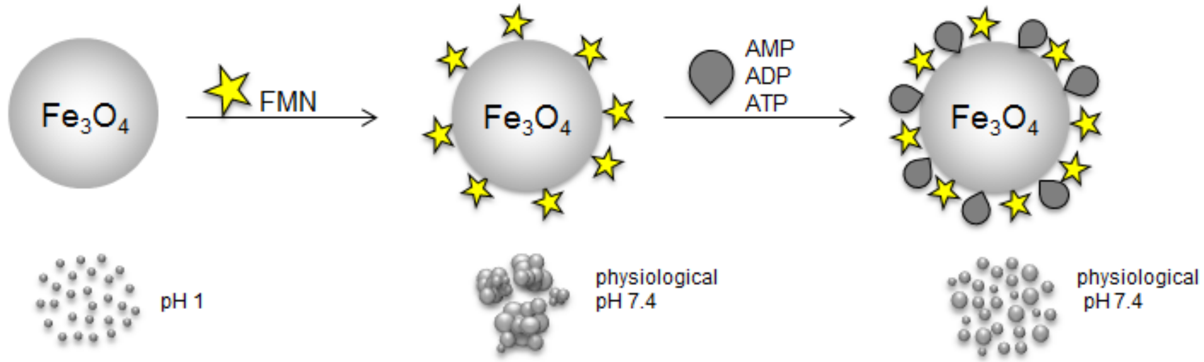

Figure 3.2 Schematic synthesis route of fluorescent monomer-coated USPIO.[74] The image is adapted from Ref. 74.

The coated USPIOs were purified by magnetophoresis and further dialyzed to completely remove unbound monomers. After dialysis in 25 mM HEPES buffer at physiological pH, the particles remained stable which indicated no depletion of the coating layer.[74]

Different stabilizing molecules grafted on the USPIO surface may influence the particles' properties in terms of size, charge, polydispersity, and coating layer. These properties are also important for the cellular uptake of the particles and were further analyzed in detail. [74]

Size and charge of the coated USPIO

The physicochemical characterization of the coated nanoparticles was performed by transmission electron microscopy (TEM), dynamic light scattering (DLS) and zeta potential measurements. The core size and the shape of the coated particles were determined through TEM measurements. The obtained images were similar for the differently stabilized USPIO as shown in Figure 3.3. The nanoparticles had spherical morphology with an average core radius of around 5 ± 1.5 nm (Table 3.1). The hydrodynamic size of the particles was evaluated with DLS. Compared with the size of their cores, the iron oxide nanoparticles displayed much larger hydrodynamic radii: 53 nm for ATP- and around 85 nm for AMP- and

ADP-stabilized particles, which indicated that the monomer-coated USPIOs tend to form clusters.[74]

Table 3.1 Nanoparticles' properties in HEPES, pH 7.4 [74] The table is adapted from Ref. 74.

	R_{core} (nm)	R_h (nm)	Zeta potential (mV)	PDI	MR Relaxivity at 3T ($s^{-1}mM^{-1}$)	
					r1	r2
AMP-FMN USPIO	4.9 ± 1.6	80 ± 1	-27 ± 1	0.17	1.56 ± 0.1	228 ± 3
ADP-FMN USPIO	5.1 ± 1.3	84 ± 2	-29 ± 1	0.22	1.05 ± 0.1	233 ± 9
ATP-FMN USPIO	5.2 ± 1.5	53 ± 1	-28 ± 1	0.2	3.16 ± 0.2	259 ± 8
RESOVIST	4.2	36 ± 1	-36 ± 2	0.19	6.84	233 ± 1

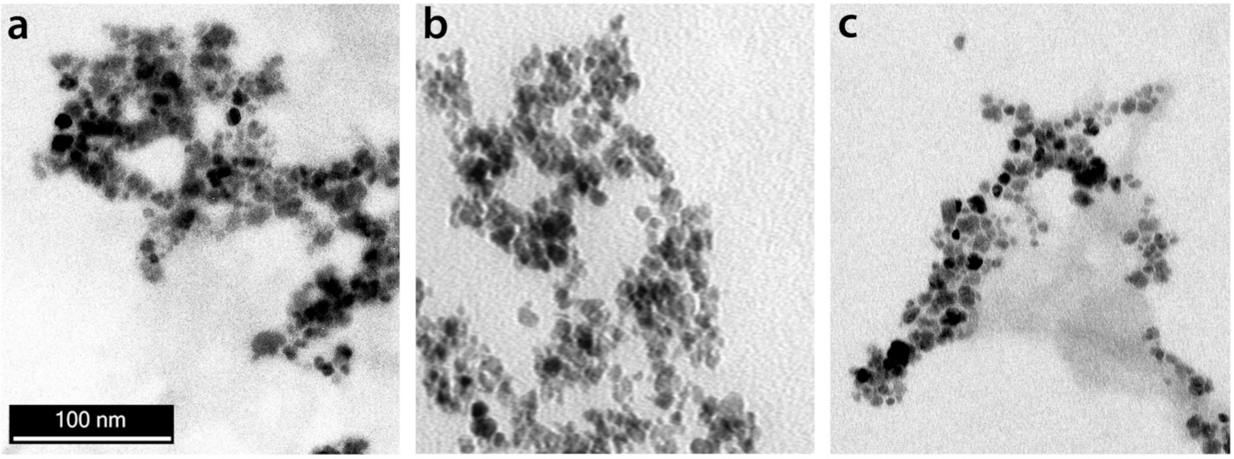

Figure 3.3 TEM image of a: AMP-FMN USPIO, b: ADP-FMN USPIO and c: ATP-FMN USPIO.[74] The image is adapted from Ref. 74.

Zeta potential measurements showed that the different spacers did not influence the particles' properties significantly in terms of charge and stability. Zeta potential was measured -28 ± 2 mV for all nanoparticles. These data showed that grafting nucleotides with more phosphate groups on the nanoparticles' surface did not increase the USPIOs charge. This could be explained by similar amount of phosphate moieties on the USPIO surface among the three different types of nanoparticles. The total amount of phosphate groups adrsorbed on the iron oxides could be measured photometrically and was normalized to the iron content. Photometric phosphate determination showed comparable values for the AMP-, ADP- and ATP- stabilized particles (0.41 ± 0.04, 0.43 ± 0.12 and 0.46 ± 0.1 µmol PO_4^{3-} /mg Fe), which could explain their similar surface charge.[74]

Relaxometry

MR relaxometry measurements were carried out to determine the relaxivities of the iron oxide particles. The r1 and r2 values of the nanoparticles were obtained by linear regression of the transversal relaxation rates at 3.0 T as a function of iron concentration. ATP-stabilized USPIO had slightly higher r2 relaxivity (259 ± 8 $s^{-1}mM^{-1}$) compared to the AMP and ADP counterparts (228 ± 3 and 233 ± 9 $s^{-1}mM^{-1}$). This difference was likely due to the smaller size of ATP-FMN-USPIOs. For equal iron concentrations, smaller nanoparticles provide more surface area and thus can interact with more water molecules, which increases the relaxation rate. This assumption also explained the similar tendency for the r1 relaxivity, as the highest r1 value of 3.16 ± 0.2 $s^{-1}mM^{-1}$ was measured for the ATP-stabilized USPIO in contrast to 1.05 ± 0.1 and 1.65 ± 0.1 $s^{-1}mM^{-1}$ for the ADP- and AMP-FMN nanoparticles. Nevertheless, the relaxivity values of the nanoparticles are similar to those of the commercial MR contrast agent Resovist. Resovist is a polydisperse carboxydextran-coated SPIO with an average core diameter of 4.2 nm [79], and an average hydrodynamic radius of 36 nm [79] with r2 value of 233 ± 1 $s^{-1}mM^{-1}$ and r1 of 6.84 $s^{-1}mM^{-1}$ [79]. [74]

Coating layer

As already described in the nanoparticles synthesis, the USPIOs surface layer consisted of FMN and adenosine phosphates. Flavins are intrinsically fluorescent due to the isoalloxazine ring and have an absorption maximum in the VIS range at 450 nm and display fluorescence emission peak at 530 nm.

Therefore, fluorescence intensity measurements at 530 nm could be used to determine the FMN amount grafted on the USPIOs. The spectra showed that the amount of FMN bound to USPIO surface varied among the particles. The emission intensity of the nanoparticles decreased significantly with the addition of the spacers (Figure 3.4), which indicated that FMN was partially replaced by the adenosine phosphates.[74]

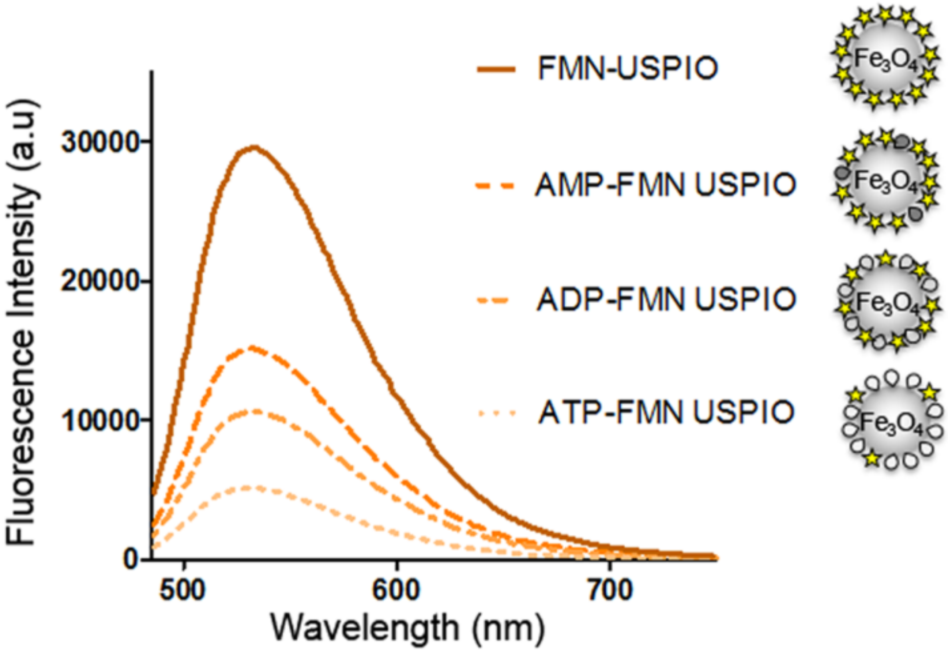

Figure 3.4 Fluorescence intensity of FMN-USPIO without nucleotides, and FMN-grafted USPIO stabilized with AMP, ADP or ATP in HEPES buffer at pH 7.4 (0.01 mmol Fe/l).[74] The image is adapted from Ref. 74.

AMP-stabilized USPIO showed the highest emission intensity among the nucleotide stabilized particles and consequently carried the highest amount of FMN (0.20 ± 0.06 μmol/mg Fe). The fluorescence intensity decreased in the case of ADP (0.1 ± 0.02 μmol FMN/mg Fe), and using ATP for stabilizing the nanoparticles led to the lowest amount of FMN bound to the USPIO surface (0.06 ± 0.01 μmol/mg Fe). This tendency could be explained by the different adsorption affinities of the spacers to iron oxide and steric effects, both of which due to the different number of phosphate groups. The adsorption affinities of organophosphates onto iron oxide, have been already extensively studied and shown to be stronger with increasing number of free phosphorous-oxygen moieties.[80] The adsorption affinity of adenosine phosphates was reported as follows: ATP>ADP>AMP. ADP is adsorbed more strongly than AMP due to the presence of the P_2O_6 group. The effect of the P_3O_9 group is similarly pronounced in the adsorption of ATP. Among the three nucleotides, ATP is reported to be adsorbed most favorably.[80] Since the adenosine phosphates are given to already FMN-grafted USPIOs, they may induce partial desorption and replacement of the flavin coating. This effect would be more prominent with increasing adsorption affinity and steric demand of the nucleotides (ATP>ADP>AMP). This assumption is in line with the fluorescence intensity measurements, which showed a gradually decreasing FMN amount according to the number of phosphate groups of the nucleotides. [74]

The overall physicochemical characterization of the monomer-coated iron oxide nanoparticles showed that the nucleotides AMP, ADP and ATP could be successfully used to stabilize FMN-targeted USPIO and provided similar charge and stability. The nanoparticles had comparable relaxivities with exception for ATP-stabilized USPIO that displayed enhanced r2 and r1 relaxivities consistent with the smaller hydrodynamic radius. The spacers influenced mainly the coating of the nanoparticles as they varied the amount of FMN bound to the surface.[74]

Biocompatibilty

Biocompatibility and toxicity are critical factors that need to be considered for the in vivo application of contrast agents and nanocarrier systems. In the case of iron oxide nanoparticles, there are numerous factors which may have an impact on their biocompatibility and toxicity such as size, charge, surface chemistry, dose, and agglomeration state.[81] However, it is generally accepted that cells and mammalian organisms can cope well with iron oxides, since iron oxides can be degraded and utilized by cells via the physical iron metabolism pathway.[82] The coating materials used in this study are biomolecules and were not toxic in the used concentrations. MTT assay was used to evaluate the cytotoxicity of the monomer-coated USPIOs in HUVEC and PC3 cells, at 0.03, 0.3 and 3 mM iron concentrations (Figure 3.5). The cells were incubated with the nanoparticles for 1 h and the cell viability was analyzed after 72 h. The short incubation time was chosen since it is sufficient to achieve high cellular uptake and a strong shortening in R2* in MRI. Under these conditions, no decrease in the cells' viability was observed after 72 h which indicated that the monomer-coated nanoparticles were well tolerated by the cells. These results were in line with previous experiments, reported by Mertens et al., in which the cytotoxicity of GMP-stabilized FMN-USPIO, uncoated USPIO and clinically approved iron oxide nanoparticles (Sinerem) was analyzed.[73] None of the nanoparticles caused a significant decrease in viability of HUVEC and smooth muscle cells [73]. [74]

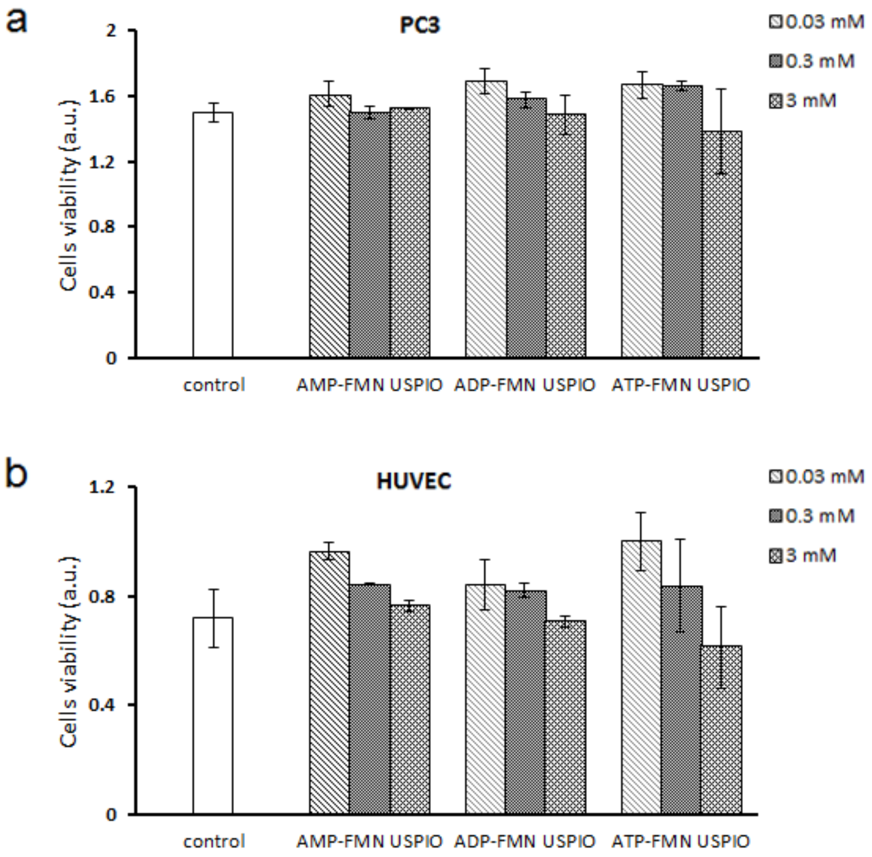

Figure 3.5 Viability of a: PC3 cells and b: HUVECs, 72h after incubation with monomer coated USPIO. Control cells were incubated with cell culture medium only. No statistically significant difference was found between the groups.[74] The image is adapted from Ref. 74.

<u>*In vitro studies*</u>

FMN is the targeting ligand which initiates the cellular internalization of the particles through the riboflavin transporters. Since the nanoparticles carried different flavin amounts on the surface, it was essential to check whether this would have an impact on their targeting efficiency. Therefore, the nanoparticles uptake was evaluated for different cancer cell lines (PC3, LnCaP, MLS, MCF-7, A431) and for endothelial cells (HUVEC). The cells were incubated with the USPIOs, washed to remove the non-internalized particles, embedded in gelatin, and MR relaxometry measurements were performed to assess the degree of USPIO uptake. Since the nanoparticles had similar r2 values, the relaxivity of the gelatin cell suspension is likely to be directly proportional to the amount of internalized particles. Although the extent of vitamin receptor overexpression and ligand selectivity may vary by cancer type, the results showed a clear tendency in the cellular uptake (Figure 3.6) - the AMP-stabilized particles' take-up by the cells was three to five times higher than the take-up of the ADP- and ATP-stabilized nanoparticles. The measurements showed a tendency in the cellular uptake, correlated to the amount of targeting ligand on the USPIO surface. Although the nucleotides did not initiate any specific cellular uptake, they considerably altered the targeting efficacy of the USPIOs. The application of spacers resulted in variable amounts of FMN adsorbed on the USPIO surface, which had a significant influence on the cellular internalization. Particles stabilized by nucleotides with less sterically demanding adsorptive sites, like AMP, carried a much higher amount of FMN than those stabilized by ATP. This is why AMP stabilized particles were taken up by cells to a significantly higher extent.[74]

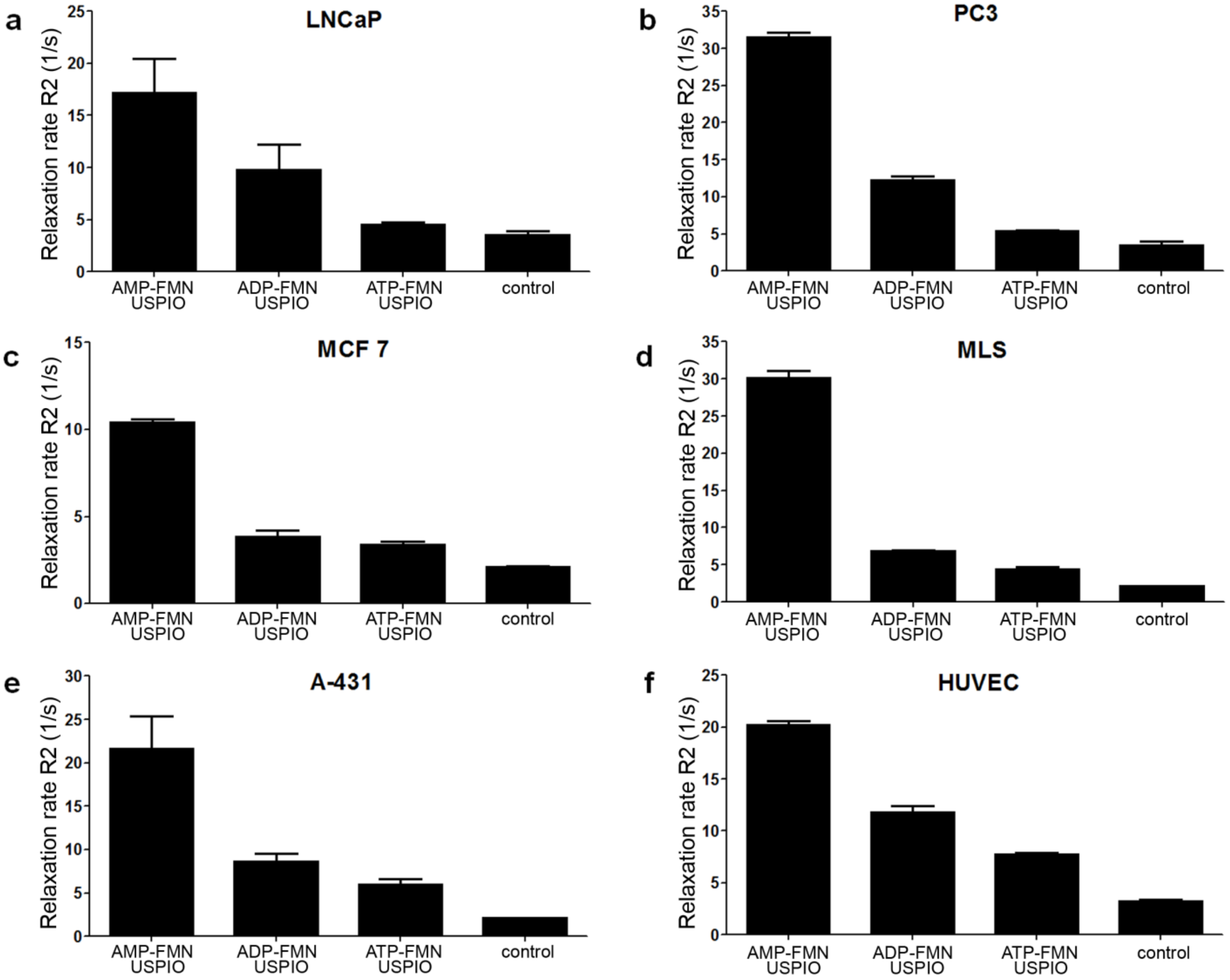

Figure 3.6 3D T2-relaxivity measurements of cells in a 0.3 ml 10wt%-gelatin solution. a: LNCaP, b: PC3, c: MCF7, d: MLS, e: A-431, cells (2x10^6 cells) and f: HUVEC (0.5x10^6 cells).[74] The image is adapted from Ref. 74.

Subsequently, the cellular uptake determined by the MR relaxivity measurements was validated with Prussian blue staining, as illustrated in Figure 3.7 a-d. In addition, the uptake of the coated USPIO was analyzed photometrically. After incubation with the nanoparticles, the cells were lysed with aqua regia, in which the internalized nanoparticles were oxidized to Fe^{3+} ions. The pH of the solution was then adjusted to 9.5 so that Fe^{3+} could form a colored complex with tiron (4,5-Dihydroxy-1,3-benzenedisulfonic acid). The complex had an absorption maximum at 480 nm and thus by measuring the absorbance at this wave length, the iron amount in the cells could be quantified. The photometrical analysis, presented in

Figure 3.7e, were in line with the MRI data and showed an enhanced uptake for the nanoparticles with the highest amount of FMN on the surface. [74]

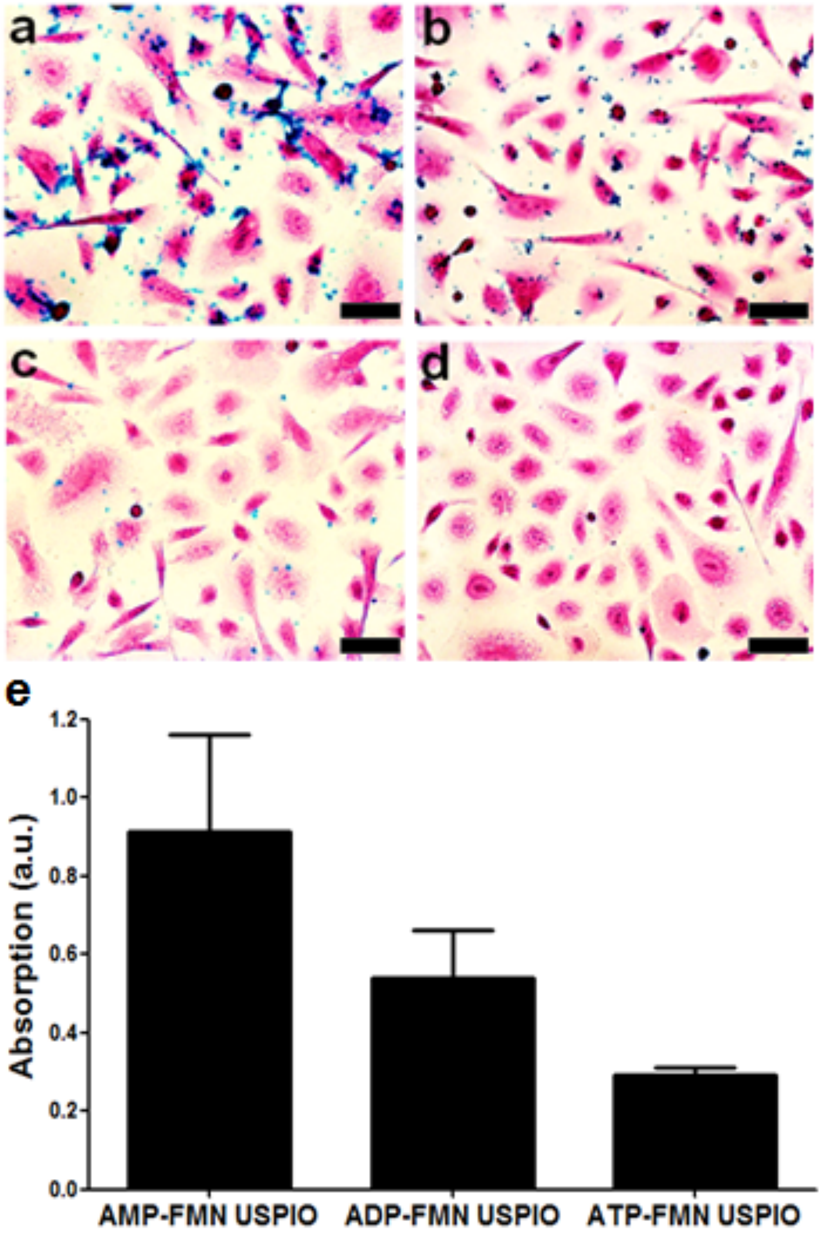

Figure 3.7 Prussian blue staining a-d: PC3 cells incubated with nanoparticles for 1h (0.6 µmol Fe/mL) a: AMP-FMN USPIO, b: ADP-FMN USPIO, c: ATP-FMN USPIO, d: control cells. Scale bar 50 µm, e: Photometric determination of the iron content proportional to the internalized nanoparticles in 0.5×10^6 PC3 cells.[74] The image is adapted from Ref. 74.

Finally, competitive binding experiments were performed to confirm that the cellular uptake was due to presence of FMN on the particles' surface. For this purpose, PC3 cells were pre-incubated with free FMN (3 µmol/ml) to saturate the receptors before adding the nanoparticles. The cellular uptake was measured with MRI and photometrically. T2-weighetd MRI data (Figure 8a) showed that the nanoparticles uptake of cells preincubated with FMN decreased significantly - the relaxation rate decreased from 31.5 ± 0.7 to 6.0 ± 0.6 s^{-1}, $p < 0.001$. The competitive binding experiments indicated that the nanoparticles internalization was receptor-mediated. Resovist was used as negative control, in order to evaluate the amount of non-specific cellular uptake of iron oxide nanoparticles. The cells incubated with Resovist showed relaxation rate of 4.2 ± 0.2 s^{-1}, which was 7.5 times lower than the relaxation rate of the cells treated with AMP-FMN USPIO (31.5 ± 0.7). Photometric iron measurements of PC3 cells showed similar tendency (Figure 3.8b). The in vitro results demonstrated that modifications in the coating layer of the particles were essential for their targeting ability. Since FMN is bound to the USPIO surface through phosphate groups, it is prone to desorb in the presence of molecules which have a higher affinity to bind to iron oxide. Spacers with di- or triphosphate moieties, initially expected to increase the particles' stability by adding more charge, decreased the amount of FMN and thus the specific uptake of the particles. The relaxation rate of cells treated with ATP-FMN USPIO (5.3 ± 0.2 s^{-1}) was only slightly higher from that of non-targeted SPION Resovist (4.2 ± 0.2 s^{-1}). Although FMN was present on the surface of the ATP stabilized particles, its amount was most likely not sufficient for an optimal interaction with the riboflavin carrier protein or the RFTs of the cells. Among the three tested spacers, AMP retained the highest amount of FMN on the USPIO surface and is for this reason the preferred molecule.[74]

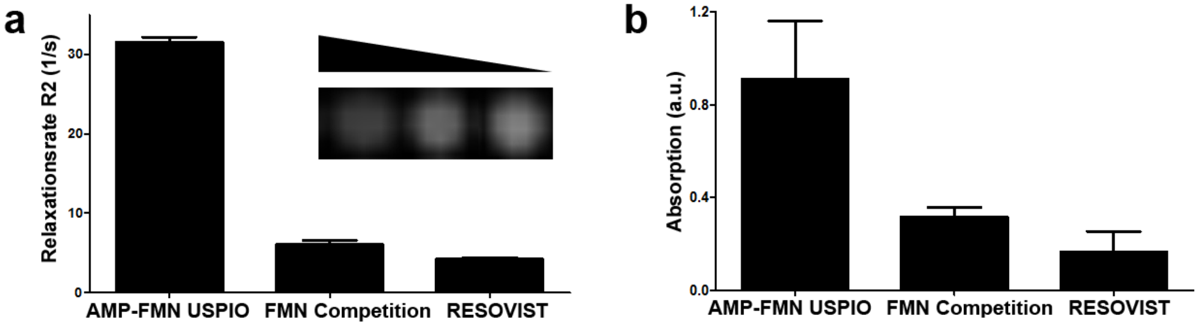

Figure 3.8 Nanoparticles' uptake in basal and FMN containing media. a: MRI relaxometry measurements of $2x10^6$ PC3 cells in a 0.3 ml 10wt%-gelatin solution, b: Photometric iron measurements with tiron of $0.5x10^6$ PC3 cells.[74] The image is adapted from Ref. 74.

3.3 Conclusion

The nucleotides AMP, ADP and ATP were evaluated as spacers to stabilize FMN-targeted iron oxide nanoparticles. It was shown that spacers with more phosphate groups did not increase the stability and zeta potential of the iron oxide nanoparticles but rather replaced the targeting ligand FMN from their surface. This led to a decrease in cellular uptake, which is mediated by RCP/RFP binding as indicated by competitive binding experiments. Taking these arguments into account and considering that the type of spacer has only marginal effects on the particles' relaxivities, AMP seems to be the preferred molecule for stabilizing FMN-targeted USPIO.[74]

3.4 Experimental

The description of all experimental procedures was adapted from Tsvetkova et al. Ref. 74.

Iron oxide nanoparticles synthesis and surface modification

USPIO nanoparticles were prepared and purified as described by Jayapaul et al.[70] Briefly, the particles were synthesized by coprecipitation of ferric and ferrous salts in alkaline solution, at pH 12. After magnetic filtration, the bare cores (5 ± 1nm) were coated with a thin layer of small biomolecules, which get adsorbed on the USPIO surface through phosphate groups. The monomer coating was performed in two steps. USPIOs were first incubated with 0.04 mmol FMN (Sigma Aldrich, Steinheim, Germany) at room temperature for 1 h. Afterwards, 0.06 mmol nucleotide: AMP, ADP or ATP (AppliChem, Darmstadt, Germany) were added to the FMN coated USPIO and sonicated for 1 h at room temperature. After each coating procedure the nanoparticles were washed with 25 mM HEPES buffer (pH 7.4) by a high-gradient magnetophoresis. Finally, the nanoparticles were centrifuged at 867 g for 15 mins to remove aggregates.[74]

Nanoparticles characterization: DLS, Zeta Potential, Fluorescence Intensity

Size distribution, polydispersity and electrophoretic mobility measurements were performed with Zetasizer Nano ZS, Malvern Instruments at 20°C, using the General Purpose algorithm. DLS was performed at scattering angle of 173°. Zeta potential was calculated using Smoluchowski model.

The fluorescence emission spectra of the nanoparticles were measured with TECAN Reader *M200 pro* spectrometer. The excitation wavelength was 450 nm and the fluorescence intensity maximum was measured at 530 nm.[74]

Cell lines

HUVEC (human umbilical vein endothelial cells), PC3 (human prostate cancer cells), LNCaP (human prostate adenocarcinoma cells), A-431 (human epidermoid carcinoma cells), MLS (human ovarian carcinoma cells) and MCF7 (human breast cancer cells) were obtained from ATCC (Wesel, Germany) and used for cellular uptake and cytotoxicity analysis. HUVEC were cultivated in Endopan 3 Medium (Pan Biotech GmbH, Aidenbach, Germany), PC3 in McCoy, MLS in F-12, LNCaP, A-431in RPMI, MCF7 in DMEM supplemented with 10% FCS and 1% Pen/Strep, obtained from Gibco, Invitrogen, Germany. All cell lines were cultured at 37°C in a humidified atmosphere of 5% CO_2.[74]

MR assessment of particle uptake by cells

After reaching about 80% confluence, cells were incubated with 0.3 µmol Fe/mL nanoparticles for 1 h. The cells were washed thrice with PBS (Gibco, Invitrogen, Germany), trypsinized, counted and centrifuged. The cell pellet was dissolved in 10% gelatin solution to obtain $2x10^6$ cells/0.3 ml/well in a 96-well plate. Each experiment was done in triplicate. The relaxivity of the gelatin cell suspensions was measured in a clinical 3T whole-body MR scanner (PHILIPS Achieva, The Netherlands) using a SENSE-flex-M coil (PHILIPS, The Netherlands).[74]

MR Relaxometry

Relaxivities r1 and r2 were determined by a linear fit of the relaxation rates (R1 and R2) as a function of the iron concentrations.

The following MR sequences were applied for relaxometry:

T_2-weighted multi-slice, multi shot spin echo sequence [TR = 1500 ms, TE = 11.8-235.8 ms, number of echoes = 20, FOV = 130×162.5×18 mm, scan resolution = 64×81, voxel size = 2×2×3, slice orientation: coronal, scan mode = 3 D]

T_1-weighted turbo field echo sequence [Turbo Factor = 4, TR = 4.3ms, TE = 2.3 ms, number of echoes = 1, FOV = 223×223mm, scan resolution=112×108, voxel size = 1.12 ×1.11, slice thickness=2 mm, slice orientation= coronal, scan mode= 2D, Inversion delay time (T_I) ranges from 31 ms to 4437 ms, ΔT_I = 22 ms].[74]

MTT Cytotoxicity assay

PC3 cells and HUVECs were seeded into 96-well plates at a density of 5 x 10^4 cells/well. The cells were incubated with AMP-USPIO, ADP-USPIO and ATP-USPIO in concentrations of 0.03, 0.3 and 3 mmol Fe/ml for 1 h, washed thrice with PBS and maintained in culture media for 72 h. MTT solution (5 mg/mL) was added to the cells and left for 3 h at 37°C. After removal of the MTT solution, DMSO was added to dissolve the formazan chrystals and left overnight at RT. The absorbance of the DMSO solution was measured at 570 nm (with 690nm as reference) and is proportional to the cells' viability. The percentage of viable cells was determined relative to untreated cells.[74]

Prussian Blue Staining

Prussian Blue staining was performed to visualize intracellular iron. The cells were seeded on glass cover slips, incubated with nanoparticles for 1 h and washed thrice with PBS. Afterwards the cells were fixed with 4% polyformaldehyde in PBS, washed and incubated with 5% potassium ferrocyanide (Sigma Aldrich, Steinheim, Germany) in 10% hydrochloric acid. Cells were washed again, counterstained with nuclear fast red and evaluated for iron staining using light microscopy (Zeiss Imager D.1, AxioCam MRc, Axio SW).[74]

Photometric Determination of Phosphate[83]

Nanoparticle suspension (100 µl) was mixed with 70-72% $HClO_4$ (100 µl) and heated at 200 °C for 45 min. After cooling down to room temperature, the sample was mixed with 1 ml reagent (22.9 mM sodium molybdate, 2.1 mM hydrazine chloride, 1.6 mM HCl and 270 mM H_2SO_4 in water) and heated in boiling water bath for 20 min. After cooling, 1.5 ml of 0.5 M H_2SO_4 was added to the mixture. The absorption of the obtained phosphomolybdenum blue was measured at 820 nm.[74]

Photometric Determination of Fe^{3+}

PC3 cells were incubated with 0.3 µmol Fe/mL nanoparticles for 1 h, washed trice with PBS, trypsinized, counted and centrifuged. Aqua regia (30 µl; 11.6 M HCl: 15.8 M HNO_3, volume ratio 3:1) was added to $2x10^6$ cells, which were redisprersed in 100 µl PBS. Then, the cell suspension was heated in a boiling water bath for 15 min. Subsequently, 20 µl of 0.25 M tiron water solution, 100 µl 4M NaOH and 200 µl 0.2 M Phosphate buffer (pH=9.5) was added to the cell suspension. The absorption of the Fe^{3+} -tiron complex was measured at 480 nm.[74]

Chapter 4

4. Riboflavin-targeted polymers

The content of this chapter and major text passages have been published in the journal of *Nano Letters*

with the following title:

"Balancing Passive and Active Targeting to Different Tumor Compartments Using Riboflavin-Functionalized Polymeric Nanocarriers"

Reproduced in part with permission from Nano Letters 17, 4665–4674 (2017).

Abstract

Riboflavin transporters and the riboflavin carrier protein are highly upregulated in many tumor cells, tumor stem cells, and tumor neovasculature, which makes them attractive targets for nanomedicines. However, addressing cells in different tumor compartments requires drug carriers with sufficient tumor accumulation, retention, penetration and cellular internalization. Since antibodies are the most efficient targeting systems developed by nature, it may be considered their approximate size to be ideal for a balanced active and passive targeting. Therefore, RF-targeted branched PEG polymers (10 kDa, D_H~6 nm and 40 kDa, D_H~14 nm) were synthesized and tested in nude mice bearing highly angiogenic squamous cell carcinoma and desmoplastic prostate cancer xenografts.

Tumor accumulation of 10 kDa polymers, which are characterized by a short blood half-life and fast inter-compartmental exchange, significantly increased if they are RF-targeted. The 40 kDa polymers accumulated four times more in the cancer lesion than the smaller PEGs, but active targeting did not significantly increase their total amount in the tumor. However, histological analysis, for both tumor models and polymers (10 and 40 kDa), revealed that active targeting strongly improved cellular internalization. Interestingly, while 10 kDa RF-polymers efficiently targeted cancer cells, the 40 kDa RF-PEGs were predominantly found in tumor-associated macrophages. Furthermore, the nanocarriers' accumulation in tumors could not be directly correlated with their cellular uptake - in both tumor models small RF-targeted polymers accumulated to a much lower extent than large untargeted PEG, but showed a significantly higher intracellular amount 72 h after administration. [84]

In conclusion, drug carriers within the size range of therapeutic antibodies showed harmonized properties with respect to passive accumulation, tissue penetration and targeting efficiency. Furthermore, besides highlighting the potential of RF-mediated targeting, it was shown that strong tumor accumulation does not directly indicate high cellular uptake and that small variations in carrier sizes can have strong impact on the targeted cell populations. Finally, evidence was given that active targeting for long circulating drug delivery systems that benefit from EPR effects, may not improve accumulation but only cellular internalization.[84]

4.1 Introduction

Cancer therapies increasingly involve the administration of nanomedicines, which passively accumulate in malignant lesions due to the enhanced permeability and retention (EPR) effect. Passive drug accumulation in tumors relies on strongly fenestrated neovasculature and insufficient lymphatic and venous drainage. Nanomedicine delivery based on EPR, however, has limitations. EPR varies strongly not only among different tumor types but also within different subregions of a single tumor.[22,85,86] Furthermore, a dense fibrotic microenvironment can lead to poor diffusion of the nanomedicines and therefore may hinder their deep penetration. Thus, drug carriers such as nanoparticles, micelles or liposomes often accumulate in the tumor perivascular space of tumors and fail to reach the cancer cells.[22,87,88] Active targeting is suggested to improve nanomedicine accumulation, since it may increase the retention of the nanocarriers through specific cellular uptake. This, however, is only possible if sufficient passive accumulation occurs, the size of nanomedicines allows for deep tissue penetration, and the target is accessible. Therefore, it is still an open question how nanomedicine accumulation in tumors can be maximized and how active and passive targeting mechanisms need to be balanced. Furthermore, enhanced nanomedicine accumulation does not automatically indicate higher therapeutic efficiency. Homogeneous drug distribution within the tumor, as well as delivery to all relevant tumor compartments with optimized uptake by cancer cells, cancer stem cells, endothelium, and malignant stroma, will have a significant impact on the therapeutic outcome. [84]

In order to better understand how active and passive tumor accumulation is influenced by the size of a nanocarrier, four-armed polyethyleneglycol (PEG) polymers with a molecular weight of 10 and 40 kDa, that have different pharmacokinetic profiles in terms of plasma residence [89] and volume of distribution, were evaluated in vivo. The small polymer (10 kDa and D_H~6 nm) is renally clearable, with a short blood half-life, and therefore is expected to display low EPR-based accumulation in the cancer lesion. The large PEG (40 kDa and D_H~14 nm) is just above the renal threshold, with significantly longer blood half-life, and thus likely to show a pronounced EPR-based tumor accumulation. Furthermore, with a hydrodynamic size of approximately 14 nm, the 40 kDa polymer is within the size range of IgG antibodies (D_H ~10-12 nm) [90,91]. Antibodies are the most potent targeting systems developed by nature and thus it can be hypothesized that their great performance is based on an evolutionary developed ideal size. There are different types of antibodies, for example IgM antibodies (D_H~28 nm) are larger, have more binding sites and are responsible for early inflammation phases, whereas production of IgG antibodies represents the long time immune memory. IgG antibodies usually circulate in the blood for a long period of time and extravasate predominantly in areas of inflammation or cancer, where inflammatory and angiogenic factors increase vascular permeability.[90,92] Thus, there might be a relation between the IgG size and the change in vascular permeability during inflammatory and neoplastic events. Therefore, it can be hypothesized that IgG may have the ideal size for sufficiently long blood half-life, passive accumulation at inflammatory sites, and deep tissue penetration, and thus display an excellent extravascular targeting. In contrast, the larger IgM antibodies are responsible for binding predominantly to antigens in the blood [92] and thus their size may already be too large for efficient targeting at areas far outside the vessels. This would mean that for actively targeted drug delivery the size of the majority of commonly used nanomedicines in vivo, such as liposomes, micelles and nanoparticles, is by far too big. [84]

Riboflavin (RF) was selected as a targeting ligand conjugated to the polymers, since its metabolism is shown to be highly up-regulated in cancer stem cells and cells of the cancer microenvironment which would contribute to a homogeneous drug distribution within the tumor as well as delivery to all relevant tumor compartments.[67,68,71,72,93]

Thus, by using different-sized polymers and a target overexpressed in multiple tumor compartments, the following questions were addressed in this study:

a) Does active targeting with RF improve the accumulation of the probes in the tumor?

b) Does the use of differently sized probes influence the preferentially targeted tumor compartment?

c) What is the impact of RF-targeting on the internalization of the probes by different cell types in the tumor?

In order to elucidate these questions, the pharmacokinetics and tumor accumulation of RF-targeted polymers and their non-specific counterparts were evaluated in vivo by using combined CT and fluorescence molecular tomography (CT-FMT) [5,94] in mice bearing A431 (squamous cell carcinoma) and PC3 (prostate cancer) xenografts. Furthermore, histological analysis of tumor sections were performed to evaluate the polymers' distribution within the cancer lesion and their cellular uptake.

4.2 Results and Discussion

PEG modification

A drug delivery system was designed from four-arm PEG tagged with the fluorescent dye Cyanine5.5 (Cy5.5) as a model drug and as a contrast agent for fluorescence molecular tomography. A riboflavin derivative (carboxymethylriboflavin), was further conjugated to the polymer as a targeting moiety. The synthesis of carboxymethylriboflavin is presented in Figure 4.1 and the polymeric systems are illustrated in Figure 4.2 [84].

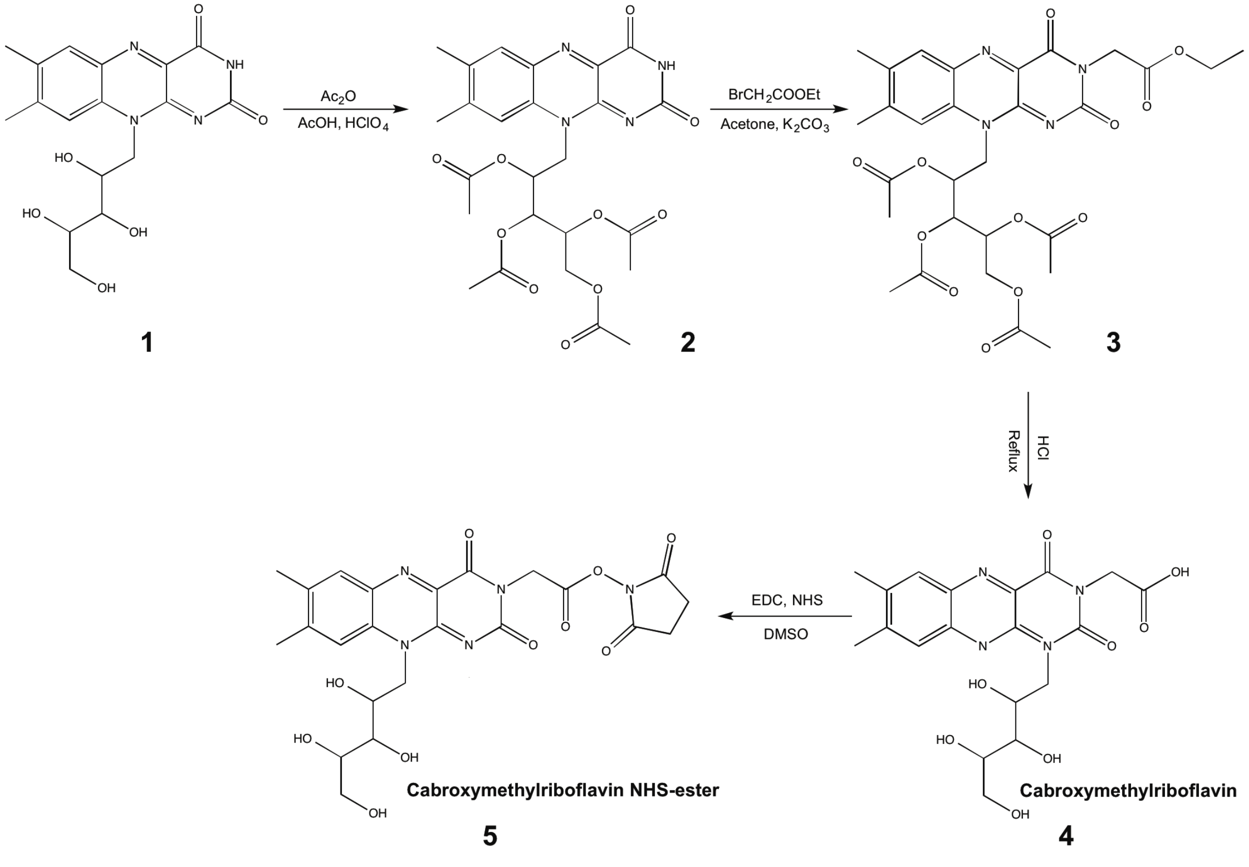

Figure 0.1 Synthesis route of carboxymethylriboflavin NHS-ester. The image is adapted from Ref. 84.

The four-arm PEG is amine functionalized and was reacted with the NHS-ester forms of the Cyanine 5.5 and carboxymethylriboflavin to form stable amide bonds. Single-labeled polymers (tagged on one arm with Cy5.5) served as a control sample. Double-labeled polymers (conjugated with Cy5.5 on one arm, and with carboxymethylriboflavin on the residual three arms) served as a targeted probe. (Figure 4.2 [84])

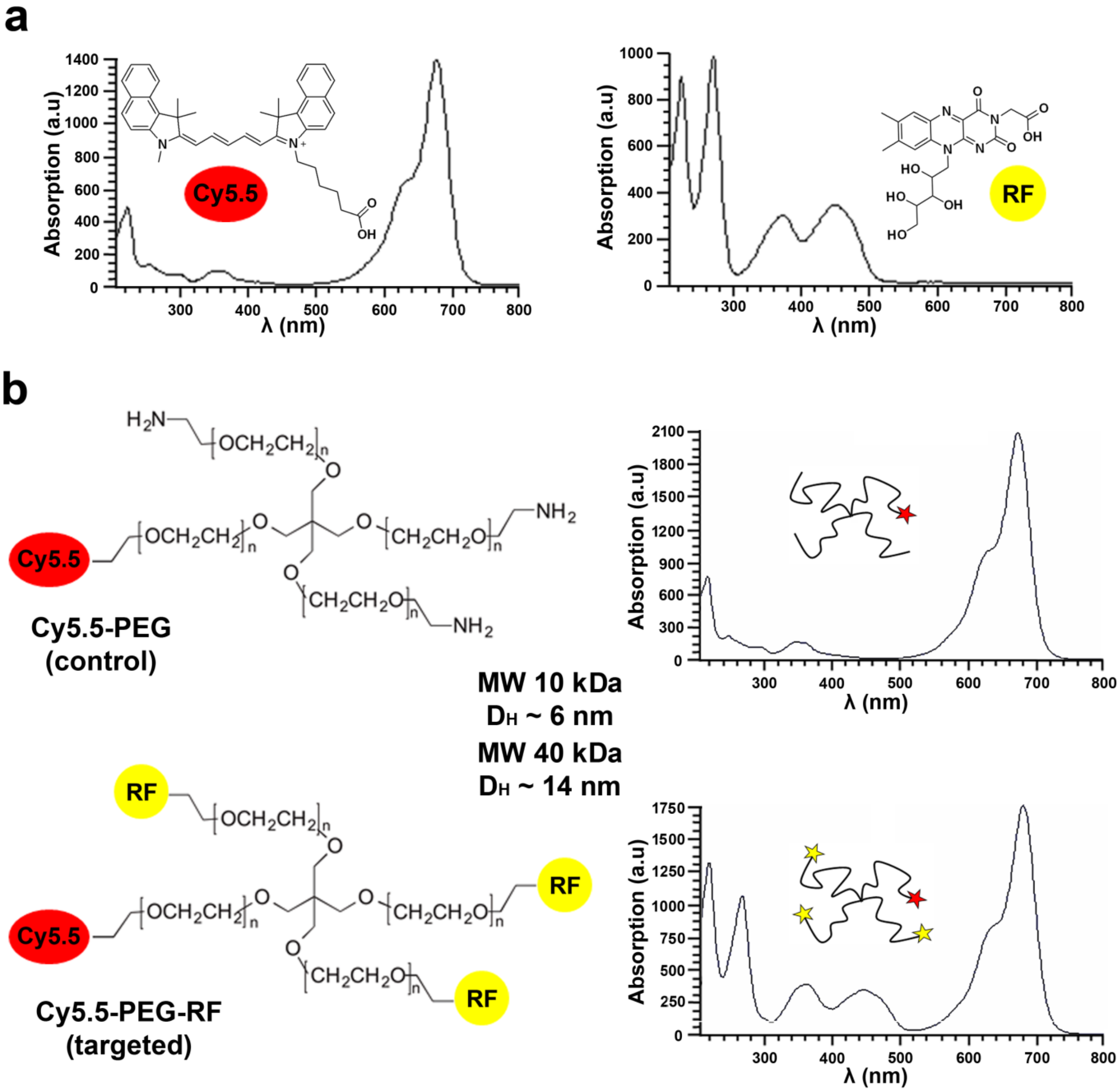

Figure 0.2 Absorption spectra of riboflanin, Cy5.5 and labeled polymers. a: Absorption spectra of carboxymethylriboflavin and the near infrared dye Cyanine 5.5, b: Four-arm PEGs tagged

only with Cy5.5 (control), with Cy5.5 and riboflavin (targeted), and their corresponding absorption spectra. The image is adapted from Ref. 84.

All PEG conjugates were purified on reversed-phase HPLC and the chemical modification was monitored with UV/VIS detector. The polymers, functionalized with both RF and Cy5.5, displayed an absorption spectrum that is characteristic of both conjugated molecules (strong absorption peaks of RF at 260 and 370 nm in the UV range and a maximum at 450 nm in the visible range, along with a strong absorption peak of the cyanine dye at 673 nm). The control polymer displayed only the absorption spectrum of the fluorescent dye. The purity and the hydrodynamic radii of the polymers were measured with Fluorescence Correlation Spectroscopy (FCS). The 10 kDa functionalized PEG displayed D_H~6 nm, and the D_H of the 40 kDa PEG was measured to be about 14 nm. [84]

In vitro studies

First, the targeting efficiency of the 10 kDa RF-polymers was evaluated on the breast cancer cell lines MCF7 and MDA, since riboflavin has been shown to be related to the progression of breast carcinoma.[62,63] The polymer internalization was quantified by fluorescence microscopy at excitation wavelength of 680 nm and showed up to four times higher cellular uptake for the targeted than non-targeted nanocarriers (Figure 4.3). Blocking RFTs or RCP by the addition of 20-fold excess of RF-PEG, that was not labeled with a NIR dye, reduced the cellular uptake of the targeted polymers by 30-50% for both cell lines strongly indicating a receptor-mediated internalization of the targeted polymers.

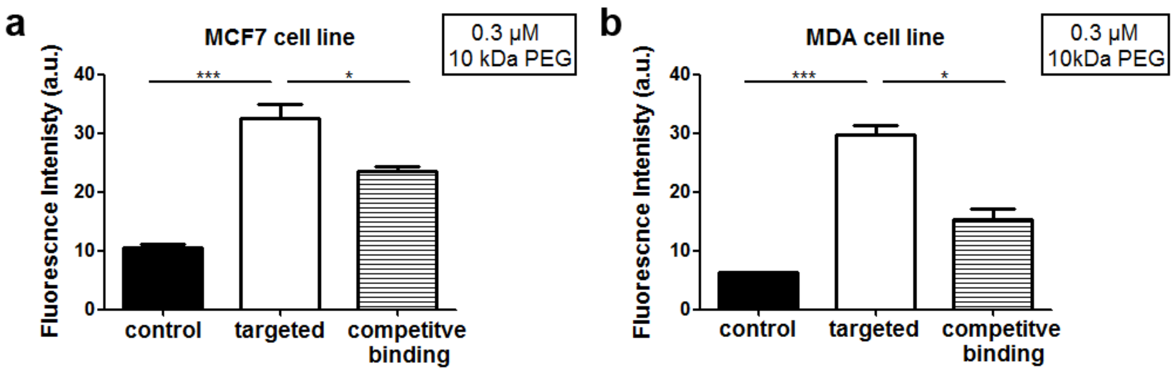

Figure 0.3 Fluorescence microscopy quantification of cellular uptake of 0.3 μM 10 kDa PEGs for a: MCF7 cells and b: MDA cells.

In addition, the cellular uptake of the 10 kDa PEG conjugates was evaluated on the squamous cell carcinoma cell line A431. Different polymer concentrations were tested, and the results showed that RF-targeting was also efficient for this cell line, as presented in Figure 4.4. However, the fluorescence intensity quantifications showed that the specificity of RF-targeted PEGs becomes less prominent with higher polymer concentrations given to the cells most likely due to increased non-specific cellular internalization.

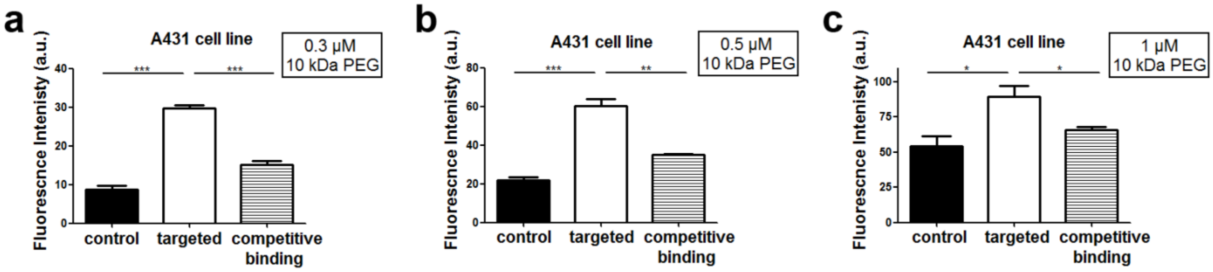

Figure 0.4 Fluorescence microscopy quantification of A431 cellular uptake of 10 kDa PEGs with different concentrations: a: 0.3 μM PEG, b: 0.5 μM PEG [84], c: 1 μM PEG. Image "b" is adapted from Ref. 84.

The cellular uptake of the 0.5 μM 10 and 40 kDa polymers was tested on A431 cell line and the prostate cancer cell line PC3 (Figure 4.5). Targeting efficiency was prominent for the small and large RF-PEGs in both cell lines. Noticeably, the uptake ratios of targeted and non-targeted 10 and 40 kDa PEGs were similar, however, the larger polymers were generally internalized by the cells to a lower extent. This may be due to slower cellular internalization, the nature of the receptor, or a lower accessibility of the targeting moiety (RF may be more entangled within a longer polymer chain and thus less accessible for the transmembrane receptors).

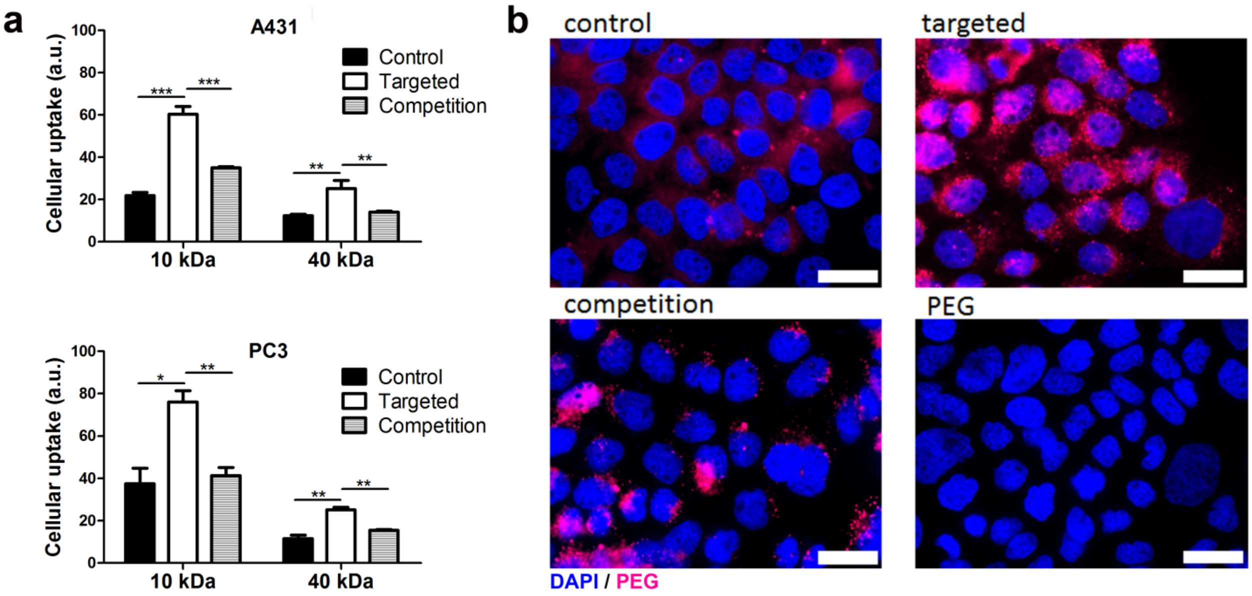

Figure 0.5 Quantification and microscopy images of the cellular uptake of 10 and 40 kDa polymers. a: Quantification of the cellular uptake of 0.3 μM 10 kDa and 40 kDa PEGs based on fluorescence intensity measurements clearly shows the higher uptake of targeted versus non targeted polymers in both cell lines and the significant reduction of cellular internalization after competitive receptor blockade. b: Fluorescence microscopy images of A431 cells after incubation with 10 kDa RF-PEGs (red) are in line with the quantification and show RF-PEGs in a perinuclear location which is in line with a lysosomal storage. Cell nuclei are counterstained with DAPI (blue). Scale bar: 50 μm.[84] The image is adapted from Ref. 84.

Pharmacokinetics and biodistribution

The polymeric conjugates were administered intravenously to CD1 nude mice bearing A431 and PC3 xenografts. In order to assess the polymers' biodistribution in vivo, the mice were imaged longitudinally using CT and 3D FMT. For the mice injected with 10 kDa PEG, scans were performed 15 min, 3 h, 6 h, 24 h after PEG i.v. administration. Mice which received 40 kDa, were additionally scanned at 48 and 72 h. Furthermore, after the last scan (24 h for 10 kDa PEG and 72 h for 40 kDa PEG) the organs of the animals were harvested, and the accumulation of the polymers was validated ex vivo with 2D fluorescence reflectance imaging (FRI). The design of the study is schematically represented in Figure 4.6.

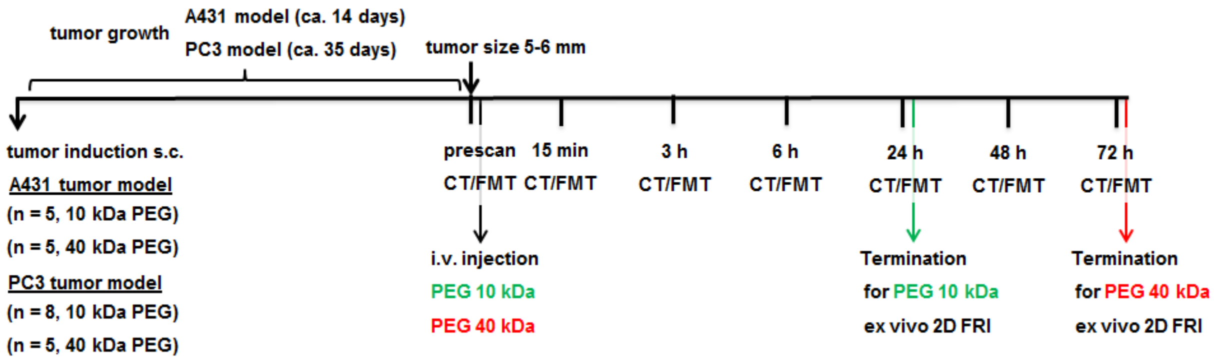

Figure 0.6 Schematic representation of the in vivo experiments.

To determine the blood half-life of the different PEGs, blood samples were collected from each animal at different time points and evaluated with FRI.

The glomerular permeability threshold for PEG polymers is reported to be approximately 30 kDa. [89] Therefore, the 40 kDa PEG remained in the blood circulation for significantly longer time compared with its 10 kDa counterpart. The decreasing fluorescence intensity of the polymers in blood over time, as shown by 2D FRI (Figure 4.7a), was fitted as an exponential decay curve indicating a blood half-life of approximately 1 h for the 10 kDa and 13 h for the 40 kDa PEG (Figure 4.7b). [84]

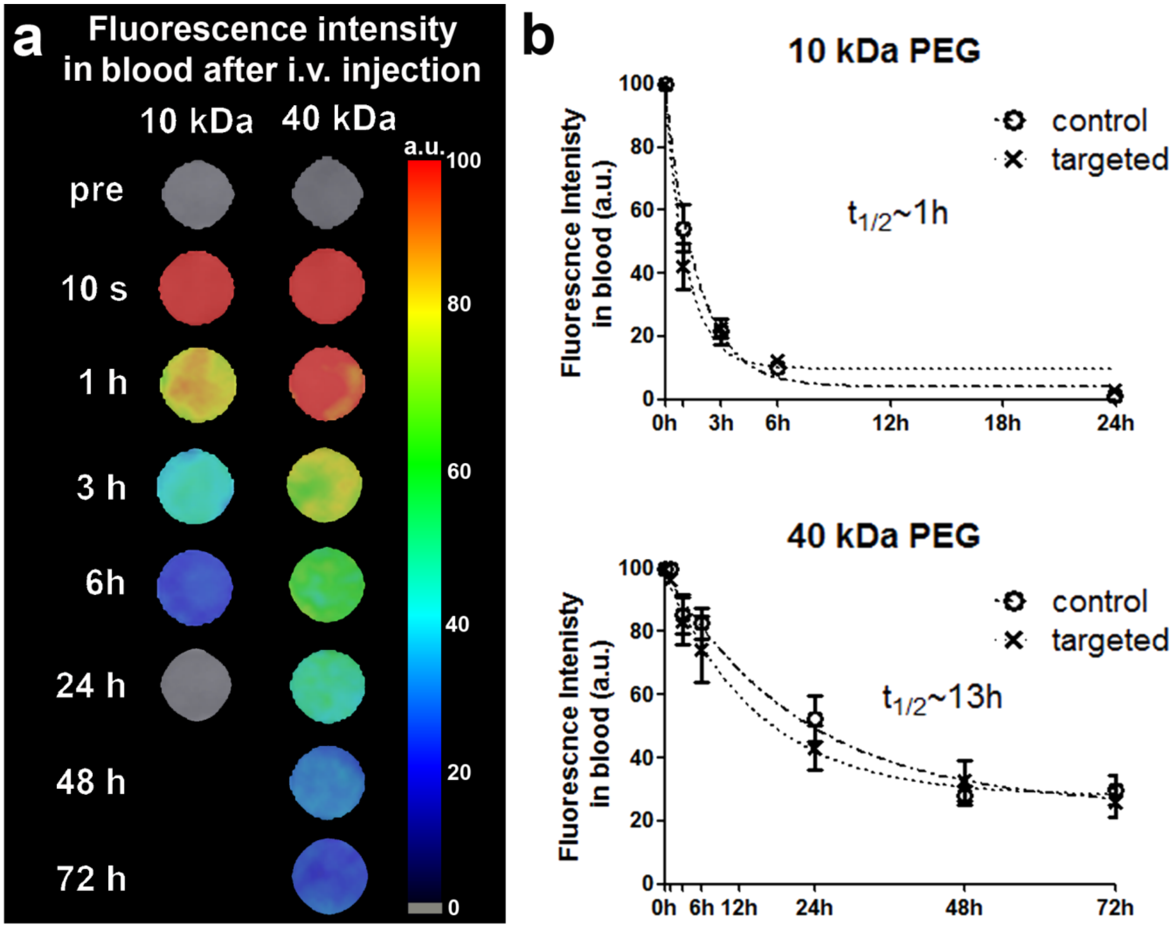

Figure 0.7 Blood half-lives of 10 and 40 kDa PEGs. a: Fluorescence intensity of blood samples measured with 2D FRI after i.v. injection of 10 kDa and 40 kDa Cy5.5-tagged targeted and non-targeted PEG polymers, b: Plot of the blood fluorescence intensity at different time points to assess the blood half-life of the polymers. There is no significant difference in the blood half-lives of targeted and non-targeted polymers. However, as expected, the blood half-lives of the renally cleared 10 kDa polymers are much shorter than of the 40 kDa PEGs.[84] The image is adapted from Ref. 84.

In vivo CT/FMT quantification of the polymers' organ distribution in mice bearing A431 tumors is shown in Figure 4.8a, and ex vivo data acquired by 2D Fluorescence Reflectance Imaging (FRI) are shown in Figure 4.8b. Due to its low molecular weight, the 10 kDa polymer also has a faster vascular penetration and diffusion within the tissue than the larger PEG, which leads to a low retention in the organs.[89] In addition, 72 h after injection there was still a substantial amount of the 40 kDa polymer circulating in the blood (5.5 half-life times), which contributed to the measured amounts in the organs. In line with this, the polymer concentration in liver, kidney and lungs was measured to be two to four times lower for the 10 kDa PEG in comparison with the 40 kDa PEG 72 h after injection. Higher fluorescence signal in the liver was measured for the 10 kDa RF-polymers compared to the 10 kDa control group (7.2 ± 0.4 %ID/cm^3 vs. 4.4 ± 0.5 %ID/cm^3, $p<0.01$), which may be explained by enhanced a receptor-mediated macrophage uptake. This difference was not prominent for the large PEG, most likely due to the much higher unspecific liver uptake of approximately 14 ± 2 %ID/cm^3. Nevertheless, it is important to note that the tumor-to-liver ratio was significantly ($p<0.001$) better for the 40 kDa PEG (0.33 ± 0.05) in comparison with the 10 kDa probe (0.15 ± 0.02). Accumulation in the heart and muscle was low for both probes, but higher for the large (0.6 ± 0.1 %ID/cm^3) than the small PEG (<0.1 %ID/cm^3), which can be explained by the fact that the large polymer was still not completely cleared from the blood 72 h post injection. [84]

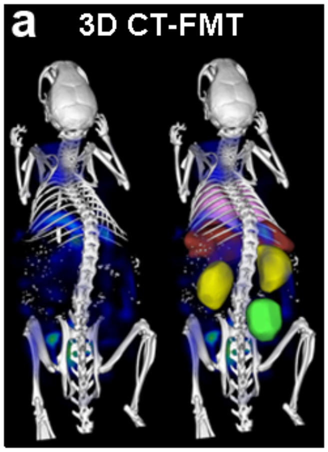

	10 kDa PEG (%ID/cm^3)		40 kDa PEG (%ID/cm^3)	
	control	targeted	control	targeted
tumor	0.6 ± 0.1	1.3 ± 0.2	5.2 ± 1.1	5.0 ± 1.1
liver	4.4 ± 0.5	7.2 ± 0.4	13.1 ± 1.1	14.0 ± 1.5
kidneys	2.0 ± 0.3	2.3 ± 0.4	8.2 ± 1.4	8.9 ± 1.0
lungs	0.5 ± 0.1	0.8 ± 0.2	4.2 ± 1.1	3.4 ± 0.3
heart	< 0.1	< 0.1	0.6 ± 0.2	0.7 ± 0.1
muscle	n.d.	n.d.	0.5 ± 0.1	0.6 ± 0.1

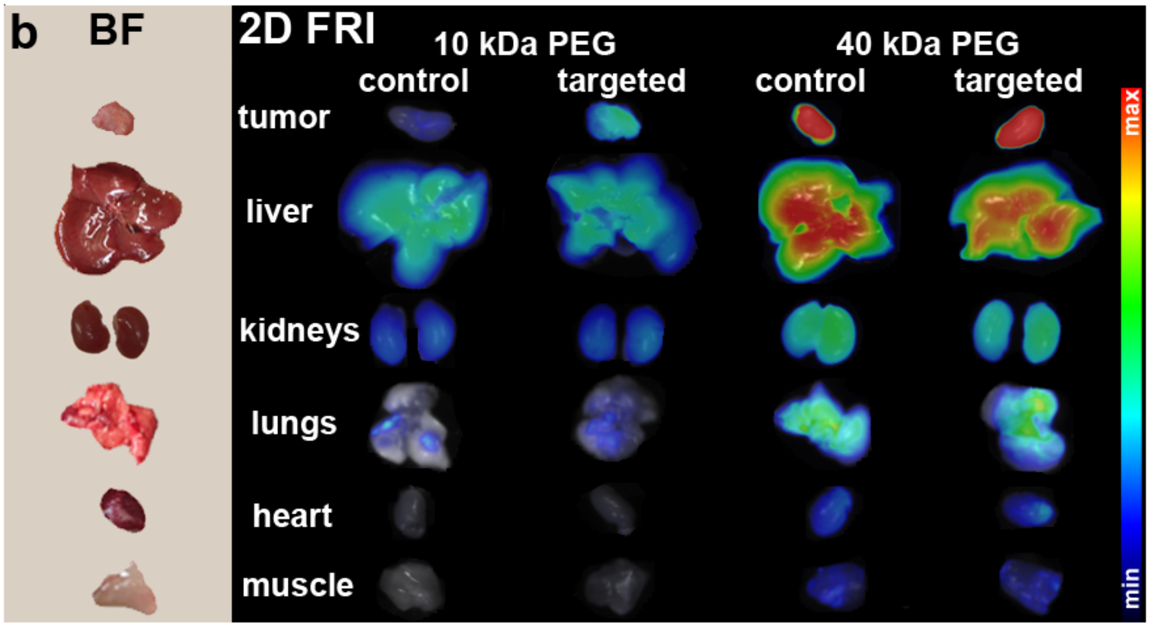

Figure 0.8 Biodistribution of fluorescently labeled 10 kDa PEG 24h post i.v. injection and 40 kDa PEGs 72 h post i.v. injection in mice bearing A431 tumors quantified by 3D CT-FMT. a: An example of a fused CT-FMT image of a mouse with organ segmentation is shown on the left. The results of the quantification of amounts in the organs is presented as percentage of the injected dose per cm^3 (right). Despite higher organ amounts of the 40 kDa than the 10 kDa probe, tumor to liver ratios are higher for the larger PEGs. In addition, it needs to be considered that the data was acquired when still significant amounts of the 40 kDa polymer were still in the blood circulation. b: ex vivo bright-field (BF) organ images (left) and their corresponding 2D FR images indicating the accumulation of the fluorescently labeled PEGs (right).[84] The image is adapted from Ref. 84.

Tumor accumulation

Longitudinal CT/FMT imaging was performed to evaluate the specificity of the RF-polymers in vivo. An enhanced tumor accumulation of the RF-targeted PEGs compared to the control was measured only for the small polymer (10 kDa) as shown in Figure 4.9. [84]

CT/FMT measurements performed during the initial distribution phase of the 10 kDa PEG, at 15 min after i.v. administration, revealed no significant difference between the amount of control and targeted polymer in the tumors. At later time points a significantly increased tumor accumulation of RF-PEGs compared to the non-binding controls was only observed for the small 10 kDa probe in both tumor xenografts (Figure 4.9a). However, this does not necessarily mean that there was no early binding of the RF-PEGs. Small polymers show a fast extravasation and tissue penetration, which leads to a rapid and strong enhancement of the PEG concentration in the extravascular space shortly after i.v. injection, masking the fraction of target-bound polymers. Subsequently, small polymers redistribute into circulation and as the amount of the carrier in the blood rapidly decreases, the retention of active-targeted probes in the tumor becomes more pronounced. This explains the fact that 3 h after administration, when 80% of the injected polymers are cleared from the blood, the difference between active and passive targeting started to become prominent. Significant differences were observed 6 h and then 24 h post injection, when almost all unbound polymers were cleared from the blood circulation. The amount of the 10 kDa polymers accumulated in the tumor lesion, quantified in vivo 24 h after PEG administration, was up to twice as high for the targeted as for the control probe in A431 (1.3 ± 0.2 %ID/cm^3 vs 0.6 ± 0.1 %ID/cm^3, $p<0.05$) and 30% higher in PC3 tumors (0.6 ± 0.1 %ID/cm^3 vs. 0.4 ± 0.1 %ID/cm^3, $p<0.05$). [84]

A significantly different time profile of tumor accumulation was observed for the 40 kDa polymers. In contrast to the small polymers, which show large volume of distribution at early time points but undergo rapid elimination, the larger PEGs exhibited continuous organ accumulation over 24 hours. The accumulation of 40 kDa PEGs in tumors was strongly mediated via EPR, and their concentration in the cancer lesion was approximately four times higher than that of the small polymers, 24 h post injection (RF-PEGs: 4.6 ± 0.6 %ID/cm^3 (40kDa) vs 1.3 ± 0.2 %ID/cm^3 (10kDa) in A431 tumors and 2.6 ± 0.4 %ID/cm^3 (40kDa) vs 0.6 ± 0.1 %ID/cm^3 (10kDa) in PC3 tumors). Interestingly, there was no significant difference between the amount of the 40 kDa targeted and control polymer in both tumor models up to 72 h after injection (Figure 4.9b). This may be due to the high polymer amount passively accumulated in the tumor which makes the difference for the actively retained fraction not significant.[84]

These data indicate that active targeting only improves the tumor accumulation for small nanomedicines with short blood half-life, which are characterized by low tissue retention. As the size of the probe increases, such as in the case of the 40 kDa PEGs, EPR becomes prominent and increases nanoparticles accumulation. Since under these circumstances a strong tissue retention is given, the effect of active targeting becomes less pronounced and may not be detectable anymore.[84]

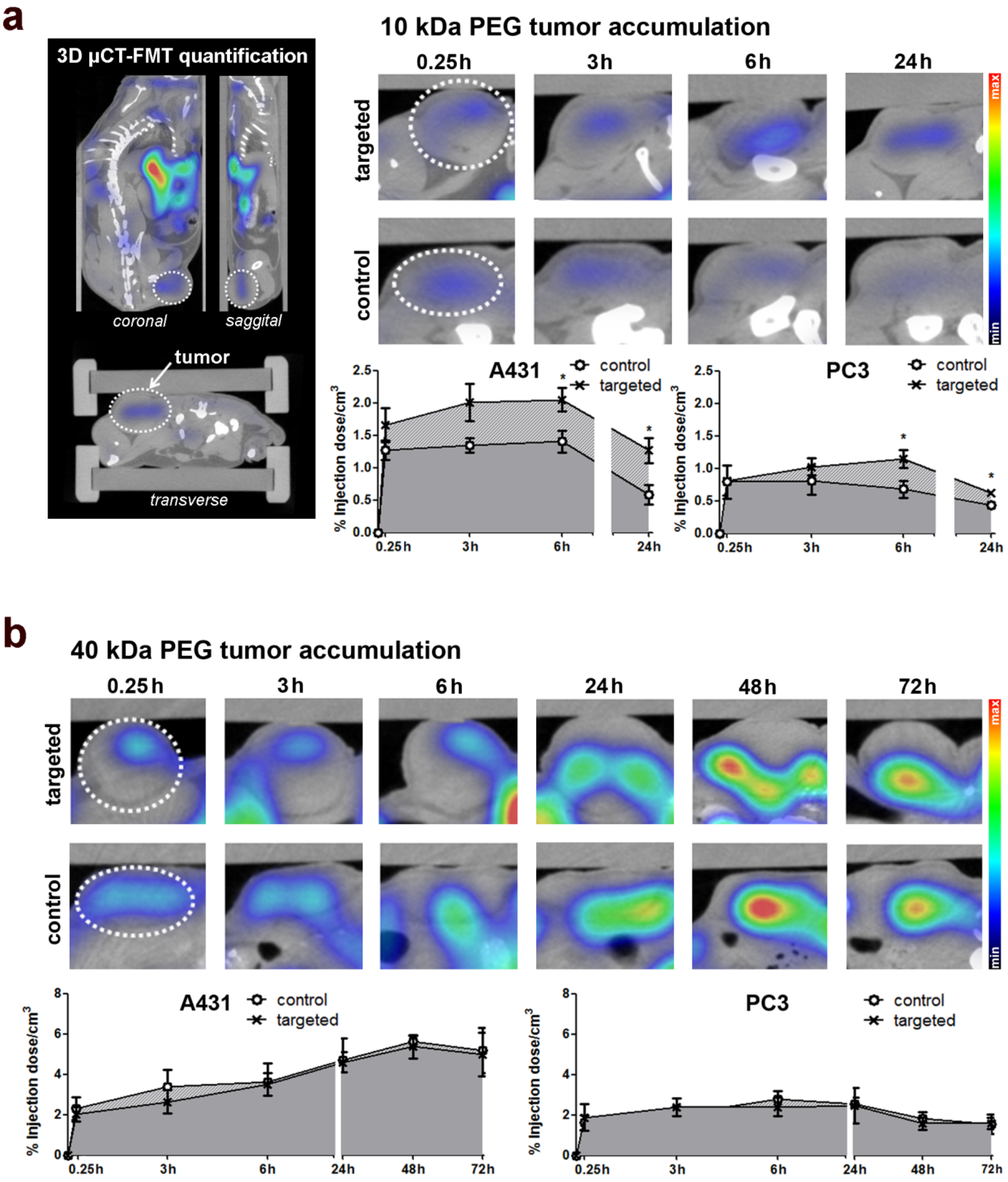

Figure 0.9 Representative CT-FMT images of A431 tumors at different time points after i.v. injection of targeted and control polymers and plots showing the accumulation of 10 kDa PEG (a) and 40 kDa PEG (b) in A431 and PC3 tumor xenografts. Only for the 10 kDa probe active targeting improves the accumulated polymer amount in tumors, which is prominent for both the highly angiogenic A431 and the desmoplastic PC3 tumors. In addition, the differences in the dynamics of 10 kDa and 40 kDa polymer accumulation are clearly demonstrated. Animal

number per group n = 5 for all experiments, except for PC3 tumor model: 10 kDa sample, n = 8.[84] The image is adapted from Ref. 84.

Although the tendency in polymers' longitudinal accumulation was similar for both tumor models, there was a clear difference between the overall amount of PEG in the A431 and the PC3 xenograft. The area below the accumulation-time curves of the control polymers showed that the A431 tumor model was better perfused with the nanocarriers (Figure 4.10a). Since the collagen content in the tumor lesion is one of the major determinants of interstitial transport [95], we analyzed the collagen density and the vascularity of both xenografts by 3D two-photon microscopy in order to explain the difference in the polymers' extravasation. Evaluation of the tumor cryosections indicated a seven-fold higher collagen density and almost three times less functional vessels for the prostate cancer model (Figure 4.10b). Thus, the lower blood supply and denser fibrotic network may be the driving factors that decrease polymer diffusion and distribution within the tumor and explains the lower amount of PEG accumulation in the PC3 xenograft compared to A431.[84]

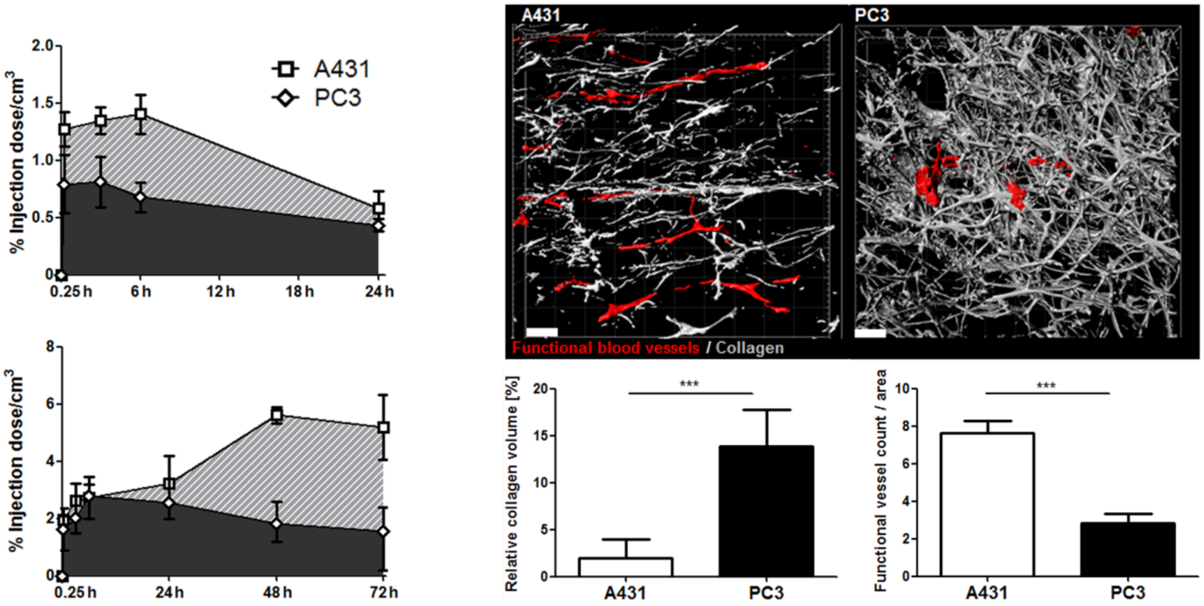

Figure 0.10 Evaluation of vasculature, collagen content and nanocarrier accumulation in A431 and PC3 tumor models. a: Plots are shown that demonstrate that the accumulation of Cy 5.5 labeled 10 and 40 kDa PEGs was substantially lower in PC3 than A431 tumors. b: 3D Two-photon images of PC3 and A431 cryosections (scale bar 50 µm) and the quantification of

collagen content and vessel density indicate the desmoplastic nature and lower vascularization of the PC3 tumors, which may explain the lower accumulation and penetration of the polymers.[84] The image is adapted from Ref. 84.

Polymer distribution, retention and internalization in the tumor

Although passive tumor accumulation via EPR is the dominant advantage of most clinical nanomedicines, it does not always ensure an efficient intracellular drug delivery. Non-targeted nanocarriers are usually designed to release the drugs in the extracellular matrix.[96] Some drugs, however, cannot diffuse efficiently and do not reach the tumor cells. Other non-targeted carriers are designed to release the therapeutic payload within the cell,[97] which relies on non-specific endocytosis and may not always be efficient. Therefore, to achieve high therapeutic efficiency, it is necessary for many drugs and nanomedicines to not only passively accumulate in the tumor but also to ensure cellular internalization. [84]

Histological analysis of tumor cryosections was performed to evaluate the amount of accumulated and internalized polymers. Fluorescence microscopy of unfixed tumor tissue enabled the quantification of the accumulated polymer content in the extravascular, extracellular space and within cells. In order to quantify only the amount of PEG taken up by cells, the tumor sections were fixed and washed extensively to remove the non-internalized polymers. The histological evaluation, represented in Figure 4.11, showed that the amount of accumulated PEG cannot be directly correlated with the amount of PEG internalized by cells.[84]

In line with the in vivo CT-FMT data, the histological analysis revealed no difference in the overall tumor accumulation between the 40 kDa targeted and control polymers in both A431 and PC3 xenografts. However, in terms of cellular uptake, the 40 kDa RF-polymers showed significantly higher internalization vs their non-targeted counterparts: 2.5 ± 0.3 a.u./area vs 1.7 ± 0.1 a.u./area, $p<0.05$ in A431 tumors, and 1.6 ± 0.3 a.u./area vs 0.5 ± 0.1 a.u./area, p<0.01 in PC3 tumors, respectively. The difference between accumulation and internalization is even more pronounced when comparing the 40 kDa control polymers with the small RF-PEGs. Although the 10 kDa RF-PEGs accumulated to much lower extent than the large control PEGs, their cellular uptake was measured to be nearly three times higher (3.8 ± 0.9 a.u./area vs 1.6 ± 0.1 a.u./area p<0.05 in A431 tumors and 1.4 ± 0.2 a.u./area vs 0.5 ± 0.1 a.u./area, p<0.01 in PC3 tumors). These data suggest that the control polymers accumulated predominantly in the extracellular stroma with low degree of non-specific cellular uptake, while the RF-polymers were retained in the tissue due to cell internalization. [84]

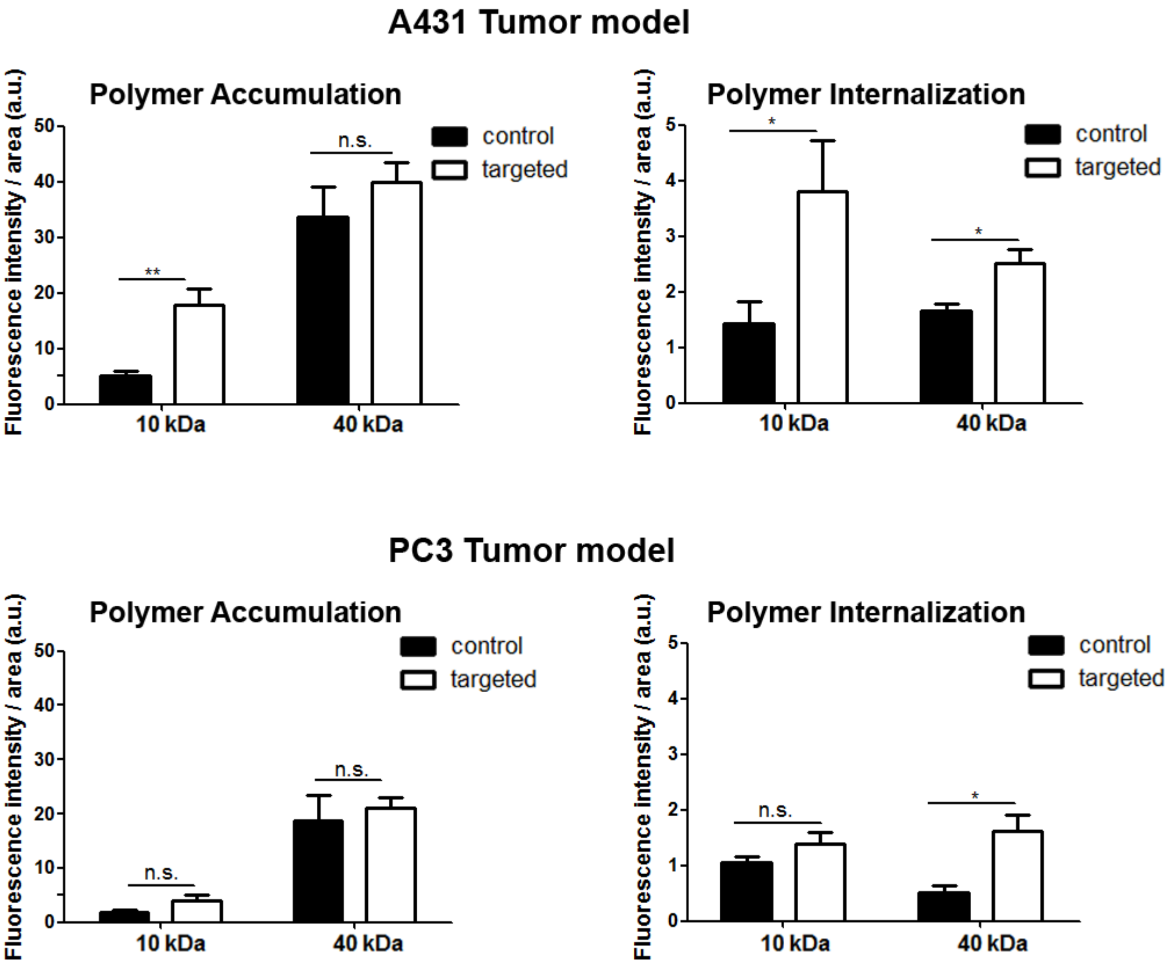

Figure 0.11 Histological quantification of polymers' total tumor accumulation and internalization based on fluorescence intensity measurements of tumor cryosections of A431

(a) and PC3 tumors (b). Histological analyses were performed 24 h after i.v. injection of 10 kDa PEG and 72 h after i.v. injection of 40 kDa PEG. In both tumor models there was a higher passive accumulation of 40 kDa than 10 kDa polymers. Active targeting predominantly improved the accumulation of the small polymers but hardly had any effect on the accumulation of the 40 kDa polymers. However, for both polymers and in both tumor models cellular internalization was strongly improved by active targeting. Please note that, in particular in the highly angiogenic A431 tumor model, tumor accumulation did not match with cellular internalization. [84] The image is adapted from Ref. 84.

Furthermore, immunohistochemical stainings were performed to identify some of the cell types by which the polymers were taken up. Antibodies were used to mark different cells: anti-CD68 for all macrophages, anti-CD163 for M2-type macrophages, anti-Ki67 for proliferating cells, anti-CD31 for endothelial cells of the vessels. The antibodies' co-localization with the polymers' signal is shown in Figures 4.12-4.14. The histological analysis showed that the presence of the targeting ligand and the size of the nanocarrier accounts for a preferential cellular uptake. As illustrated in Figure 4.12, non-targeted polymers were only taken up in low amounts and predominantly found in macrophages while the cellular internalization of the RF-conjugates was much stronger and observed in different tumor compartments: macrophages, tumor cells and proliferating cells. However, as observed in confocal images, presented in Figure 4.13, the uptake of the RF-PEG by endothelial cells was very low (Figure 4.13c), which is in contrast to previous findings about riboflavin-labeled USPIO with ~100 nm size [71,72]. Either endothelial cells less preferentially internalize PEG than USPIO or the lower endothelial uptake is only relative and explained by the fact that riboflavin-labeled USPIO with its considerably short blood half-life did not penetrate deeply into the tissue and thus, showed markedly less uptake by macrophages and hardly any uptake by tumor cells [72]. [84]

Even in the size range between 6 and 14 nm, the size of the nanocarriers strongly influenced their preferential cellular uptake: While the 10 kDa targeted PEGs were evenly distributed among macrophages, cancer cells and proliferating cells in general, the 40 kDa targeted

PEGs were internalized more by macrophages and to a lower extent by cancer cells. This may be due to the high concentration and long persistence of the 40 kDa PEG in the extravascular, extracellular space and its slower penetration into the tissue and thus, stronger exposure to interstitial stroma than cancer cells. However, this does not mean that 40 kDa RF-PEG would be less effective drug carriers. First, killing M2-type tumor macrophages will strongly reduce cancer cell invasion and metastasis.[98] Second, tumor-associated macrophages have been described to act as a slow-release reservoir of nanotherapeutics and may transfer them to neighboring tumor cells.[99] Third, after 72 h there was still significant amount of free 40 kDa RF-PEG in the the interstitial space of the tumor tissue (Figure 4.11a) that over time may penetrate and bind to RFT or RCP on the cancer cells.[84]

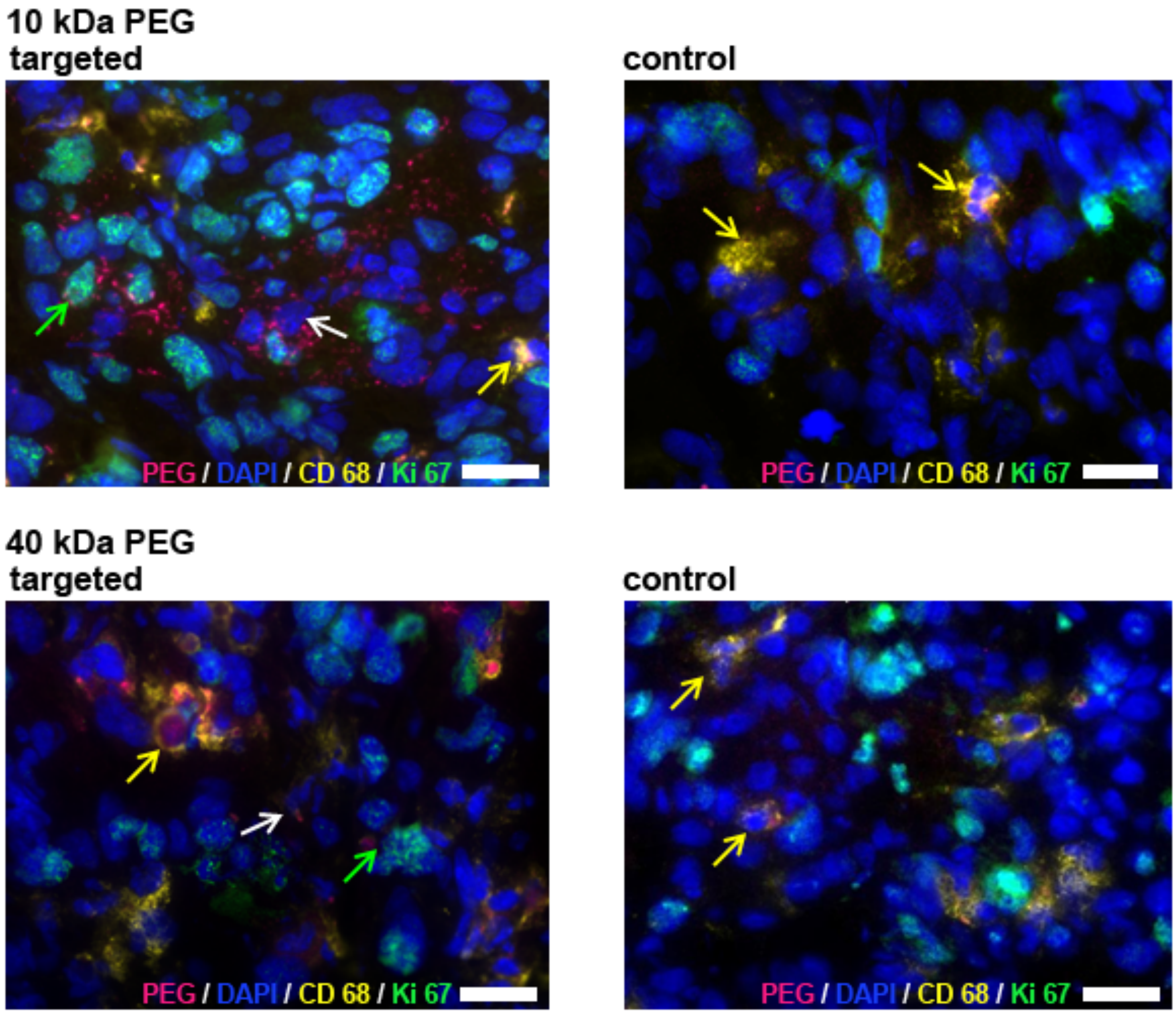

Figure 0.12: Fluorescence images illustrating the cellular uptake of the 10 kDa and 40 kDa polymers in A431 tumors. PEG is shown in red, macrophages (CD68) in yellow, proliferating cells (Ki67) in green and cell nuclei (DAPI) in blue. There was only a low uptake of non-targeted 10 kDa and 40 kDa polymers, predominantly by tumor macrophages. Uptake of the targeted polymers was much more pronounced. However, while the targeted 10 kDa polymers were predominantly located in (proliferating) tumor cells, the 40 kDa polymers are also strongly internalized by macrophages. Arrows show polymer accumulation in different cell types (white arrows for tumor cell, yellow arrows for macrophages, green arrows for proliferating cells). Scale bar: 20 µm.[84] The image is adapted from Ref. 84.

Representative images of the cellular uptake were obtained also with confocal fluorescence microscopy for the 10 kDa RF-PEG in A431 cryosection.

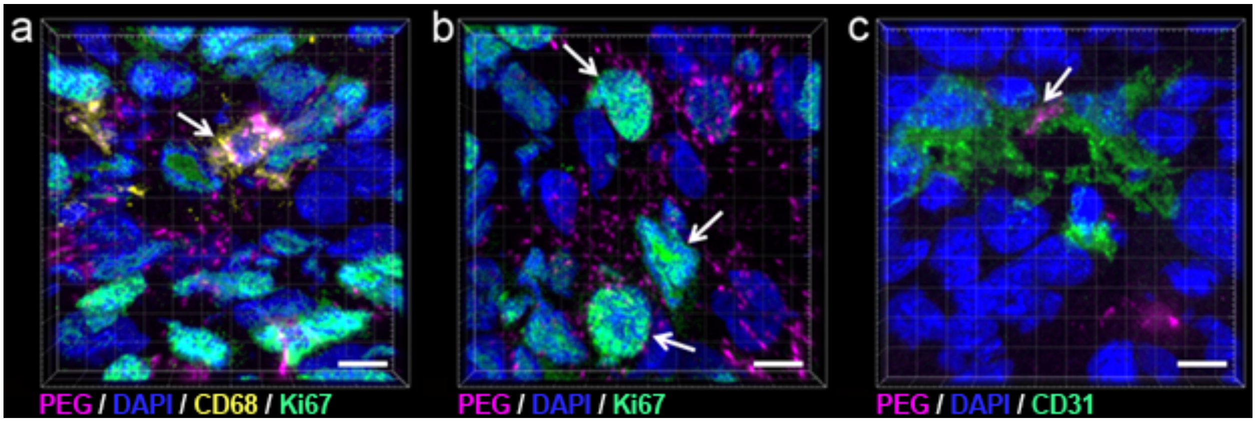

Figure 0.13 Confocal fluorescence images of 10 kDa RF-PEG in A431 tumor model illustrating the cellular uptake by: a: macrophages (CD68) shown in yellow (cell nuclei (DAPI) in blue, proliferating cells (Ki67) in green, PEG in red); b: proliferating cells (Ki67) shown in green (cell nuclei (DAPI) in blue, PEG in red); c: blood vessel endothelial cells (CD31) shown in green (cell nuclei (DAPI) in blue, PEG in red). Scale bar 8 µm.

The macrophage uptake of the RF-PEGs was associated mostly to M2-type macrophages, as presented in Figure 4.14. The cryosections were first stained with anti-CD68 antibody to determine all macrophages. Afterwards, anti-CD163 antibody was used to mark the M2-type macrophages. Merging the signals from anti-CD68 and anti-CD163 showed which of all found macrophages were M2-type.

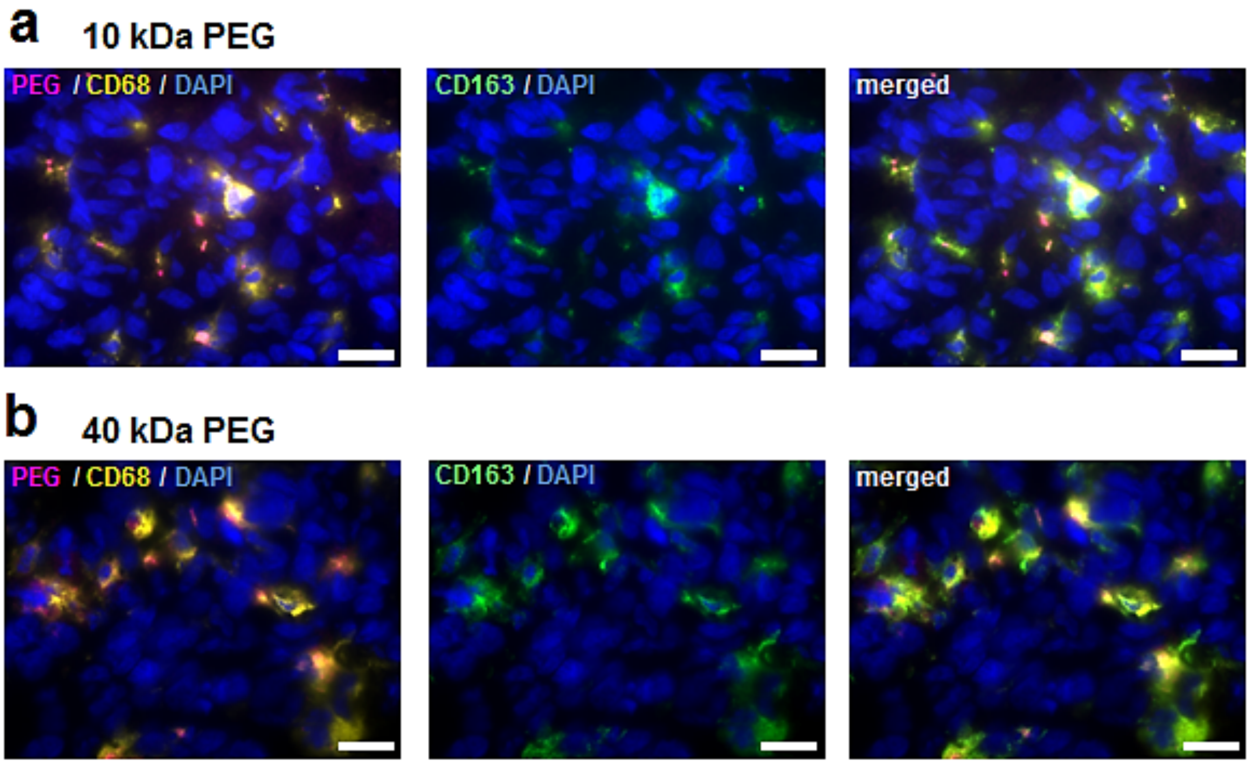

Figure 0.14: Fluorescence images illustrating the cellular uptake of the 10 kDa and 40 kDa RF-polymers in A431 tumors. PEG is shown in red, all macrophages (CD68) in yellow, M2 machropages (CD163) in green and cell nuclei (DAPI) in blue. Scale bar: 20 µm. a: 10 kDa RF-PEG, b: 40 kDa RF-PEG.

4.3 Conclusion

In summary, besides supporting RFTs and RCP as interesting targets for cancer nanomedicines, this study highlighted some important relations between particle size and passive and active targeting. The results showed that active targeting improved the tumor accumulation only for small drug carriers with short blood half-life, which are characterized by low tissue retention. Long-circulating targeted nanomedicines, with a size similar to IgG antibodies, displayed strong EPR –based accumulation and active targeting was beneficial only for their cellular internalization in the tumor lesion. Active targeting with riboflavin strongly improved the cellular uptake of the polymers by cancer cells, macrophages and proliferating cells. In this context, it could be suggested that IgG may have the ideal size to circulate long, selectively extravasate in (inflamed) tissues with increased vascular permeability, passively accumulate in these tissues via EPR, and penetrate deeply and thus find extravascular targets. Thus, for nanomedicines, which are actively targeted and not designed to release their payload in the interstitial space (like most liposomes and micelles), the size range of therapeutic antibodies may be preferable.[84]

4.4 Experimental

Synthesis, characterization and activation of carboxymethylriboflavin

The synthesis of carboxyriboflavin was conducted in three steps, as described by Caelen et al. [100]. The substances obtained in each step of the synthesis were characterized with ^{1}H NMR and mass spectroscopy. NMR spectra were recorded on a Varian AV400 or AV600 spectrometer (^{1}H: 400 MHz) in CD_3OD or $CDCl_3$ and reported relative to the solvents residual signal ^{1}H (CHD_2OD, δ(H) = 3.31 (q); $CHCl_3$, δ(H)=7.26). MS (ESI) was performed on Thermo Fisher LTQ-Orbitrap XL, positive ion mode, *m/z* (rel. intensity %) or on a Finnigan SSQ 7000 mass spectrometer (EI or CI). [84]

The chemicals were purchased from the following firms and were used without any further purification: riboflavin (Applichem), glacial acetic acid (Carl Roth), acetic anhydride (Sigma Aldrich), perchloric acid (70-72%) (Merck), anhydrous sodium sulfate (AppliChem), anhydrous potassium carbonate (Carl Roth), ethylbromoacetate (Alfa Aesar), N-hydroxysuccinimide (Sigma Aldrich), 1-(3-Dimethylaminopropyl)-3-ethylcarbodiimide (Fluka), acetone (VWR), chloroform (Carl Roth), dichloromethane (Sigma Aldrich), DMSO (Acros Organics) chloroform-d ($CDCl_3$) (Carl Roth), methanol-d4 (CD_3OD) (Sigma Aldrich). [84]

Synthesis of 2’,3’,4’,5’-tetra-O-acetyl riboflavin (**2**): Riboflavin (1000 mg, 2.7 mmol, **1**) was dissolved in a 1:1 mixture of 40 ml glacial acetic acid and acetic anhydride. After adding 0.2 ml perchloric acid (70-72%), the mixture was stirred for 1 h at 40°C. After cooling down, 40 ml of cold water was added to the mixture and the product was extracted with chloroform. The chloroform phase was dried with anhydrous sodium sulfate, filtered, and the solvent was removed under reduced pressure to obtain 2’,3’,4’,5’-tetra-O-acetylriboflavin (1248 mg, 2.29 mmol, 85 % yield) as light yellow powder.[84]

Mass (m/z) found: 545.19 ([M+H]$^+$), calculated for $C_{25}H_{28}N_4O_{10}$: 544.51

2',3',4',5'-tetra-O-acetylriboflavin: ^{1}H NMR (CD_3OD), δ (ppm): 2.04 (s, 3H, CH_3), 2.17 (s, 3H, CH_3), 2.20 (s, 3H, CH_3), δ 2.21 (s, 3H, CH_3), 2.49 (s, 3H, 2CH_3), 2.62 (s, 3H, 2CH_3), 4.35 (ddd, *J*=18.5, 12.3, 4.6 Hz, 3H, CH_2, CH), 4.59 (s, 1H, CH), 5.44 (td, *J*=3.2, 6.1, 6.1, 1H, CH), 5.44 (td, *J*=3.2, 6.1, 6.1, 1H, CH), 5.55 (m, 1H, CH), 5.69 (dd, *J*=12.5, 4.6 Hz, 1H, CH), 7,84 (s 1H, CH), 7.95 (s 1H, CH).[84]

Synthesis of 2',3',4',5'-tetra-O-acetyl-N(3)-ethoxycarbonylmethyl riboflavin (**3**):

2',3',4',5'-tetra-O-acetylriboflavin (1240 mg, 2.28 mmol, 1 equiv., **2**), potassium carbonate (1573 mg, 11.40 mmol, 5 equiv.) were taken in anhydrous acetone, and added . ethyl bromoacetate (1.3 ml, 11.40 mmol, 5 equiv.). The reaction mixture was stirred over night at room temperature. After that the solvent was removed under reduced pressure and the residue was dissolved in dichloromethane, and washed twice with 1 N acetic acid, followed by water. The collective organic phase was dried with anhydrous sodium sulfate, filtered, and the solvent was removed under reduced pressure to obtain compound **3** (522 mg, 0.81 mmol, 35 % yield) as yellow powder. [84]

Mass (m/z) found: 631.22 ([M+H]$^+$), calculated for $C_{29}H_{34}N_4O_{12}$: 662.60

^{1}H NMR ($CDCl_3$), δ (ppm): 1.28 (t, *J*=7.1, 3H, CH_3), 1.77 (s, 3H, CH_3), 2.08 (s, 3H, CH_3), δ 2.21 (s, 3H, CH_3), 2.30 (s, 3H, CH_3), 2.45 (s, 3H, 2CH_3), 2.57 (s, 3H, 2CH_3), 4.31 (m, 5H, CH_2), 4.82 (dd, *J*=2.1 Hz, 2H, CH_2), 4.42 (dd, *J*=5.0, 2.6 Hz, 2H, CH_2), 5.64 (s, 1H, CH), 7.57 (s 1H, CH), 8.05 (s 1H, CH).

Synthesis of N(3)-carboxymethyl riboflavin (**3**): -2',3',4',5'-tetra-O-acetyl N3-ethyloxycarbonylmethyl riboflavin (500 mg, 0.77 mmol, **2**) was refluxed in 2 M HCl for 2 h.

The solvent was dried under reduced pressure to obtain carboxymethylriboflavin (267 mg, 0.62 mmol, 80% yield) as yellow powder.[84]

Mass (m/z) found: 435.15 ($[M+H]^+$), calculated for $C_{19}H_{22}N_4O_8$: 434.40

^{1}H NMR (CD_3OD), δ (ppm): 2.49 (s, 3H, CH_3), δ 2.60 (s, 3H, CH_3), 3.67 (m, 1H, CH), 3.83 (m, 3H, CH, CH_2), 4.45 (d, *J*=9.0 Hz, 1H, CH), 4.76 (d, *J*=7.0 Hz, 2H, CH_2), 5.04 (dt, *J*=22.7, 11.7 Hz, 2H, CH_2), 8.05 (s 1H, CH), 8.18 (s 1H, CH).

Synthesis of **5** (NHS-ester of N(3)-carboxymethylriboflavin):

Equimolar amount of N3-carboxymethylriboflavin, N-hydroxysuccinimide (NHS) and 1-(3-Dimethylamino-propyl)-3-ethylcarbodiimide (EDC) were taken in anhydrous DMSO and stirred for 1 h. The obtained product was directly used for next step without any purification.[84]

Labeling and characterization of four-arm PEG

Four-arm PEG-amines (with a pentaerythritol core) with molecular weights of 10 kDa and 40 kDa were purchased at JenKemTechnology USA. The polymers were either single-labeled (one arm coupled to NIR dye Cy5.5) or double labeled (one arm coupled to Cy5.5, the other three to carboxymethylriboflavin). Calibration curves of Cy5.5 (excitation at 673 nm, emission at 707 nm) and carboxyriboflavin (excitation at 450 nm, emission at 530 nm) were obtained with a spectrometer (Tecan Infinite 200 Pro, Tecan Trading AG, Switzerland) in order to quantify the amount of the labeled polymers and conjugated fluorophores. Assuming that one Cy5.5 molecule was coupled to one polymer chain, the amount of the labeled PEGs could be quantified by emission intensity measurement at 707 nm, corresponding to the calibration curve of the Cy5.5 dye. The amount of conjugated carboxymethylriboflavin to the polymer was quantified by measuring the fluorescence intensity of the double-labeled PEG at 530 nm, corresponding to the calibration curve of carboxymethylriboflavin.[84]

Synthesis of single-labeled PEGs(10 and 40 kDa):

In order to tag only one of the PEG arms with a fluorescent dye, an excess of the polymers (10:1) was mixed with the near infrared dye Cyanine 5.5 (Cy5.5-NHS-ester purchased by Lumiprobe, Germany). [84]

Cy5.5 labeling of 10 kDa PEG: 0.2 ml DMSO solution of Cy 5.5-NHS-ester (0.5 µmol, 1 equiv.) was mixed with 10 kDa PEG-amine (50 mg, ~5 µmol, 10 equiv.) dissolved in 2 ml carbonate-bicarbonate buffer (pH 8.5). The mixture was stirred at room temperature for 15 min after which the labeled polymer (10 kDa Cy5.5-PEG) was purified using a reverse phase HPLC. [84]

Cy5.5 labeling of 40 kDa PEG: 0.8 ml DMSO solution of Cy5.5-NHS-ester (0.5 µmol, 1 equiv.) was mixed with 10 kDa PEG-amine (200 mg, ~5 µmol, 10 equiv.) dissolved in 8 ml carbonate-bicarbonate buffer (pH 8.5). The mixture was stirred at room temperature for 15 min after which the labeled polymer (40 kDa Cy5.5-PEG) was purified using a reverse phase HPLC. [84]

Synthesis of double-labeled PEGs (10 and 40 kDa):

HPLC-purified Cy5.5-PEG (0.2 µmol, 1 equiv.) was dissolved in 500 µl carbonate-bicarbonate buffer (pH 8.5) mixed with 50 µl DMSO solution of carboxymethylriboflavin-NHS ester (6.0 µmol, 30 equiv.) and stirred for 1 h at room temperature. [84]

Diode array HPLC detectors displayed the UV-VIS spectra of each peak in the chromatogram, which showed an absorption spectrum of Cy5.5 for the single-labeled PEGs and a mixed absorption spectrum of Cy5.5 and carboxymethylriboflavin for the double-labeled PEGs.

All labeled polymers were freeze-dried and stored at -20°C.

HPLC conditions

The polymer purification was conducted with Agilent Infinity 1260 HPLC system comprising a Chemstation chromatography software (VersionB-04-03), 1260 Infinity II manual sample injector, 1260 DAD and an Agilent 1260 Quartenary pump. Reversed phase separations were carried out at room temperature using the following conditions:

10 kDa PEG:

150 × 4.6 mm i.d., 5 µm C_8 Zorbax (Agilent) column. The mobile phase was a 30 min 10–90% gradient of water and acetonitrile/water (70/30) with 0.01% trifluoroacetic acid, eluted at a flow rate of 1 ml/min. All solvents used are gradient grade. [84]

40 kDa PEG:

250 × 20 mm i.d., 5 µm C_{18} Multo High 100 RP 18 (CS Chromatogrphie) column. The mobile phase was a 1 h 10–90% gradient of water and acetonitrile/water (70/30) with 0.01% trifluoroacetic acid, eluted at a flow rate of 5 ml/min. All solvents used are gradient grade. [84]

In vitro experiments

The cellular uptake of the polymers was evaluated for A431 cell line (human epidermoid carcinoma cells) and for PC3 (human prostate cancer cells), both obtained from ATCC (Wesel, Germany). A431 cells were cultivated in RPMI and PC3 cells in McCoy medium supplemented with 10% FCS and 1% Pen/Strep, obtained from Gibco, Invitrogen, Germany. All cell lines were cultured at 37°C in a humidified atmosphere of 5% CO_2. [84]

The cells were incubated with different polymer concentrations (0.3, 0.5 and 1 µM) for 1 h at 37°C or at 4°C. Afterwards, the cells were washed trice with PBS (Gibco, Invitrogen, Germany), fixed with 4% PVA solution and the cellular uptake was quantified means fluorescence microscopy. Each experiment was done in triplicate. [84]

In vivo experiments and polymer administration

All animal experiments were approved by the governmental authority for animal care.

Eight-week old CD-1 female nude mice (n=20, Charles River Laboratories, Wilmington, USA) were inoculated with 100 µL of $4x10^6$ A431 cells suspension in RPMI culture medium, subcutaneously into the right flank. The tumors xenografts were monitored for ca 20 days until they reached size of about 8 mm. [84]

Eight-week old CD-1 male mice (n=23, Charles River Laboratories, Wilmington, USA) were inoculated with 100 µL of $3x10^6$ PC3 cells suspension in McCoy culture medium subcutaneously into the right flank. The experiments were started ca 35 days after inoculation when the PC3 tumor xenografts reached the size of ca 6 mm. [84]

A week prior polymer i.v. administration, all mice received chlorophyll-free food in order to reduce autofluorescence. Fluorescent polymers (6 nmol) were dissolved in 100 µL physiological saline and injected into the mice tail vein. 3D CT/FMT imaging was performed under inhalation isoflurane anesthesia (2%) at different time points after injection: 0.5 h, 3 h, 6 h, 24 h, 48 h and 72 h. Mice which received 10 kDa polymers were sacrificed 24 h after probe administration and those 40 kDa were imaged additionally at 48 and 72 h before being sacrificed. [84]

3D CT/FMT

The mice were scanned in a cassette that contains markers for image registration and that fits in both µCT- and in FMT-system. The mice were first scanned with CT, after which they were imaged with FMT. The image data sets were reconstructed, matched and fused with a software (Imalytics Preclinical software [5]). [84]

CT imaging was performed with Micro-CT TomoScope Duo (CT Imaging, Erlangen, Germany). The CT scanner was run with two tubes at 65 kV and 0.5 mA with full rotation and a scan duration of 90s. [84]

FMT (FMT2500; PerkinElmer) was used to perform whole body scan of the mouse at 680 nm excitation wavelength. [84]

Histology and Fluorescence microscopy

After the mice were sacrificed, the organs were collected and embedded in Tissue-Tek (Sakura, Staufen, Germany) and stored at -80 °C. Eight µm-thick tumor cryosections were fixed with 80% Methanol (v/v) aqueous solution for 5 mins and afterwards with cold acetone for 2 mins. Immunohistochemistry stainings were performed with anti-CD68 antibody (AbD Serotec, Puchheim, Germany), anti-CD31 antibody (BD Biosciences, Germany), anti-Ki67 antibody (Abcam, Germany) and anti-CD163 antibody (Dianova, Hamburg, Germany). Secondary antibodies were obtained from Dianova (Hamburg, Germany). DAPI (Sigma Aldrich, Taufkirchen, Germany) was used for nuclei counterstaining and sections were mounted with Mowiol. Fluorescence microscopy was performed with Axio Imager M2 microscope (Carl Zeiss Microimaging GmbH, Göttingen, Germany) and a high-resolution camera (AxioCam MRm Rev.3, Carl Zeiss Microimaging GmbH, Göttingen, Germany). [84]

Fluorescence Confocal microscopy

Eight hundred µm-thick tumor cryosections were analyzed with Leica TCS SP8 X automated inverted confocal microscope (Leica Microsystems). Excitation was performed using white light laser (470-670 nm). Hybrid detectors were used (HyDs) for detection. Microscope objectives: plan-apochromat 100x/1.40 oil-immersion and plan-apochromat 20X/0,75 multi-immersion.[84]

Two Photon microscopy

One hundred μm-thick unfixed tumor cryosections were used for image acquisition. Image stacks, containing 50 images with 1 μm steps along the z-axis, were obtained with 25x water-immersed objective on Olympus FV1000MPE multiphoton microscopy system. Blood vessels pefused with rhodamine-lectin staining and collagen content (second-harmonic generation imaging) were imaged. Two-photon Laser Scanning Microscopy images were analyzed with Imaris Software, Version 7.4 (Bitplane AG, Zurich, Switzerland) and the collagen content of each tumor were quantified using intensity thresholding.[84]

Statistical Analysis

The results were evaluated with GraphPad Prism 5.01 and are shown as average ± standard error of the mean. The statistical analysis were performed using the two-tailed student's t-test and a p-value < 0.05 was considered as statistical significance (*: p<0.05, **: p<0.01, ***: p<0.001), indication with n.s.: not significant.[84]

Chapter 5

5. Summary

The development of nanomaterials and their physicochemical, in vitro, and in vivo evaluation in preclinical settings have a great impact on the improvement of cancer diagnosis and treatment. Nanomaterials can be used as contrast agents and/or drug delivery systems, and their efficiency in cancer therapy may be improved by their conjugation to a targeting ligand, which specifically binds to cellular receptors overexpressed in the tumor lesion. Riboflavin transporters (RFT) and riboflavin carrier protein (RCP) are overexpressed by many tumor cells and cells of the malignant stroma. This is why this thesis involves two studies focused on the preclinical evaluation of riboflavin (vitamin B2) as a tumor targeting ligand for nanomaterials.

In the first study, flavin mononucleotide (a riboflavin derivative) was grafted on the surface of ultrasmall superparamagnetic iron oxide (USPIO) nanoparticles, used as contrast agents for magnetic resonance imaging (MRI). The riboflavin-targeted USPIOs were further stabilized with different small biomolecules that influenced the size and functionality of the magnetic nanoparticles. The nanoparticles' uptake by endothelial and numerous cancer cells was evaluated photometricaly and with MRI. The results showed that the surface modification of the contrast agents had a significant influence on the cellular internalization: riboflavin faciliated a receptor-mediated endocytosis of the magnetic nanoparticles by cancer cells, and the amount of targeting ligand on the particles' surface regulated the degree of cellular uptake.

In the second study, the targeting efficiency of riboflavin-functionalized polymers was evaluated in vivo - in mice bearing prostate and epidermoid tumors - using fluorescent molecular and computed tomography. The polymers had different molecular weights and hydrodynamic sizes (10 kDa, D_H~6 nm and 40 kDa, D_H~14 nm) and, therefore, displayed different pharmacokinetic profiles in terms of plasma residence and volume of distribution. The results led to the hypothesis that targeted drug delivery systems should have the size of diagnostic antibodies (D_H~12 nm) in order to display an ideal balance between EPR-based accumulation, sufficient tumor penetration, active binding, and cellular internalization. Riboflavin targeting with drug carriers exhibiting rapid compartmental exchange and fast tissue clearance significantly improved tumor accumulation and cellular uptake in the cancer lesion. On the other hand, riboflavin targeting with long circulating drug carriers improved only their cellular internalization in the malignant lesion and hardly increased their tumor accumulation. In addition, the results showed that already small differences in probe size could influence drug carrier uptake in targeted cell populations in tumors.

Chapter 6

6. Appendix

6.1 List of abbreviation

AMP	Adenosine monophosphate
ADP	Adenosine diphosphate
ATP	Adenosine triphosphate
cRCP	Chicken riboflavin carrier protein
CD	Cluster of differentiation
CT	Computed tomography
Cy 5.5	Cyanine 5.5
DAPI	4′,6-Diamidin-2-phenylindol
DiR	1,1′ -dioctadecyl-3,3,3′ ,3′ -tetramethylindotricarbocyanine iodide
EPR	Enhanced permeability and retention
FAD	Flavin adenine dinucleotide
FMN	Flavin mononucleotide
FMT	Fluorescence molecular tomography
GMP	Guanosine monophosphate
GFP	Green fluorescent protein
HPLC	High performance liquid chromatography
HPMA	N-(2-hydroxypropyl)methacrylamide
HUVEC	Human umbilical vein endothelial cells
ICG	Indocyanine green
MDR	Multidrug resistance
MR	Magnetic resonance
MRI	Magnetic resonance Imaging
NIR	Near-infrared
OI	Optical Imaging
PEG	Polyethylene glycol
PET	Positron emission tomography
PAI	Photoacoustic Imaging
PMAM	Polyamidoamine
RCP	Riboflavin Carrier protein
RF	Riboflavin
RFT 1	Riboflavin transporter 1
RFT 2	Riboflavin transporter 2
RFT 3	Riboflavin transporter 3
Rh	Hydrodynamic radius
SPECT	Single photon emission computed tomography
SPION	Superparamagnetic iron oxide nanoparticle
USPIO	Ultrasmall superparamagnetic iron oxide
UV	Ultraviolet
VIS	Visible

6.2 List of tables

6.3 List of figures

6.4 References

1. James, M. L. & Gambhir, S. S. A Molecular Imaging Primer: Modalities, Imaging Agents, and Applications. *Physiol. Rev.* **92,** 897–965 (2012).
2. Kunjachan, S., Ehling, J., Storm, G., Kiessling, F. & Lammers, T. Noninvasive Imaging of Nanomedicines and Nanotheranostics: Principles, Progress, and Prospects. *Chem. Rev.* **115,** 10907–10937 (2015).
3. Lusic, H. & Grinstaff, M. W. X-Ray Computed Tomography Contrast Agents. *Chem. Rev.* **113,** (2013).
4. Rajan, S. S. *MRI: A Conceptual Overview*. (Springer Science & Business Media, 1997).
5. Gremse, F. *et al.* Absorption Reconstruction Improves Biodistribution Assessment of Fluorescent Nanoprobes Using Hybrid Fluorescence-mediated Tomography. *Theranostics* **4,** 960–971 (2014).
6. Jeswani, T. & Padhani, A. R. Imaging tumour angiogenesis. *Cancer Imaging* **5,** 131–138 (2005).
7. Lewis, D. Y., Soloviev, D. & Brindle, K. M. Imaging Tumor Metabolism Using Positron Emission Tomography. *Cancer J. Sudbury Mass* **21,** 129–136 (2015).
8. Peters, G. J., Schornagel, J. H. & Milano, G. A. Clinical pharmacokinetics of anti-metabolites. *Cancer Surv.* **17,** 123–156 (1993).
9. Gascoigne, K. E. & Taylor, S. S. How do anti-mitotic drugs kill cancer cells? *J. Cell Sci.* **122,** 2579–2585 (2009).
10. Davis, M. E., Chen, Z. (Georgia) & Shin, D. M. Nanoparticle therapeutics: an emerging treatment modality for cancer. *Nat. Rev. Drug Discov.* **7,** 771–782 (2008).
11. Peer, D. *et al.* Nanocarriers as an emerging platform for cancer therapy. *Nat. Nanotechnol.* **2,** 751–760 (2007).
12. Farokhzad, O. C. & Langer, R. Impact of Nanotechnology on Drug Delivery. *ACS Nano* **3,** 16–20 (2009).

13. Lammers, T., Kiessling, F., Hennink, W. E. & Storm, G. Drug targeting to tumors: Principles, pitfalls and (pre-) clinical progress. *J. Controlled Release* **161,** 175–187 (2012).

14. Maeda, H., Wu, J., Sawa, T., Matsumura, Y. & Hori, K. Tumor vascular permeability and the EPR effect in macromolecular therapeutics: a review. *J. Control. Release Off. J. Control. Release Soc.* **65,** 271–284 (2000).

15. Heldin, C.-H., Rubin, K., Pietras, K. & Östman, A. High interstitial fluid pressure — an obstacle in cancer therapy. *Nat. Rev. Cancer* **4,** 806–813 (2004).

16. Jain, R. K. Normalization of Tumor Vasculature: An Emerging Concept in Antiangiogenic Therapy. *Science* **307,** 58–62 (2005).

17. McDonald, D. M. & Baluk, P. Significance of Blood Vessel Leakiness in Cancer. *Cancer Res.* **62,** 5381–5385 (2002).

18. Cao, Y. Tumor angiogenesis and molecular targets for therapy. *Front. Biosci. Landmark Ed.* **14,** 3962–3973 (2009).

19. Nagy, J. A., Chang, S.-H., Dvorak, A. M. & Dvorak, H. F. Why are tumour blood vessels abnormal and why is it important to know? *Br. J. Cancer* **100,** 865–869 (2009).

20. Harrington, K. J. *et al.* Effective Targeting of Solid Tumors in Patients With Locally Advanced Cancers by Radiolabeled Pegylated Liposomes. *Clin. Cancer Res.* **7,** 243–254 (2001).

21. Northfelt, D. W. *et al.* Pegylated-liposomal doxorubicin versus doxorubicin, bleomycin, and vincristine in the treatment of AIDS-related Kaposi's sarcoma: results of a randomized phase III clinical trial. *J. Clin. Oncol.* **16,** 2445–2451 (1998).

22. Kunjachan, S. *et al.* Passive versus active tumor targeting using RGD- and NGR-modified polymeric nanomedicines. *Nano Lett.* **14,** 972–981 (2014).

23. O'Brien, M. E. R. O'Brien ME, Wigler N, Inbar M, Rosso R, Grischke E, Santoro A, Catane R, Kieback DG, Tomczak P, Ackland SP, Orlandi F, Mellars L, Alland L, Tendler CReduced cardiotoxicity

and comparable efficacy in a phase III trial of pegylated liposomal doxorubicin HCl (CAELYXTM/Doxil®) vs conventional doxorubicin for first-line treatment of metastatic breast cancer. Ann Oncol 15: 440-449. *ResearchGate* **15,** 440–449 (2004).

24. Barua, S. & Mitragotri, S. Challenges associated with Penetration of Nanoparticles across Cell and Tissue Barriers: A Review of Current Status and Future Prospects. *Nano Today* **9,** 223–243 (2014).

25. Albanese, A., Tang, P. S. & Chan, W. C. W. The Effect of Nanoparticle Size, Shape, and Surface Chemistry on Biological Systems. *Annu. Rev. Biomed. Eng.* **14,** 1–16 (2012).

26. Parker, N. *et al.* Folate receptor expression in carcinomas and normal tissues determined by a quantitative radioligand binding assay. *Anal. Biochem.* **338,** 284–293 (2005).

27. Yoo, H. S. & Park, T. G. Folate-receptor-targeted delivery of doxorubicin nano-aggregates stabilized by doxorubicin–PEG–folate conjugate. *J. Controlled Release* **100,** 247–256 (2004).

28. Daniels, T. R. *et al.* Transferrin receptors and the targeted delivery of therapeutic agents against cancer. *Biochim. Biophys. Acta* **1820,** 291–317 (2012).

29. Garin-Chesa, P. *et al.* Trophoblast and ovarian cancer antigen LK26. Sensitivity and specificity in immunopathology and molecular identification as a folate-binding protein. *Am. J. Pathol.* **142,** 557–567 (1993).

30. Zwicke, G. L., Mansoori, G. A. & Jeffery, C. J. Utilizing the folate receptor for active targeting of cancer nanotherapeutics. *Nano Rev.* **3,** (2012).

31. Habeshaw, J. A., Lister, T. A., Stansfeld, A. G. & Greaves, M. F. Correlation of transferrin receptor expression with histological class and outcome in non-Hodgkin lymphoma. *Lancet Lond. Engl.* **1,** 498–501 (1983).

32. Das Gupta, A. & Shah, V. I. Correlation of transferrin receptor expression with histologic grade and immunophenotype in chronic lymphocytic leukemia and non-Hodgkin's lymphoma. *Hematol. Pathol.* **4,** 37–41 (1990).

33. Yang, D. C., Wang, F., Elliott, R. L. & Head, J. F. Expression of transferrin receptor and ferritin H-chain mRNA are associated with clinical and histopathological prognostic indicators in breast cancer. *Anticancer Res.* **21,** 541–549 (2001).

34. Seymour, G. J., Walsh, M. D., Lavin, M. F., Strutton, G. & Gardiner, R. A. Transferrin receptor expression by human bladder transitional cell carcinomas. *Urol. Res.* **15,** 341–344 (1987).

35. Kondo, K. *et al.* Transferrin Receptor Expression in Adenocarcinoma of the Lung as a Histopathologic Indicator of Prognosis. *Chest* **97,** 1367–1371 (1990).

36. Prior, R., Reifenberger, G. & Wechsler, W. Transferrin receptor expression in tumours of the human nervous system: relation to tumour type, grading and tumour growth fraction. *Virchows Arch. A Pathol. Anat. Histopathol.* **416,** 491–496 (1990).

37. Rathinam, R. & Alahari, S. K. Important role of integrins in the cancer biology. *Cancer Metastasis Rev.* **29,** 223–237 (2010).

38. Cox, D., Brennan, M. & Moran, N. Integrins as therapeutic targets: lessons and opportunities. *Nat. Rev. Drug Discov.* **9,** 804–820 (2010).

39. Danen, E. H. J. Integrin Signaling as a Cancer Drug Target. *Int. Sch. Res. Not.* **2013,** e135164 (2013).

40. Desgrosellier, J. S. & Cheresh, D. A. Integrins in cancer: biological implications and therapeutic opportunities. *Nat. Rev. Cancer* **10,** 9–22 (2010).

41. Weis, S. M. & Cheresh, D. A. αv Integrins in Angiogenesis and Cancer. *Cold Spring Harb. Perspect. Med.* **1,** (2011).

42. Sitohy, B., Nagy, J. A. & Dvorak, H. F. Anti-VEGF/VEGFR therapy for cancer: Reassessing the target. *Cancer Res.* **72,** 1909–1914 (2012).

43. Niu, G. & Chen, X. Vascular Endothelial Growth Factor as an Anti-angiogenic Target for Cancer Therapy. *Curr. Drug Targets* **11,** 1000–1017 (2010).

44. Jang, M., Kim, S. S. & Lee, J. Cancer cell metabolism: implications for therapeutic targets. *Exp. Mol. Med.* **45,** e45 (2013).

45. Adekola, K., Rosen, S. T. & Shanmugam, M. Glucose transporters in cancer metabolism. *Curr. Opin. Oncol.* **24,** 650–654 (2012).

46. Hanahan, D. & Weinberg, R. A. Hallmarks of Cancer: The Next Generation. *Cell* **144,** 646–674 (2011).

47. Bensinger, S. J. & Christofk, H. R. New aspects of the Warburg effect in cancer cell biology. *Semin. Cell Dev. Biol.* **23,** 352–361 (2012).

48. Bensinger, S. J. & Christofk, H. R. New aspects of the Warburg effect in cancer cell biology. *Semin. Cell Dev. Biol.* **23,** 352–361 (2012).

49. Miles, K. A. PET-CT in oncology: making the most of CT. *Cancer Imaging* **8,** S87–S93 (2008).

50. Butler, E. B., Zhao, Y., Pinedo, C. M., Lu, J. & Tan, M. Stalling the engine of resistance: targeting cancer metabolism to overcome therapeutic resistance. *Cancer Res.* **73,** 2709–2717 (2013).

51. Zhao, Y., Butler, E. B. & Tan, M. Targeting cellular metabolism to improve cancer therapeutics. *Cell Death Dis.* **4,** e532 (2013).

52. Hollak, C. E. M. & Lachmann, R. *Inherited Metabolic Disease in Adults: A Clinical Guide*. (Oxford University Press, 2016).

53. Yonezawa, A., Masuda, S., Katsura, T. & Inui, K. Identification and functional characterization of a novel human and rat riboflavin transporter, RFT1. *Am. J. Physiol. - Cell Physiol.* **295,** C632–C641 (2008).

54. Yamamoto, S. *et al.* Identification and Functional Characterization of Rat Riboflavin Transporter 2. *J. Biochem. (Tokyo)* **145,** 437–443 (2009).

55. Yao, Y. *et al.* Identification and Comparative Functional Characterization of a New Human Riboflavin Transporter hRFT3 Expressed in the Brain. *J. Nutr.* **140,** 1220–1226 (2010).

56. Subramanian, V. S., Ghosal, A., Subramanya, S. B., Lytle, C. & Said, H. M. Differentiation-dependent regulation of intestinal vitamin B2 uptake: studies utilizing human-derived intestinal epithelial Caco-2 cells and native rat intestine. *Am. J. Physiol. - Gastrointest. Liver Physiol.* **304,** G741–G748 (2013).

57. H B White, III & A H Merrill, J. Riboflavin-Binding Proteins. *Annu. Rev. Nutr.* **8,** 279–299 (1988).

58. Monaco, H. L. Crystal structure of chicken riboflavin-binding protein. *EMBO J.* **16,** 1475–1483 (1997).

59. Miura, R., Tojo, H., Fujii, S. & Miyake, Y. A 13C-NMR Study on the Interaction of Riboflavin with Egg White Riboflavin Binding Protein. *J. Biochem. (Tokyo)* **96,** 197–206 (1984).

60. Merrill, A. H., Froehlich, J. A. & McCormick, D. B. Purification of riboflavin-binding proteins from bovine plasma and discovery of a pregnancy-specific riboflavin-binding protein. *J. Biol. Chem.* **254,** 9362–9364 (1979).

61. Mason, C. W. *et al.* Recognition, Cointernalization, and Recycling of an Avian Riboflavin Carrier Protein in Human Placental Trophoblasts. *J. Pharmacol. Exp. Ther.* **317,** 465–472 (2006).

62. Karande, A. A., Sridhar, L., Gopinath, K. s. & Adiga, P. R. Riboflavin carrier protein: A serum and tissue marker for breast carcinoma. *Int. J. Cancer* **95,** 277–281 (2001).

63. Rao, P. N. *et al.* Elevation of Serum Riboflavin Carrier Protein in Breast Cancer. *Cancer Epidemiol. Biomarkers Prev.* **8,** 985–990 (1999).

64. Rao, P. N. *et al.* Elevation of serum riboflavin carrier protein in hepatocellular carcinoma. *Hepatol. Res. Off. J. Jpn. Soc. Hepatol.* **35,** 83–87 (2006).

65. Johnson, T. *et al.* Biochemical characterization of riboflavin carrier protein (RCP) in prostate cancer. *Front. Biosci. Landmark Ed.* **14,** 3634–3640 (2009).

66. Aili, A. *et al.* Association of the Plasma and Tissue Riboflavin Levels with C20orf54 Expression in Cervical Lesions and Its Relationship to HPV16 Infection. *PLoS ONE* **8,** (2013).

67. Bareford, L. M., Avaritt, B. R., Ghandehari, H., Nan, A. & Swaan, P. W. Riboflavin-Targeted Polymer Conjugates for Breast Tumor Delivery. *Pharm. Res.* **30,** 1799–1812 (2013).

68. Beztsinna, N. *et al.* Amphiphilic Phospholipid-Based Riboflavin Derivatives for Tumor Targeting Nanomedicines. *Bioconjug. Chem.* **27,** 2048–2061 (2016).

69. Beztsinna, N. *et al.* Photoacoustic imaging of tumor targeting with riboflavin-functionalized theranostic nanocarriers. *Int. J. Nanomedicine* **in press,**

70. Jayapaul, J. *et al.* FMN-coated fluorescent iron oxide nanoparticles for RCP-mediated targeting and labeling of metabolically active cancer and endothelial cells. *Biomaterials* **32,** 5863–5871 (2011).

71. Jayapaul, J. *et al.* Riboflavin carrier protein-targeted fluorescent USPIO for the assessment of vascular metabolism in tumors. *Biomaterials* **33,** 8822–8829 (2012).

72. Jayapaul, J. *et al.* In vivo evaluation of riboflavin receptor targeted fluorescent USPIO in mice with prostate cancer xenografts. *Nano Res.* **9,** 1319–1333 (2016).

73. Mertens, M. E. *et al.* FMN-Coated Fluorescent USPIO for Cell Labeling and Non-Invasive MR Imaging in Tissue Engineering. *Theranostics* **4,** 1002–1013 (2014).

74. Tsvetkova, Y. *et al.* Refinement of adsorptive coatings for fluorescent riboflavin-receptor-targeted iron oxide nanoparticles. *Contrast Media Mol. Imaging* (2015). doi:10.1002/cmmi.1657

75. Ali, A. *et al.* Synthesis, characterization, applications, and challenges of iron oxide nanoparticles. *Nanotechnol. Sci. Appl.* **9,** 49–67 (2016).

76. Laurent, S. *et al.* Magnetic Iron Oxide Nanoparticles: Synthesis, Stabilization, Vectorization, Physicochemical Characterizations, and Biological Applications. *Chem. Rev.* **108,** 2064–2110 (2008).

77. Lefebure, S., Dubois, E., Cabuil, V., Neveu, S. & Massart, R. Monodisperse magnetic nanoparticles: Preparation and dispersion in water and oils. *J. Mater. Res.* **13,** 2975–2981 (1998).

78. Bacri, J.-C., Perzynski, R., Salin, D., Cabuil, V. & Massart, R. Ionic ferrofluids: A crossing of chemistry and physics. *J. Magn. Magn. Mater.* **85,** 27–32 (1990).

79. Hodenius, M. *et al.* Fluorescent magnetoliposomes as a platform technology for functional and molecular MR and optical imaging. *Contrast Media Mol. Imaging* **7,** 59–67 (2012).

80. Hori, T. & Sugiyama, M. Use of hydrous iron(III) oxide in a concentration step for the determination of trace amounts of organophosphorus compounds in aqueous solutions. *Analyst* **117,** 893–897 (1992).

81. Lewinski, N., Colvin, V. & Drezek, R. Cytotoxicity of nanoparticles. *Small Weinh. Bergstr. Ger.* **4,** 26–49 (2008).

82. Bulte, J. W. M. & Kraitchman, D. L. Iron oxide MR contrast agents for molecular and cellular imaging. *NMR Biomed.* **17,** 484–499 (2004).

83. Vaskovsky, V. E., Kostetsky, E. Y. & Vasendin, I. M. A universal reagent for phospholipid analysis. *J. Chromatogr.* **114,** 129–141 (1975).

84. Tsvetkova, Y. *et al.* Balancing Passive and Active Targeting to Different Tumor Compartments Using Riboflavin-Functionalized Polymeric Nanocarriers. *Nano Lett.* **17,** 4665–4674 (2017).

85. Maeda, H. & Matsumura, Y. EPR effect based drug design and clinical outlook for enhanced cancer chemotherapy. *Adv. Drug Deliv. Rev.* **63,** 129–130 (2011).

86. Kunjachan, S. *et al.* Nanoparticle Mediated Tumor Vascular Disruption: A Novel Strategy in Radiation Therapy. *Nano Lett.* **15,** 7488–7496 (2015).

87. Jain, R. K. Transport of molecules in the tumor interstitium: a review. *Cancer Res.* **47,** 3039–3051 (1987).

88. Barua, S. & Mitragotri, S. Challenges associated with Penetration of Nanoparticles across Cell and Tissue Barriers: A Review of Current Status and Future Prospects. *Nano Today* **9,** 223–243 (2014).

89. Yamaoka, T., Tabata, Y. & Ikada, Y. Distribution and Tissue Uptake of Poly(ethylene glycol) with Different Molecular Weights after Intravenous Administration to Mice. *J. Pharm. Sci.* **83,** 601–606 (1994).

90. Radomsky, M. L., Whaley, K. J., Cone, R. A. & Saltzman, W. M. Macromolecules released from polymers: diffusion into unstirred fluids. *Biomaterials* **11,** 619–624 (1990).

91. Armstrong, J. K., Wenby, R. B., Meiselman, H. J. & Fisher, T. C. The Hydrodynamic Radii of Macromolecules and Their Effect on Red Blood Cell Aggregation. *Biophys. J.* **87,** 4259–4270 (2004).

92. Charles A Janeway, J., Travers, P., Walport, M. & Shlomchik, M. J. *The distribution and functions of immunoglobulin isotypes*. (2001).

93. Miranda-Lorenzo, I. *et al.* Intracellular autofluorescence: a biomarker for epithelial cancer stem cells. *Nat. Methods* **11,** 1161–1169 (2014).

94. Kunjachan, S. *et al.* Non-Invasive Optical Imaging of Nanomedicine Biodistribution. *ACS Nano* **7,** 252–262 (2013).

95. Chauhan, V. P., Stylianopoulos, T., Boucher, Y. & Jain, R. K. Delivery of Molecular and Nanoscale Medicine to Tumors: Transport Barriers and Strategies. *Annu. Rev. Chem. Biomol. Eng.* **2,** 281–298 (2011).

96. Lim, E.-K., Jang, E., Lee, K., Haam, S. & Huh, Y.-M. Delivery of Cancer Therapeutics Using Nanotechnology. *Pharmaceutics* **5,** 294–317 (2013).

97. Meng, F., Cheng, R., Deng, C. & Zhong, Z. Intracellular drug release nanosystems. *Mater. Today* **15,** 436–442 (2012).

98. Chanmee, T., Ontong, P., Konno, K. & Itano, N. Tumor-Associated Macrophages as Major Players in the Tumor Microenvironment. *Cancers* **6,** 1670–1690 (2014).

99. Miller, M. A. *et al.* Tumour-associated macrophages act as a slow-release reservoir of nano-therapeutic Pt(IV) pro-drug. *Nat. Commun.* **6,** 8692 (2015).

100. Caelen, I., Kalman, A. & Wahlström, L. Biosensor-Based Determination of Riboflavin in Milk Samples. *Anal. Chem.* **76,** 137–143 (2004).